



National Library
of Canada

Acquisitions and
Bibliographic Services Branch

385 Wellington Street
Ottawa, Ontario
K1A 0N4

Bibliothèque nationale
du Canada

Direction des acquisitions et
des services bibliographiques

385, rue Wellington
Ottawa (Ontario)
K1A 0N4

Produit par la Bibliothèque nationale du Canada

Produit par la Bibliothèque nationale du Canada

NOTICE

The quality of this microform is heavily dependent upon the quality of the original thesis submitted for microfilming. Every effort has been made to ensure the highest quality of reproduction possible.

If pages are missing, contact the university which granted the degree.

Some pages may have indistinct print especially if the original pages were typed with a poor typewriter ribbon or if the university sent us an inferior photocopy.

Reproduction in full or in part of this microform is governed by the Canadian Copyright Act, R.S.C. 1970, c. C-30, and subsequent amendments.

AVIS

La qualité de cette microforme dépend grandement de la qualité de la thèse soumise au microfilmage. Nous avons tout fait pour assurer une qualité supérieure de reproduction.

S'il manque des pages, veuillez communiquer avec l'université qui a conféré le grade.

La qualité d'impression de certaines pages peut laisser à désirer, surtout si les pages originales ont été dactylographiées à l'aide d'un ruban usé ou si l'université nous a fait parvenir une photocopie de qualité inférieure.

La reproduction, même partielle, de cette microforme est soumise à la Loi canadienne sur le droit d'auteur, SRC 1970, c. C-30, et ses amendements subséquents.

Canada

UNIVERSITY OF ALBERTA

**APPLICATION OF THE SYNTHETIC DUAL-DOPPLER TECHNIQUE TO AN
OPERATIONAL DOPPLER WEATHER RADAR**

by



Bruno Larochelle

**A thesis submitted to the Faculty of Graduate Studies and Research in partial fulfillment of
the requirements for the degree of MASTER OF SCIENCE**

in

METEOROLOGY

DEPARTMENT OF GEOGRAPHY

**Edmonton, Alberta
Spring 1994**



National Library
of Canada

Acquisitions and
Bibliographic Services Branch

395 Wellington Street
Ottawa, Ontario
K1A 0N4

Bibliothèque nationale
du Canada

Direction des acquisitions et
des services bibliographiques

395, rue Wellington
Ottawa (Ontario)
K1A 0N4

Author's name - Nom de l'auteur

Author's title - Titre de l'ouvrage

The author has granted an irrevocable non-exclusive licence allowing the National Library of Canada to reproduce, loan, distribute or sell copies of his/her thesis by any means and in any form or format, making this thesis available to interested persons.

L'auteur a accordé une licence irrévocable et non exclusive permettant à la Bibliothèque nationale du Canada de reproduire, prêter, distribuer ou vendre des copies de sa thèse de quelque manière et sous quelque forme que ce soit pour mettre des exemplaires de cette thèse à la disposition des personnes intéressées.

The author retains ownership of the copyright in his/her thesis. Neither the thesis nor substantial extracts from it may be printed or otherwise reproduced without his/her permission.

L'auteur conserve la propriété du droit d'auteur qui protège sa thèse. Ni la thèse ni des extraits substantiels de celle-ci ne doivent être imprimés ou autrement reproduits sans son autorisation.

ISBN 0-612-11270-5

Canada

UNIVERSITY OF ALBERTA

RELEASE FORM

NAME OF AUTHOR Bruno Larochelle

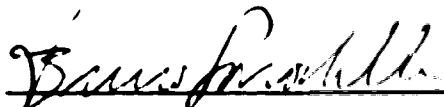
TITLE OF THESIS Application of the synthetic dual-Doppler technique to an operational Doppler weather radar

DEGREE Master of Science in Meteorology

YEAR DEGREE GRANTED 1994

Permission is hereby granted to the University of Alberta Library to reproduce single copies of this thesis and to lend or sell such copies for private, scholarly or scientific purposes only.

The author reserves all other publication and other rights in association with the copyright in the thesis, and except as herein before provided neither the thesis nor any substantial portion thereof may be printed or otherwise reproduced in any material form whatever without the author's prior written permission.



Bruno Larochelle

9288-54 St.

Edmonton, Alberta

T6B 2L4

April 6 1994

UNIVERSITY OF ALBERTA

FACULTY OF GRADUATE STUDIES AND RESEARCH

The undersigned certify that they have read, and recommend to the Faculty of Graduate Studies and Research for acceptance, a thesis entitled APPLICATION OF THE SYNTHETIC DUAL-DOPPLER TECHNIQUE TO AN OPERATIONAL DOPPLER WEATHER RADAR submitted by Bruno Larochelle in partial fulfillment of the requirements for the degree of MASTER OF SCIENCE in METEOROLOGY



G.W. Reuter, Supervisor



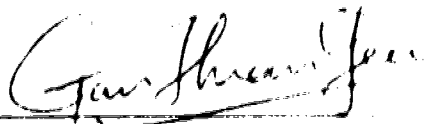
E.P. Lozowski



J.D. Wilson



R. Eyton



T. Gan

April 6, 1994

Pour Raymond et Gertrude, Louise et Alodie, je vous aime beaucoup

For my mother and father, wife and daughter

Abstract

The Synthetic Dual-Doppler (SDD) technique combines radial wind measurements recorded at two different times by a single Doppler radar to obtain the horizontal wind flow in a precipitating storm. This thesis examines the usefulness and accuracy of the SDD technique when applied to operational Doppler radars which scan only a few low-level elevation angles.

Numerical experiments of the SDD technique applied to a moving Rankine vortex with random errors superimposed on the flow provided the following results:

1. The errors in the synthesized wind increase linearly with the uncertainty of the Doppler velocities and are inversely proportional to the sine of the difference in storm viewing angles.
2. The most significant errors in the wind field reconstruction tend to be in the wind component perpendicular to the average storm viewing angle.
3. The SDD technique has a tendency to overestimate the actual wind speed.
4. The errors in the synthesized wind can become large when changes occur in the storm-relative flow.

Formal relationships were derived for the first three findings and gave excellent agreement with the experimental results.

Computer software was developed to apply the SDD technique on mesoscale precipitating systems monitored by operational Doppler radars located at Carvel, Alberta, and King City, Ontario. The SDD technique was found to be useful in identifying a roll circulation associated with an August 6 1993 gust front sweeping across central Alberta. For a July 30 1993 storm over east-central Alberta, the SDD synthesized wind field indicated a vortex in the low level flow 90 minutes prior to the visual observations of an F3 tornado. This case shows that proper use of the SDD technique can be useful for tornado forecasting.

Acknowledgments

I am indebted to the many individuals who provided encouragement and guidance to me during this undertaking. In particular, I wish to thank:

- ◆ **Dr. G.W. Reuter, my thesis supervisor. His comments, suggestions and guidance were invaluable and very much appreciated.**
- ◆ **Mr. Tom Nichols, for the many hours spent to familiarize me with the weather radar archive and for the numerous comments and suggestions.**

- ◆ **The professors of the Division of Meteorology, for their excellent teaching.**
- ◆ **Mr. D.B. Burnett and Mr. B. Paruk, of the Alberta Weather Center, for kindly providing office space and facilities during my leave of absence.**
- ◆ **Mr. H. Ewen, electronics technician, for my initial tour of the Carvel radar and comments pertaining to the facility.**
- ◆ **Dr. A.H. Kalantar, for discussions on data uncertainties.**
- ◆ **Mr. T. Thompson and Mrs. L. Smith, for their unhesitant and varied support.**
- ◆ **Dr. P.I. Joe, for his comments on the radar archive and for providing the July 24 1987 King City radar data.**
- ◆ **Dr. N.R. Donaldson, for his helpful comments in the initial stages of this undertaking.**

- ◆ **The Atmospheric Environment Service of Environment Canada, for the financial support provided during my educational leave.**

- ◆ **My wife Louise and daughter Alodie.**

Table of contents

1. Introduction	1
1.1. Historical perspective of Doppler weather radars	1
1.2. Basics of the SDD technique	3
1.3. Overview of SDD research (1968-1994)	6
1.4. Research and "operational" Doppler weather radars	9
1.5. Objectives of this thesis and approach to the research	11
1.6. Outline of subsequent chapters	12
2. Limitations and inaccuracies in the SDD technique	14
2.1. Error analysis of the basic wind synthesis equations	14
2.2. The quasi-steady and azimuthal motion requirements	14
2.3. The influence of storm viewing geometry on the synthesized wind field	16
2.4. Error sources in the SDD technique	17
2.5. Restrictions on the SDD technique caused by limited scan Doppler radars	19
3. Development of computer programs	21
3.1. A synthetic dual-Doppler simulator	21
3.2. A synthetic dual-Doppler analyzer	22
3.3. Interactive adjustment of storm positions using "sliding windows"	25
4. Sensitivity tests on the synthetic dual-Doppler technique	29
4.1. Errors caused by spectral broadening mechanisms	29
4.2. Errors caused by imprecise storm position matching	30
4.3. Errors caused by height changes	31
4.4. Errors caused by an evolving wind field	31
4.5. Errors caused by combined effects	32
4.6. Dependence of SDD analyses on angular separation	34
4.7. Observations of the dependence of SDD analyses to wind orientation	35
4.8. Observations of a speed bias due to errors in radial velocities	36
4.9. Concluding remarks	39
5. SDD analyses of mesoscale phenomena over Alberta	65
5.1. The gust front of August 06 1993	65
5.2. The severe storms of July 29-30 1993	67
5.3. The Holden tornadic storm (July 30, 1993)	68

6. SDD analysis of the "Mississauga storm"	103
6.1 Synthesized horizontal wind field at low levels	103
6.2 Test of the quasi-steady assumption	104
6.3 Horizontal wind fields at higher levels	105
6.4 Concluding remarks	105
7. Conclusions and suggestions for future work	116
7.1 Summary of the main results	117
7.2 Suggestions for future work	120
Bibliography	123
Appendices	127
A. Radar characteristics	127
B. Data preprocessing	128
C. Notes on the programs	130
D. Derivations of (4.2),(4.5) and (4.6)	133
E. Calculations for an evolving mesocyclone	138

List of Tables

<i>Table</i>	<i>Content</i>	<i>Page</i>
4.1	Simulation results for an SDD case with combined errors	34
4.2	Simulation results of bias reduction on a Burgess mesocyclone	39

List of Figures

<i>Figures</i>	<i>Content</i>	<i>Pages</i>
1 1	Single Doppler observations	4
1 2	SDD wind synthesis	4
1 3	SDD layout	5
1 4	Changes in viewing angle caused by parallax	6
1 5	Full volume scan of the AES Doppler radars	10
1 6	Limited scan of the AES Doppler radars	11
2 1	Relationship between angular velocity and range	15
2 2	Optimum orientation of the true wind for SDD synthesis	16
3 1	Outline of the SDD simulator program	26
3 2	Outline of the SDD analyzer	27
3 3	"Sliding windows" concept	28
3 4	Use of "sliding windows"	28
4 1	Effect of spectral noise on SDD synthesis	40-42
4 2	Effect of incorrect horizontal position matching on SDD synthesis	43-45
4 3	Sensitivity of SDD mesocyclone analysis to position matching	46
4.4	Effect of temporal changes on SDD synthesis	47-49
4.5	Effect of combined errors on SDD synthesis	50-53
4.6	SDD dependence on angular separation	54-55
4.7	RMS errors for SDD analysis as a function of angular separation	56
4.8	The effect of wind orientation on SDD synthesis	57-59
4.9	The effect of wind orientation on SDD synthesis for a mesocyclone	60
4.10	Velocity difference fields as a function of angular separation	61-63
4.11	Average speed bias ratio for SDD synthesis	64

(continued on next page)

List of Figures (continued)

<i>Figures</i>	<i>Content</i>	<i>Page</i>
5.1	The August 06 1993 case: reflectivity and velocity images	72
5.2-5.9	SDD analysis of the August 06 1993 case: 2050Z-2150Z	73-76
5.10	SDD analysis of the August 06 1993 case at higher levels	77-79
5.11	Schematic diagram showing a roll circulation within a gust front	80
5.12	SDD analysis of the August 06 1993 case: 2050Z-2120Z	81
5.13	SDD analysis of the August 06 1993 case: 2120Z-2150Z	82
5.14	The July 29-30 1993 case: reflectivity and velocity images	83-84
5.15	SDD analysis of the July 29-30 case: 2310Z-2340Z	85-87
5.16	SDD analysis of the July 29-30 case: 0030Z-0100Z	88-90
5.17	1.5° SDD analysis of the July 29-30 case	91
5.18	The July 30 1993 mesocyclone (Holden): reflectivity and velocity images	92
5.19-5.26	SDD analysis of the Holden case: 0150Z-0250Z	93-96
5.27	SDD analyses for the Holden case at 0150Z-0220Z and 0220Z-0250Z	97-98
5.28	Ground truthing for the July 30 1993 Holden tornado	99
5.29	Display of the bounded weak echo region (BWER) for the Holden case	100
5.30	Conceptual model of the BWER for the Holden case	101
5.31	Conceptual model of the Holden tornadic storm	102
6.1	The July 24 1987 storm (Mississauga): reflectivity and velocity	106-107
6.2	SDD analysis of the Mississauga case: 2200Z-2220Z	108-109
6.3	Vorticity and convergence fields for the Mississauga case	110
6.4	SDD analyses of the Mississauga case: comparisons of the 2200Z-2220Z analysis with analyses at 2210Z-2230Z and 2210Z-2240Z	111-113
6.5	1.5° and 3.5° analyses for the Mississauga case	114-115

List of Symbols

β_1	azimuth of first Doppler measurement
β_2	azimuth of second Doppler measurement
β	average viewing azimuth of the first and second Doppler measurements
$\Delta\beta$	difference between the first and second azimuths of the Doppler data sets
c	translation speed of precipitating storm or feature
$d\beta$	error in azimuth measurements
dr	error in Doppler measurements
du	error in the u component of the synthesized wind field
dv	error in the v component of the synthesized wind field
dx	"base line" between the two synthetic Doppler radars
λ	operating wavelength of the radar
M	number of Doppler measurements made for a given volume sample
PRF	pulse repetition frequency(ies) of the radar
R	distance between storm and radar
r_u	maximum unambiguous Doppler velocity (Nyquist velocity)
r_1	first measurement of Doppler velocity
r_2	second measurement of Doppler velocity
RMS_{err}	RMS difference between the initial and reconstructed wind fields
SBR	speed bias ratio (ratio of reconstructed and initial wind fields)
SNR	signal to noise ratio
σ_v	standard deviation of the Doppler velocity spectrum, or spectral width
σ_r	standard deviation of the mean Doppler velocity estimate
t_1	time of the first Doppler measurement
t_2	time of the second Doppler measurement
u	u component of synthesized wind field
v	v component of synthesized wind field
u_0	u component of original (initial) wind field
v_0	v component of original (initial) wind field
v_t	tangential velocity of a precipitating storm
ω	angular velocity of a precipitating storm as seen by the radar
$\langle \rangle$	used to represent the average over a Gaussian distribution of noise
$\bar{}$	used to represent the spatial average over a wind field

List of Abbreviations

AES	Atmospheric Environment Service (Environment Canada)
AGL	Above Ground Level
ALWC	ALberta Weather Center (Edmonton)
BVP	Banded Velocity Processing
BWER	Bounded Weak Echo Region
FFT	Fast Fourier Transform
MCS	Mesoscale Convective System
NEXRAD	NEXt generation of weather RADars (United States)
NCAR	National Center for Atmospheric Research (Boulder, Colorado)
PC	Personal Computer
RMS	Root-Mean-Square
SDD	Synthetic Dual-Doppler
VAD	Velocity Azimuth Display
VVP	Volume Velocity Processing
WHK	Call letters for the Carvel radar site, near Carvel, Alberta
WKR	Call letters for the King City radar site, near King City, Ontario

Glossary

Reflectivity factor (Z)- The reflectivity factor quantifies the combined effect of a collection of precipitation particles on scattering electromagnetic energy back to the radar. It is defined as the sum of the diameter of the particles to the sixth power per unit volume (i.e. $Z = \sum D^6$ with units of mm^6m^{-3}). This quantity is usually expressed in dBZ (i.e. $10\log(Z/(1 \text{ mm}^6\text{m}^{-3}))$). The reflectivity factor is used for describing the intensity of radar echoes and is commonly referred to simply as the "reflectivity".

Beam width - The angle within which the microwave radiation from the radar beam is at least one-half its peak intensity (i.e. 3 dB width)

Velocity spectrum - The FFT signal processor of the radar system uses the measured phase shifts between many pulse pairs (typically 65) to build a velocity spectrum. This spectrum can usually be approximated as a normal distribution. The mean of the distribution is archived as the *mean radial velocity* and the standard deviation of the distribution is archived as the *spectral width*.

PPI - Plan Position Indicator radar chart. A two-dimensional remapping of the conical area swept out by a radar scanning at a constant elevation angle.

Volume scan - This is the set of PPI radar scans and it can be used to build a three dimensional representation of the radar reflectivity. For the AES radars in Doppler mode, the volume scan is limited, consisting of only three or four low elevation angle Doppler velocity scans.

LOG Z - Reflectivity factor radar chart. A PPI type chart showing the radar reflectivity (in dBZ). When the radar is in Doppler mode, ground clutter (signal returns from fixed targets, like mountains...) can be removed to get the CORRECTED LOG Z chart.

CAPPI - Constant Altitude Plan Position Indicator radar chart. Sections of many different elevation angle reflectivity PPI's (i.e. the volume scan) are used to build a 2-D mapping representing radar reflectivity at a semi-constant height above ground.

MAX R - Maximum Rainfall Rate radar chart. This is a 2-D mapping of the maximum rainfall rate (related to reflectivity) above 2 km in the volume scan.

ECHO TOPS - Echo Tops radar chart. This is a 2-D mapping of the maximum height at which the radar reflectivity is at least 10 dBZ.

SEVERE - Severe weather radar chart. This is a 2-D mapping of parameters which are considered to indicate a strong potential for severe weather. Currently, the display includes the maximum height at which reflectivities of 40 dBZ or more were recorded, superimposed with the locations and frequency of lightning strikes.

"Run-time" - Expression used to refer to real-time interaction with a computer program. For example, parameters can be adjusted without re-running the program. Feedback on any adjustments is immediate.

1. Introduction

1.1. Historical perspective on Doppler weather radars

The late 1930's saw rapid development in microwave radar technology (Fletcher 1990). With war about to break out, the driving force behind radar research was the ability to detect and monitor enemy aircraft well before they could be seen or heard. Researchers soon saw that microwave radar was also able to detect rain and snow because precipitating particles acted as scatterers to electromagnetic waves. The first recorded measurements of precipitation echoes by radar were made in February 1941. During the war years, weather radar research focused on the atmosphere's influence on microwave propagation, with little interest in the actual measurement of precipitation. However, shortly after World War II, research groups in the United States and Canada started to concentrate their efforts on precipitation and storms (Atlas 1990).

Until the early 1950's, weather radars were used mainly to measure the location and intensity (reflectivity) of precipitating echoes. At that time, however, the United States military was beginning to retrieve velocity information on radar targets through the use of coherent radio signals and the Doppler effect. Barrat and Browne (1953) used these same principles to make velocity measurements on a rain shower. The Doppler weather radar field became well established when Brantley and Barczys (1957) reported velocity measurements of various weather phenomena using a continuous wave Doppler radar unit (Rogers 1990).

The Doppler radar greatly increased the possibility of studying air flow motions in weather systems. Velocity information retrieved from a single Doppler radar is however ambiguous since only the radial component of the velocity vector (i.e. towards or away from the radar) can be inferred through the Doppler effect. Spatial assumptions can be made of the wind flow to remove this ambiguity, and these have led to retrieval techniques for the wind speed and direction averaged over a conical surface. The basis of these is the Velocity Azimuth Display (VAD) technique, which assumes that the wind field is locally linear. It was first proposed by Lhermitte and Atlas (1961), with further developments by Caton (1963), Browning and Wexler (1968) and Easterbrook (1975). Since that time, numerous extensions to the technique have been developed. Unfortunately, the area over which the wind speed and direction are averaged in these techniques is usually relatively large and therefore unsuitable for a wind flow study of weather phenomena on the convective or meso scales (e.g. thunderstorms, squall lines, gust fronts). In addition, the

linearity assumption upon which the techniques are based is usually inappropriate for mesoscale weather systems.

The desire to understand mesoscale weather phenomena prompted the use of dual or multiple Doppler radar. Using two Doppler radars, a precipitating system can be observed simultaneously from two viewing angles. By using low radar elevation angles, the radial components are uncontaminated by vertical velocity components (up and down drafts) and a synthesis of horizontal winds in the system is possible. Three or more Doppler radars are needed for the reconstruction of a three dimensional wind field (i.e. including horizontal and vertical motions). Estimates of the fall speed of hydrometeors (which scatter microwave energy) are also needed if the intent is to deduce the actual vertical air flow. If the continuity equation is invoked, it is also possible to solve the 3-D problem using only two radars.

There are two major drawbacks to dual or multiple Doppler arrangements. First and foremost, they are very costly. Second, unless the positions of the radars can be moved to suit a particular storm system, accurate wind field synthesis can only be done in certain locations relative to the radars. This limitation is caused by resolution problems and the requirement for a substantially different viewing angle (to the storm) between the radars. Airborne Doppler radar provides a solution to the geometrical constraints by moving the radar and observing the same precipitating complex from two significantly different viewing angles. This is often referred to as "pseudo-multiple Doppler" since only one radar is actually used. Being aboard a high speed aircraft, the radar can make measurements from different viewing angles within minutes (i.e. semi-synchronous). Unfortunately, the prohibitive cost of airborne Doppler radars limits their use to a few field experiments per year (Jorgensen 1986).

Peace et al (1968) proposed the basis for a technique which had the potential for studying mesoscale weather phenomena using a single Doppler radar. This method consists of a comparison between two sequential Doppler radar observations of a moving precipitating complex. These two observations can be used to emulate simultaneous observations from two Doppler radars at different locations. The two radial wind fields thus obtained allow for the reconstruction of the horizontal wind field in a precipitating complex. In order to obtain useful results from the technique, the wind structure of the weather system must remain quasi-steady between observations. In addition, the complex should be advecting at a significant speed so as to obtain a significantly different viewing angle between the single Doppler observations. Being based on only one radar unit, the method, commonly referred to as *synthetic dual-Doppler* (SDD), is less expensive than it's double radar counterpart. Furthermore, the restrictive geometry of dual-Doppler is relaxed

somewhat as only one radar is involved in defining acceptable orientations relative to a weather complex

1.2. Basics of the SDD technique

1.2.1 Geometry of the SDD technique

The synthetic dual-Doppler technique is based on the notion that wind measurements sampled by a single Doppler radar at two different times can be interpreted as simultaneous measurements by two Doppler radars at different sites. Three basic assumptions are required for such a time-to-space conversion:

1. Radial wind measurements must be available at two times t_1 and t_2 , where $t_2 - t_1$ is typically 20 to 60 minutes.
2. During the time period t_1 to t_2 , the storm relative flow pattern must remain quasi-steady (i.e. no significant changes in the internal storm circulation).
3. The motion of the precipitating system must be such that the viewing angle from the radar changes significantly from t_1 to t_2 (i.e. the motion must be largely azimuthal).

The following example illustrates the way in which the data from two different times are synthesized (time-to-space). At a time t_1 , the radial wind component is shown together with a series of possible wind vectors that are consistent with the actual observed radial component (Figure 1.1). At a time t_2 , a similar situation emerges. During the time interval $t_2 - t_1$ the precipitating system moved eastward by a distance $\Delta x = c(t_2 - t_1)$, where c is the translation speed of the system.

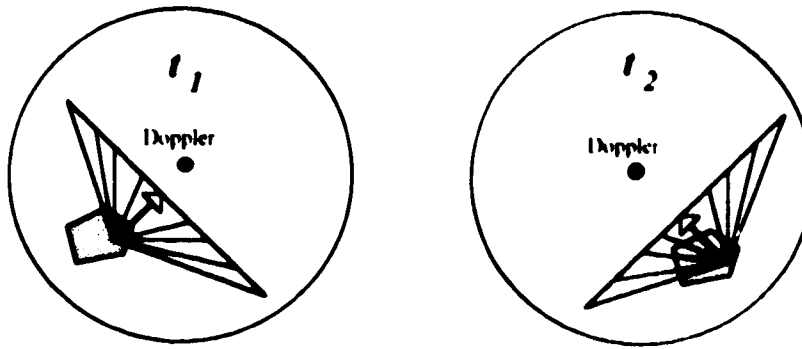


Figure 1.1 Single Doppler observations of a moving storm at two different times, t_1 and t_2 . The radial components as observed by the Doppler are shown, along with various wind vectors which could yield those radials.

The superposition of the two radar observations is equivalent to "simultaneous" measurements from two Doppler radars separated by a distance dx . Figure 1.2 shows how the two radial components determine the unique horizontal wind vector (indicated by the dark arrow).

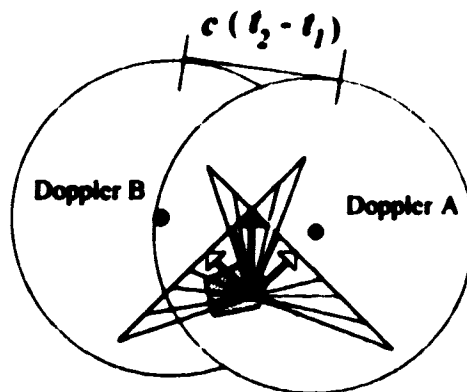


Figure 1.2 SDD horizontal wind reconstruction. Doppler radars are repositioned in space relative to the storm. Both observed radials are shown, along with the reconstructed wind vector.

In the above example, storm relative winds (i.e. internal winds) were used for clarity. Of course, a ground based radar measures ground relative winds, but exactly the same principles apply.

1.2.2 Mathematical formulation of the SDD technique

The SDD technique can be formulated in a pair of equations for the x and y components of the wind vector (u and v) in terms of the radial wind observations and the angles at which they are observed. Suppose r_1 and r_2 denote the radial wind measured at times t_1 and t_2 , with β_1 and β_2 being the azimuthal angles (from north) at which the radial components are measured. Then:

$$\begin{aligned} u &= \frac{r_1(\cos\beta_2) - r_2(\cos\beta_1)}{\sin(\beta_1 - \beta_2)} \\ v &= \frac{r_2(\sin\beta_1) - r_1(\sin\beta_2)}{\sin(\beta_1 - \beta_2)} \end{aligned} \quad (1.1)$$

This pair of equations is the two dimensional version of the "classic" dual-Doppler relations as described by Lhermitte (1970). The relevant geometry is depicted in Figure 1.3. It should be mentioned that (1.1) neglects the contribution of the vertical component of velocity to the radial component. This is a valid assumption when radar elevation angles are small (e.g. less than 5° for all cases presented in this thesis).

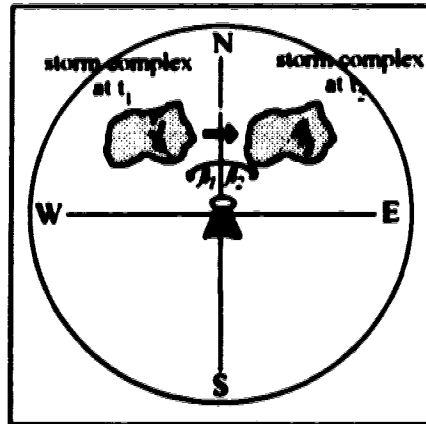


Figure 1.3 Layout for a SDD case showing observed radial components and azimuthal viewing angles of a given storm at two observation times.

1.2.3. Changes in viewing angle

Changes in azimuthal viewing angle occur in two ways. The first is the most obvious and is caused by translation of a storm, as shown in Figure 1.3. This implies that features with motion directly towards or away from the radar cannot be analyzed using the SDD technique. This is not quite true since the azimuthal viewing angle of a particular part in a storm will change due to parallax, as is demonstrated in Figure 1.4. Although the feature (a gust front in this example) as a whole has not altered its azimuth with respect to the radar, the azimuth to individual portions along the front has changed as the front approached the radar. Fundamentally, this parallax is caused by translation. A long feature is used to illustrate this effect, however the same is true for smaller features such as supercell storms, only to a lesser degree.

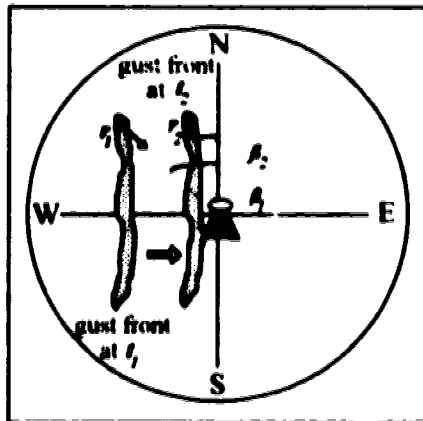


Figure 1.4 Changes in viewing angle caused by parallax.

1.3. Overview of SDD research (1968 - 1994)

Peace et al (1968) proposed the basis of the SDD technique and indicated that it has merits in analyzing single-Doppler observations of quasi-steady phenomena. They tested their methodology using a May 1967 storm passing over Oklahoma. Observations of the measured radial wind fields were fitted to two dimensional polynomials. A processing technique was developed to separate the wind field parameters through Taylor's hypothesis¹. The fitted polynomial expressions were then used to determine

¹This technique became the basis of Easterbrook's (1975) VAD extension, which in turn became the basis of various single-Doppler processing techniques such as the VVP technique of Waldteufel (1979).

expressions for the u and v component wind fields. The storm was observed simultaneously by two Doppler radars, which provided a means of testing the single Doppler technique. Comparisons were made between single and dual Doppler analyses and the results were promising. In a subsequent study, Peace et al (1969) tested their technique using simulated fields to see how well the single-Doppler technique could reconstruct a horizontal wind field, again concluding that single Doppler measurements could be used to derive horizontal motions under certain conditions.

Most researchers after 1968 have not used a parameter separation approach to deriving the horizontal wind field. Rather, the dual-Doppler calculations as described by Lhermitte (1970) are made with the synthesized (time to space) data sets. There are several reasons why this is so. First, the technique originally developed by Peace was limited to analyzing linear wind fields. Linearity in a wind field means that the spatial curvature term of the flow is small compared to the shear term (i.e. in the Taylor expansion of the wind, the second derivatives are small), which may not always be valid for mesoscale phenomena. Second, the dual-Doppler calculations are more direct. Finally, several software programs already exist to perform the dual-Doppler calculations, and only minor alterations need be made in order for these programs to run single-Doppler data sets. An example of such a program is NCAR's CEDRIC analysis package (Mohr, 1986). Krauss (1974) was the first to develop the use of the classic dual-Doppler approach to "synthetic" radial velocity data sets. This approach puts no limitations on the wind field structure.

One advantage that Peace's original method has over the classic approach is that it makes use of the data as an "ensemble" (via polynomial expressions). This may allow for the use of relatively small angular differences in the observations while giving acceptable accuracy on the retrieved wind field. Polynomial fitting of the radial wind fields also provides a good way to convert polar coordinate radar data to a regular Cartesian grid.

After Krauss' (1974) study, the single-Doppler technique remained dormant for fifteen years, until 1989. One could guess that this occurred because of the advent of multiple-Doppler radar experiments, which were subject to fewer constraints than those imposed by the single-Doppler technique. Klimowski (1990) mentions that the renewed interest is related to the installation of the NEXRAD WSR-88D radar network, which will give single-Doppler coverage throughout most of the U.S.A..

Bluestein and Hazen (1989) used the technique to analyze rainbands of Hurricane Alicia (1983) as it moved into Oklahoma, and named it the "synthetic dual-Doppler"

analysis or "SDD"². Since complete volume scans of Doppler data were available, several levels of the horizontal wind field (0.5, 1.0 and 2.0 km AGL) were retrievable. The time interval between the two observations used for the analysis was 120 minutes. The hurricane was moving at 20 km/hr, giving a synthetic dual-Doppler base line of 40 km. Their results were consistent with surface measurements, and they concluded that the technique was viable for the analysis of *mesoscale* aspects of mobile cyclones and fronts.

Klimowski and Marwitz (1990) studied a severe squall line using the SDD technique. They also used another analysis method applicable to banded precipitation systems (Banded Velocity Processing - BVP) which relies on a two dimensional assumption. Results from the two techniques and a real dual-Doppler analysis were compared. Full volume scans permitted reconstruction of the horizontal wind field up to a height of 10.5 km. The time interval used was 45 minutes, with an angular separation of 30° between the observations. Their results showed that the SDD technique worked well for the higher levels, but that the lower level did not compare well to the real dual-Doppler analysis. This was attributed to a rapidly changing wind structure in the lower levels, making the time to space conversion inaccurate. They concluded that the SDD technique can be used to investigate the kinematics of *convective* situations.

Bluestein et al (1991) tested the SDD technique with two cyclonic vortices embedded in the stratiform rain areas of mesoscale convective systems (MCS). Comparisons were made with a real dual-Doppler analysis. In both cases, they found the synthetic analysis yielded results qualitatively similar to the dual-Doppler analysis, even though the RMS speed difference between the two analyses was quite large in certain areas. One case used observations with a 90 minute difference and a baseline of 75 km. This relatively large synthetic baseline gave an analysis area about twice the size the real dual-Doppler analysis with its baseline of 40 km. The second case used a time difference of 119 minutes between observations, with a baseline of 40 km. Complete volume scans were available for both cases making reconstruction of higher level wind fields possible.

Donaldson (1992) developed software for the SDD technique and applied it to a squall line observed on the King City radar (WKR) near Toronto, Canada. Since the King City radar does only a limited Doppler scan (3 low elevation angle scans), several observations of the squall line were used in order to increase the area over which a SDD analysis could be done. The redundant information (by using several observations instead of only two) was used to test the "quasi-steady" hypothesis. The method was found to be

²The technique is sometimes referred to as "pseudo dual-Doppler" (Bluestein, 1989)

very sensitive to the advection speed of the storm. This is equivalent to having problems matching storm positions as required for the horizontal wind field synthesis.

Klimowski and Marwitz (1992) compared the SDD technique to the real dual-Doppler technique using three cases: a mature gust front, a supercell storm, and a developing squall line. Several low angle (0.5°) scans of the gust front case were used in the analysis, with time separations varying from 4 to 56 minutes and angular separations of 8 to 62° . The best comparison with the real dual-Doppler analysis was with the 19 minute time difference, corresponding to an angular separation of 38° between the observations. This reflects the compromise between the angular separation and the time interval between the observations. Full volume scans were used for the supercell and squall line cases, and results were in good agreement with the dual-Doppler analysis. They concluded that the technique was useful in analyzing mean velocity wind fields of certain quasi-steady phenomena.

The SDD notions have occasionally been used for analyzing single-Doppler data without direct mention that a known and documented technique was being used. Nelson and Knight (1987) used the quasi-steady assumption for use in a dual-Doppler analysis of a supercell storm. Nichols (1990) evaluated the speed of a descending jet associated with an MCS over southern Ontario by assuming steadiness in the wind field. Boonesteel and Lin (1977) used the SDD ideas to obtain conceptual information on supercell storms. Their study is exceptional in that the radial data sets used were from *different* storms, one near Union City, Oklahoma in 1973 and the other near Davis, Oklahoma in 1972. Airborne Doppler measurements are also related to the SDD technique in that it is assumed that the wind structure is quasi-steady during the data acquisition period. The time acquisition period for a given area of a storm is typically only a few minutes and, unlike in the SDD technique, no time-to-space conversions are done. Watson (1993) and Dowell (1993) investigated supercell storms using airborne Doppler. Wakimoto et al (1993) used similar techniques to study an intense Atlantic cyclone.

1.4. Research and "operational" Doppler weather radars

Research Doppler weather radars can be controlled to some degree by the users to meet the objectives of a specific experiment. In addition, premium hardware (e.g. large radar dish) is usually used giving optimum performance and resolution. Information processing and display is performed by "state-of-the-art" computers (e.g. CRAY super computer) and workstations (e.g. Silicon Graphics).

Having a primary mandate to support forecast operations, "operational" Doppler weather radars have specific tasks which cannot be interrupted by research experiments. Further, these radar units usually consist of moderate hardware (e.g. small radar dish) and have limited computing facilities for information processing (e.g. DEC VAX minicomputer) and display (e.g. IBM PC).

The Atmospheric Environment Service (AES) of the Canadian government manages two *operational* Doppler weather radars. The King City radar, located near Toronto, began operations in 1986. It is identified internationally by the letters "WKR". Development for the Canadian Doppler radars is done at the King City radar facility by a team of AES scientists. A second Doppler, the Carvel radar (WHK), began operations near Edmonton, Alberta, in 1990. The AES plans to install several more Doppler radar units over the next few years.

The AES Doppler radars have a varied agenda. The radar goes through a routine of Doppler (velocity, reflectivity and spectral width) and conventional (reflectivity) measurements (see Glossary). This routine repeats at 10 minute intervals.

In the non-Doppler measurement mode, the radar scans 23 elevation angles in a 5 minute period to produce a three dimensional grid of reflectivity data. Such a scan is often referred to as a "full" volume scan (Figure 1.5). Data from the volume scan is used to produce various display products for operational forecast use, which include the CAPPI, MAX R, ECHO TOPS and SEVERE displays (see Glossary).

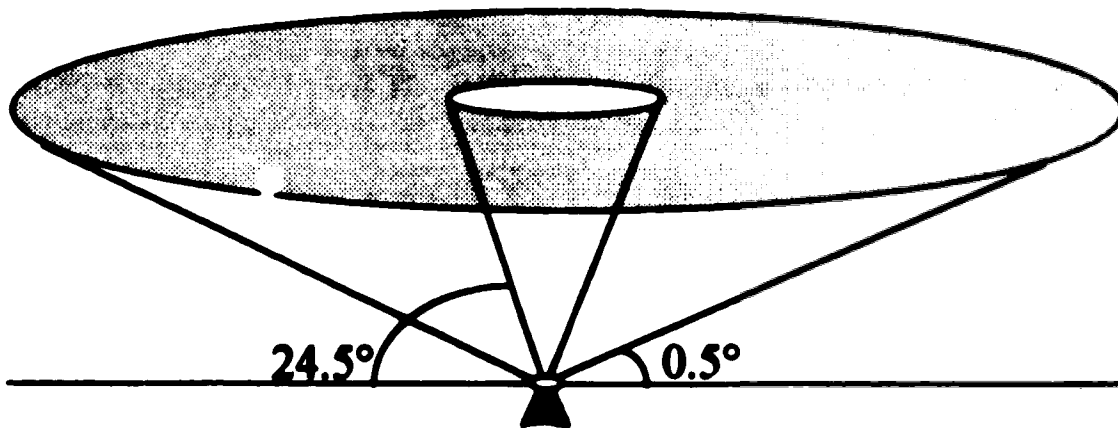


Figure 1.5 The conventional mode "full" volume scan for the AES Doppler radars. The volume sampled by the radar (shaded) encloses 98% of the volume below 15 km within a radius of 113 km (neglecting refraction and the Earth's curvature). The angles have been distorted for clarity.

The radar then goes into a Doppler mode and scans at four elevation angles, typically 0.4° , 0.5° , 1.5° and 3.5° (Figure 1.6). Only four elevations (i.e. limited scan) are possible because the antenna rotation rate must be reduced considerably when doing Doppler measurements. Hardware details of the AES radar units are provided in Appendix A.

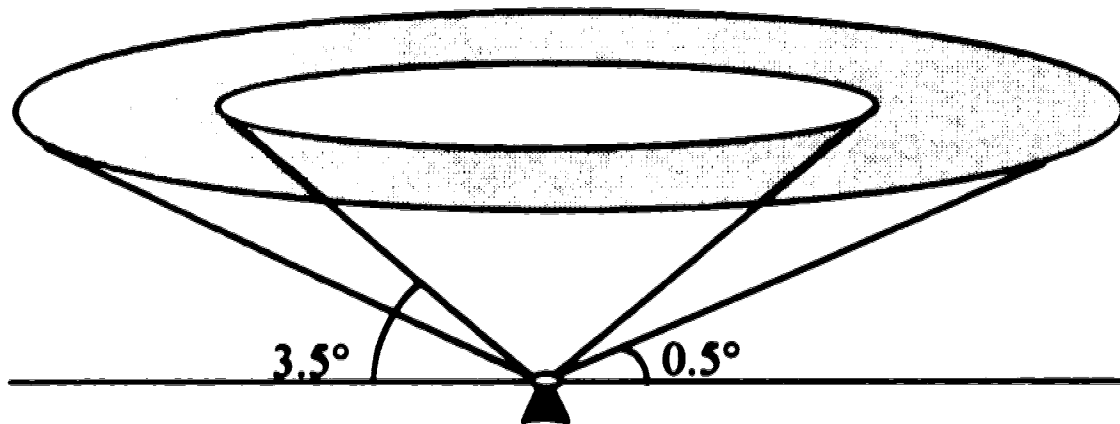


Figure 1.6 The Doppler mode limited scan for the AES Doppler radars. The volume sampled by the radar (shaded) encloses only 40% of the volume below 15 km within a radius of 113 km (neglecting refraction and the Earth's curvature). The angles have been distorted for clarity.

The limited Doppler scan of the AES radars has several important implications for the SDD technique. These will be discussed in the next chapter.

1.5. Objectives of this thesis and approach to the research

Being relatively inexpensive to operate, single Doppler radar units are more common than dual or multiple Doppler arrangements. In Canada, there are three: the two units operated by AES, and one near Montréal run by McGill University. In addition, the University of Toronto owns a portable unit. In the United States, a network of single Doppler units (NEXRAD) is in the process of being installed and will soon provide Doppler coverage over most of the states (Klazura and Imy 1993). With all these data becoming available to operational forecasters, much effort is now being devoted to the development of techniques to interpret single Doppler data.

Significant research on the SDD technique has been done in the last few years. With the exception of Donaldson (1992), however, cases analyzed were based on data

from Doppler radars which offer full volume scans. As mentioned in the previous section, the AES Doppler radars do provide a full reflectivity volume scan, but the Doppler scans are done only at very low elevation angles due to time constraints.

This thesis has three major objectives. The first objective is to investigate the effect of various error sources on SDD derived wind fields. These include inaccuracies in the measured radial components due to shear and turbulence, errors in matching radial components at two times and errors caused by the evolution of a wind field. The various sources of error will be discussed in chapter 2.

In order to do this investigation of error sources for the SDD technique, a computer program was designed to do SDD wind field reconstructions based on radial wind fields generated from an initial wind field. This program can be thought of as a SDD simulator. Various realistic error producing processes can be simulated by modifying the generated radial wind fields before a wind synthesis is attempted. The dependency on viewing geometry can be examined, and comparisons may be made between statistical calculations and simulator output.

The second objective is to determine whether or not the SDD technique is feasible and/or useful when based on limited Doppler scans, either for case studies or for real-time operational use by forecasters. An example of this is the possibility of studying and/or detecting mesocyclones which can eventually spawn tornadoes.

The means of satisfying the second objective eventually led to a third objective to develop an SDD analysis package for an operational Doppler weather radar which could potentially be used for real-time applications. In keeping with the operational aspects of this objective, it was determined that the analysis package should have the following characteristics:

1. Fast, graphically based, user-friendly and robust.
2. Can be run on a relatively inexpensive personal computer (e.g. IBM 486).
3. Incorporates a rapid display of both the absolute (ground relative) and the storm relative horizontal wind field.
4. Includes a display of the vorticity and divergence of the synthesized wind field.

The means of satisfying this third objective involved a significant amount of time in coding and design. The resulting "SDD analyzer" was used to address the second objective.

1.6. Outline of subsequent chapters

Chapter 2 deals with the limitations and inaccuracies of the SDD technique. The configuration of precipitating systems with respect to the radar as related to the wind field reconstruction is also discussed.

The computer program design, implementation and use of both the SDD simulator and the SDD analyzer are presented in Chapter 3. The development of these programs comprised a significant part of the research undertaken. Details on the code are provided in Appendix C and the source code is included on a magnetic disk in the thesis cover.

Chapter 4 consists of the sensitivity tests on the SDD method using the simulator. The effects of spectral noise and imprecise matching of radial wind fields are examined. Evolution of a wind field structure is simulated to see its effects on SDD wind fields. In order to represent a realistic case, a simulation is done using a combination of noise, imprecise matching and wind evolution. The effects of viewing geometry using realistic data are investigated, both statistically and with the simulator. Finally, a statistical treatment is done to determine which biases the SDD analysis may introduce to the synthesized wind field. These biases are analyzed with the simulator program.

Chapter 5 consists of SDD analyses on real weather cases. Three cases from the Carvel weather radar near Edmonton are presented. The first is a gust front, the second is a severe storm, and the last is a tornadic storm. All three cases occurred in the summer of 1993 over central Alberta. Interpretations are made on the analyses obtained.

In Chapter 6, a tornadic storm which was observed by the King City radar near Toronto on July 24, 1987, is analyzed.

The final chapter summarizes the findings of the research undertaken. Suggestions are made for future work on the SDD technique, particularly as pertains to operational radars.

2. Limitations and inaccuracies in the SDD technique

2.1. Error analysis of the basic wind synthesis equations

An error analysis on (1.1) gives some insight into the limitations and inaccuracies of the SDD technique. The determination of the horizontal wind vector at a given point depends only on the viewing angles and the radial velocities at that point for the two observations. Therefore, errors in the horizontal wind field (du and dv) depend only on these variables and the accuracy to which they are known. Expressions for these errors can be derived from (1.1)

$$\begin{aligned} du^2 &= \frac{(\cos^2 \beta_2 + \cos^2 \beta_1) dr^2 + f(r_1, r_2, \beta_1, \beta_2) d\beta^2}{\sin^2(\beta_1 - \beta_2)} \\ dv^2 &= \frac{(\sin^2 \beta_1 + \sin^2 \beta_2) dr^2 + f(r_1, r_2, \beta_1, \beta_2) d\beta^2}{\sin^2(\beta_1 - \beta_2)} \end{aligned} \quad (2.1)$$

where it is assumed that the radar measurement errors are the same for both observations (i.e.: $dr_1 = dr_2 = dr$ and $d\beta_1 = d\beta_2 = d\beta$). The $f(\dots)$ terms are lengthy and involve the cosine and sine functions.

A scale analysis of (2.1) reveals that the error due to the $d\beta$ terms is about 100 to 1000 times smaller than that due to the dr terms. This then leads to simplified expressions for the error in the horizontal wind:

$$\begin{aligned} du &= \frac{dr \sqrt{\cos^2 \beta_2 + \cos^2 \beta_1}}{\sin(\beta_1 - \beta_2)} \\ dv &= \frac{dr \sqrt{\sin^2 \beta_1 + \sin^2 \beta_2}}{\sin(\beta_1 - \beta_2)} \end{aligned} \quad (2.2)$$

2.2. The quasi-steady and azimuthal motion requirements

Inherent to the SDD technique is the requirement that the wind structure within the storm remain quasi-steady between the observations to allow for the time to space conversion. In addition, the storm being observed must undergo significant azimuthal movement between the observations so as to make the wind synthesis calculations reasonably accurate. As a rule of thumb, an azimuthal change of 20° or more is needed to get a useful reconstruction of the wind field. Figure 2.1 shows the relationship between angular velocity, w , and range, R . Curves for various tangential velocities, v_t , are plotted. As expected, shorter ranges and higher tangential velocities lead to higher angular velocities. For example, a storm moving at a tangential speed of 15 m/s and at a current range of 50 km would undergo an azimuth change of about 10° in 10 minutes. As such, the storm would have to be quasi-steady for at least 20 minutes in order to get a usable set of observations.

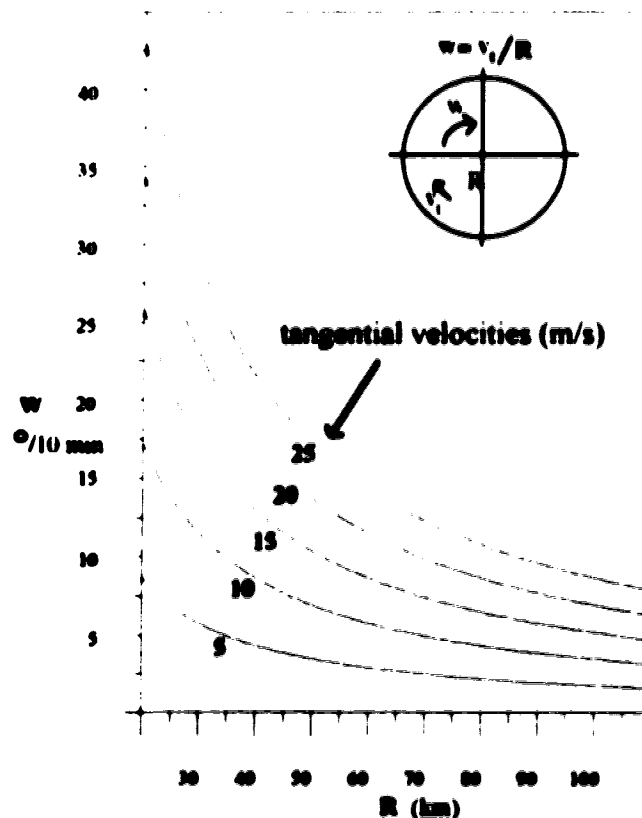


Figure 2.1 Relationship between angular velocity, w , and range, R , for various tangential velocities.

A delicate balance exists between the time interval used in an SDD analysis and the angular separation obtained during that time. Accuracy of the calculations increases for larger angular separations, but may decrease due to the evolution of the wind field over a long time interval. Similarly, a short time interval may help to validate the quasi-steady requirement, but leads to inaccuracies caused by a small angular difference. For example, a case with 20°/20 minutes may yield better results than a case with 40°/40 minutes or 10°/10 minutes.

2.3. The influence of storm viewing geometry on the synthesized wind field

Equation (2.2) shows the sensitivity of the SDD technique to the difference in the angles from which the storms are viewed. The sinusoidal relationship in the denominator implies that errors are minimized when the two storm observations are at right angles. Errors are large if the storm or feature is moving almost along a radial ($\beta_1 \sim \beta_2$) or when the feature passes over the radar ($\beta_1 \sim \beta_2 \sim 180^\circ$).

The accuracy with which the wind field is reconstructed also depends on the orientation of the true wind vector with respect to the "radars". An extensive analysis of errors involved in a dual-Doppler wind field reconstruction was reported by Doviak and Ray (1976). It is shown that the best wind magnitude estimates are obtained when the true wind is aligned along the bisector of the angle subtended between the radars and the analysis point. The best wind direction, however, is obtained when the true wind is aligned perpendicular to this bisector (Figure 2.2).

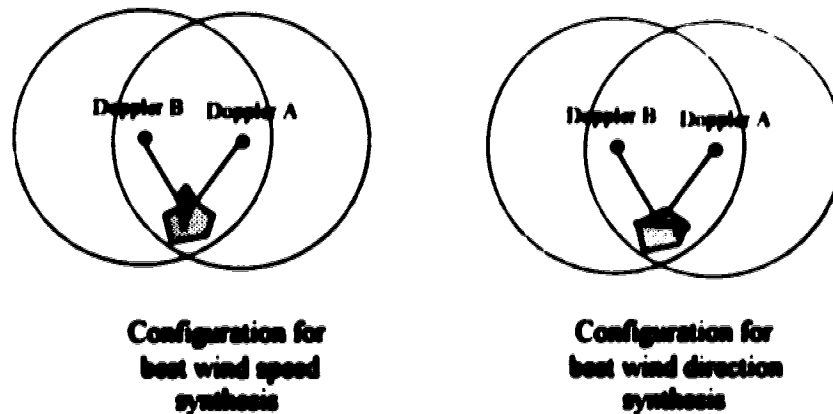


Figure 2.2 Optimum true wind vector orientation for synthesis of wind speed and wind direction using two Doppler observations.

2.4. Error sources in the SDD technique

2.4.1 Measurement of radial components

In order to obtain meaningful estimates of radial velocity, the measurement of the phase change (Doppler effect) between two pulses of energy for a given location is repeated many times. On the AES Doppler radars, 65 pulses are used, giving 64 pairs of measurements from which to compute radial velocities. A Fast Fourier Transform (FFT) signal processor then computes a spectrum of radial velocities, along with its mean and standard deviation. The standard deviation of the spectrum is called the spectral width, σ_r , and is fundamentally caused by turbulence and shear within the volume being sampled. Typically, σ_r varies from about 1 m/s in stratiform precipitation to over 4 m/s in strong convective situations. The uncertainty in the mean value of the radial velocity, σ_v , is a function of σ_r and other parameters. Doviak (1984) shows that, for a Gaussian spectrum with relatively narrow σ_r , σ_v can be approximated as:

$$\sigma_v^2 = \frac{\lambda^2 (PRF)^2}{4M} \left[\frac{\sigma_r}{\sqrt{\pi} PRF \lambda} + \frac{32 \sigma_r^2}{(PRF)^2 \lambda^2 SNR} + \frac{1}{12 (SNR)^2} \right] \quad (2.3)$$

where λ is the operating wavelength of the radar, M is the number of paired measurements for a given sample, PRF is the pulse repetition frequency and SNR is the signal-to-noise ratio¹. For large SNR's, the first term is dominant. Using a PRF of about 1000 Hz, 64 pulse pairs and a wavelength of 5 cm, we can then approximate the uncertainty in the mean as:

$$\sigma_v \approx 0.33 (\sqrt{M}) \sqrt{\sigma_r} \quad (2.4)$$

Spectral widths of 3-6 m/s in strong convective situations then translate to radial velocity errors of 0.5 to 0.8 m/s. The second and third terms in (2.3) can however contribute significantly to σ_v under typical conditions. Crozier (1986) mentions that for the King City radar, mean radial velocity estimates of a given volume measured at different PRF's differ

¹See Doviak (1984), p. 108, equation 6.26.

by an average of about 3 m/s. Using addition of errors in quadrature, this suggests that σ_r is typically about 2 m/s.

Uncertainties in the azimuth of the radar beam also lead to errors in the radial component at a given location. These errors are proportional to wind shear at that location. Under strong shear conditions, a random uncertainty in the beam pointing azimuth of 0.1° will cause an error in the radial velocity of about 1 m/s (Doviak 1976). Radial velocity errors due to inaccurate beam positioning are therefore of the same order as those due to spectral noise, giving a combined σ_r of up to 3 m/s. Systematic errors in azimuthal beam positioning may also exist and will cause additional errors in the radial component velocities.

2.4.2. Resolution problems of the radar

The beamwidth and pulse length of a radar unit determine the spatial resolution with which the properties of targets are measured. The angular resolution decreases with range as the beam widens, however the pulse length fixes the lengthwise dimension of the volume being sampled. For example, using a beamwidth of 1 degree and a pulse length of 0.5×10^{-6} s, a volume sampled (or "pulse volume") at 30 km can be approximated as a cylinder with a diameter of 0.5 km and a length of 75 m. At 90 km, this cylinder increases to a diameter of 1.5 km but retains the length of 75 m. The range of targets must therefore always be taken into account when using radar data since significant "blurring" occurs at longer ranges.

Thus far, the limitations discussed apply equally to a real dual-Doppler arrangement and to a SDD setup. The following limitations, however, are particular to the SDD technique.

2.4.3. Determination of the advection vector

A problem that can arise from using synthetic "radars" is that these radars also have synthetic positions relative to the storm, as determined by the storm advection vector. This means that the positions of the storms which have their radial wind fields matched for the SDD analyses must be accurately known. The effect of not knowing these positions precisely increases Δr in (2.2) since radial components from different parts of a storm are matched. For features with relatively weak horizontal wind field gradients, the accuracy with which the storm positions are determined is not so important. However, for features with strong horizontal wind shear, such as mesocyclones, the storm positions are

critical to the analysis. In a broad sense, inaccuracies of x km's in the storm positions will "blur" features with dimensions smaller than x km (Klinowski 1992). Furthermore, artifacts may be created in the wind field as a results of these inaccuracies.

Determination of the advection vector is often a major source of error in the SDD technique. Additional problems can arise when the advection of a feature cannot be described by a single vector, as pointed out by Nelson and Knight (1987).

2.4.4. Steadiness of the internal wind structure

A significant error source stems from time variations in the internal wind structure. These errors show up in (2.2) as an increase in Δr . The quasi-steady requirement puts limitations on the time interval between the radial wind field observations used for the SDD analysis. Typically, a usable time interval for supercell storms would be in the 20 to 60 minute range, while more persistent gust fronts or rainbands may allow for time intervals of 40 to 90 minutes. Without the use of a real dual-Doppler, the only way to test that a particular feature is quasi-steady is to compare two or more SDD analyses using three or more radial wind field observations (Krauss 1974).

2.5. Restrictions on the SDD technique caused by limited scan Doppler radars

Limited Doppler scans impose restrictions on the use of the SDD technique. First, for a given elevation angle, the height of a storm which can be examined depends on range. At 30 km, the 0.5° - 3.5° scans will penetrate features from average heights of 700 to 1800 m. Out to a range of 90 km, these same scans penetrate at average depths of 1200 to 3300 m.

A more severe restriction on the use of the technique comes from the fact that at least two observations of a feature are needed for an SDD analysis. Unless the motion of this feature is strictly azimuthal, the height at which it is penetrated by the radar beam will change between observations. In the subsequent synthesis of horizontal winds, radial components originating from the same horizontal location in the storm will actually come from different heights. Under strong vertical shear conditions, this can be a dominant source of error for the SDD technique.

Although it may sometimes be possible to use information from more than one elevation angle in order to construct a "pseudo-CAPPI" of the Doppler information, the conditions where this works are extremely limited. There is no way around this problem, and it limits use of the SDD technique to cases where the storm or feature advection is

largely azimuthal. In order to "keep tabs" on the accuracy of the technique, average beam heights and their changes between the two observations being compared can be calculated. Estimates of acceptable height changes can be made by considering typical vertical wind shears.

3. Development of computer programs

Two core programs have been developed to test and utilize the SDD technique. The first program is a SDD simulator, the second is an actual SDD analyzer. Both programs are written in the C programming language and run on IBM compatible personal computers. The source code for the programs is included on a magnetic disk in the thesis cover. Details on the program structure can be found in Appendix C.

3.1. A synthetic dual-Doppler simulator

The SDD simulator takes an initial wind field and generates the radial wind fields that a Doppler radar would have observed at given positions. The Doppler "observations" are then used in the SDD technique to reconstruct the horizontal wind field. Finally, the initial and reconstructed wind fields are compared. Using the simulator, it is possible to investigate the influence of angular separations between observations, wind orientations, spectral noise and storm positioning on SDD wind field reconstructions. An outline for the SDD simulator is shown in Figure 3.1. The major components are discussed briefly in the following subsections.

3.1.1. Program inputs

The first entry in the program specifies a filename for a hypothetical horizontal wind field. This file consists of 2 NxN matrices, one each for the u wind and v wind components. These regular grids (matrices) determine the u and v wind fields once a spatial resolution (i.e. grid spacing) is chosen. Typically, matrices of 67x67 elements are used with a resolution of 1 km. The next entry is the elevation angle of the radar which is used to calculate average radar beam heights. The mean radial component standard deviation (m/s) is then entered. It is used to add random error to Doppler observations generated from the initial wind field. Finally, the positions (range and azimuth) of the given wind field for the first and second observations are specified.

3.1.2. Radial component generator

The position of a feature relative to the radar is used to derive the radial components of the horizontal wind field for that feature. This is done for both

observations. Since realistic storms and gust fronts are relatively large, the difference in viewing azimuth from one part of the feature to another is taken into account. Spectral noise may then be added to the radial component wind fields with a standard deviation as specified in the program input.

3.1.3. SDD analysis

Since this program is designed to simulate the use of the SDD technique on limited scan radars, average radar beam heights are calculated for both observation times. Beam heights and their change between observations are displayed. This helps to keep track of errors that may be occurring in cases of strong vertical wind shear. The standard 4/3 Earth refraction model is used to compute the heights (Doviak and Zmic 1984). The generated radial component wind fields are then displayed using conventional Doppler shift colors (red-away, blue-towards).

Next, using the dual-Doppler equations (1.1), the horizontal wind field is reconstructed and its RMS difference with the original wind field is computed. Only the radial component fields (with spectral noise) and their orientations are used in these calculations. Once the resultant wind field is displayed, the position of either radial component wind set can be interactively adjusted. If an adjustment is made, the SDD calculation is repeated, and the new wind field is displayed. Smoothing is done on the resulting wind field before it is displayed (see Appendix B). Finally, the vorticity and divergence fields are computed (centered finite difference scheme) and displayed.

3.2. A synthetic dual-Doppler analyzer

The SDD analyzer uses two Doppler observed radial wind fields and their positions to reconstruct the horizontal wind field which is consistent with those observations. The program has been designed to accept input from either the Carvel or the King City Doppler weather radars but could easily be adapted to accept input from other radars. The analyzer can also be used in conjunction with output from the SDD simulator to examine the effect of temporal changes in a wind structure on a SDD analysis. The workings of the SDD analyzer are outlined in Figure 3.2.

The archived radar data undergoes a considerable amount of preprocessing before being used by the SDD analyzer.

The first step is to retrieve and decode the two required radial wind fields from the optical platter archives. A decode program¹ reads the archived files and allows the user to select the azimuths, ranges and elevation angles of the data to be decoded.

The radial velocity data are then converted from polar coordinates (inherent to sweeping radars) to regularly spaced Cartesian coordinates. The resultant uniform resolution in the radial velocity data facilitates SDD comparisons between data from different positions on the radar scan. The program which does the conversion puts polar coordinate data into their nearest corresponding locations in a user specified Cartesian grid. If two polar coordinate data points fall in the same Cartesian grid cell, then the one nearest to the center of the Cartesian cell is kept and the other discarded. Cressman (1959) developed a more sophisticated interpolation method but it is not implemented in this program.

The maximum radial velocity which can be measured by a Doppler radar without ambiguity is given by (Crozier 1986):

$$r_u = \frac{PRF \lambda}{4} \quad (3.1)$$

where λ is the radar's operating wavelength and PRF is the pulse repetition frequency. Radial velocities exceeding the maximum unambiguous velocity are aliased (or "folded") and are indistinguishable from unaliased data. To correct this velocity folding, the velocity measurements must be de-aliased in some way. As described by Crozier (1986), the Carvel and King City radars use a dual-PRF technique to de-alias velocity data to an unambiguous radial velocity of 48 m/s. The dual-PRF technique is applied before the data are archived and accurately "unfolds" the data under most conditions. Unfolding errors can however occur in areas of strong horizontal shear. Once a Cartesian grid has been filled (for use in the SDD technique), an attempt is made to correct these unfolding errors. This is done by adding or subtracting multiples of 2x12 or 2x16 m/s to the radial velocity component at one grid location until the difference between it and neighboring data is

¹Provided by Tom Nichols of the Atmospheric Environment Service, Edmonton, Alberta.

minimized. The values of 2x16 and 2x12 m/s represent the possible folds that can occur in the data. They are related to the AES C band radar (5 cm) dual operating PRFs of 892 Hz and 1190 Hz.

The last step in the data pre-processing is a rejection of data which do not seem to fit well in the data set. This is done by comparing values at grid locations with neighboring data. If the difference is above a certain threshold, the data at that location are rejected. Data eliminated in this way are usually values which were incorrectly de-aliased and in which the latter procedure failed to recover the data properly.

Details of the data preprocessing are contained in Appendix B.

3.2.2. Input of case characteristics

Once the two radial component sets are obtained, characteristics of the particular case being analyzed are entered into the program. This includes the position of the center of the storm at both observation times, grid scale information and the elevation angle of the radar scan.

3.2.3. SDD analysis

Finally, the actual SDD analysis is performed. The average height of the radar beam is calculated for various parts of the storm on both sets of data. As in the simulator program, the standard 4/3 Earth model is used to compute the heights. The height calculations are important because of the variation of height (with range) on a conical surface such as the PPI. Differences of beam height between the two observations are also computed. Although these values are not used in the SDD calculations, they are needed to verify that the data being compared are at similar heights. If the two heights differ significantly, an SDD analysis may not be appropriate (section 2.5).

Next, the two radial component wind fields are displayed for verification by the user. The SDD calculations are then made and the ground relative wind field is displayed. The range and azimuth of either radial component wind set can then be interactively adjusted. If an adjustment is made, the SDD calculation is repeated, and the new ground relative wind field is displayed. Smoothing is done on the resulting wind field before it is displayed.

Similarly, the storm relative wind field is displayed and interactive adjustments can be made. Finally, the divergence and vorticity fields are computed and displayed, using the adjusted positions for the radial wind fields.

3.3. Interactive adjustment of storm positions using "sliding windows"

The simulator and analyzer programs are designed such that the positions of the storms can be adjusted while running the program. This presents a significant advantage over using existing dual-Doppler software packages for doing SDD analyses, as done by most SDD researchers. With dual-Doppler software, there is no reason to allow for an adjustment of storm positions since only one observation of the storm is used and its position with respect to the radars is well known. Run-time adjustment is important as it allows "fine tuning" of the SDD analysis by giving immediate feedback on the resulting wind field. The reason one is able to do fine tuning when the true wind field is unknown is that relatively small inaccuracies in the storm positions can lead to unrealistic wind fields (section 2.4.3).

The method used to allow for this interactive adjustment is to decode and preprocess areas of data larger than that initially needed. The user can then "slide" around in the data area to choose the subset of data desired. Figure 3.3 illustrates this procedure. The example shows that the data subset position can be adjusted. Only one observation is shown in the figure, however both observations of the radial wind field can be adjusted. Figure 3.4 shows how the SDD analyzer displays the current offsets of the sliding windows.

Being able to perform this adjustment at run-time is very useful when doing case studies. If an SDD analyzer were intended to be used by operational forecasters, run-time adjustment would be crucial.

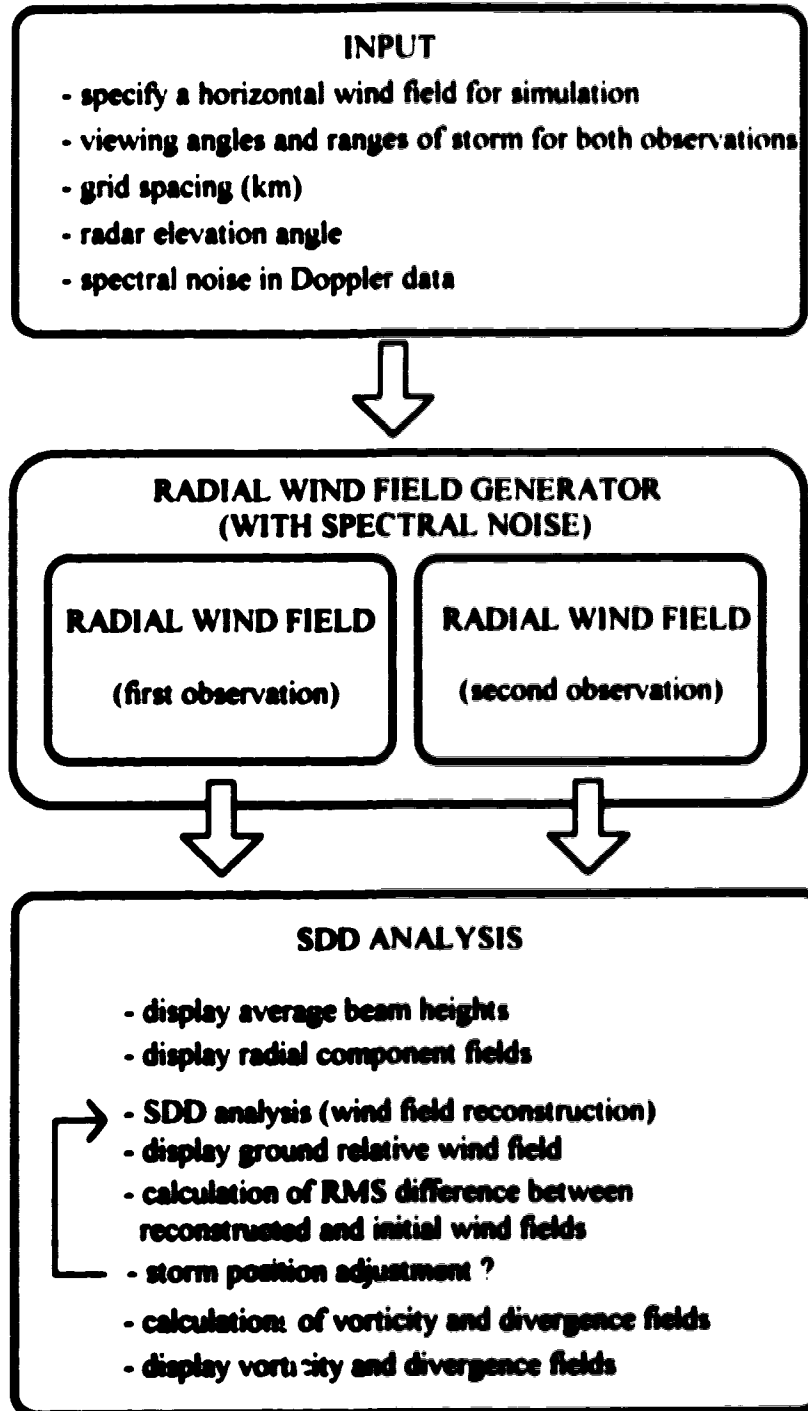


Figure 3.1 Outline of the SDD simulator program.

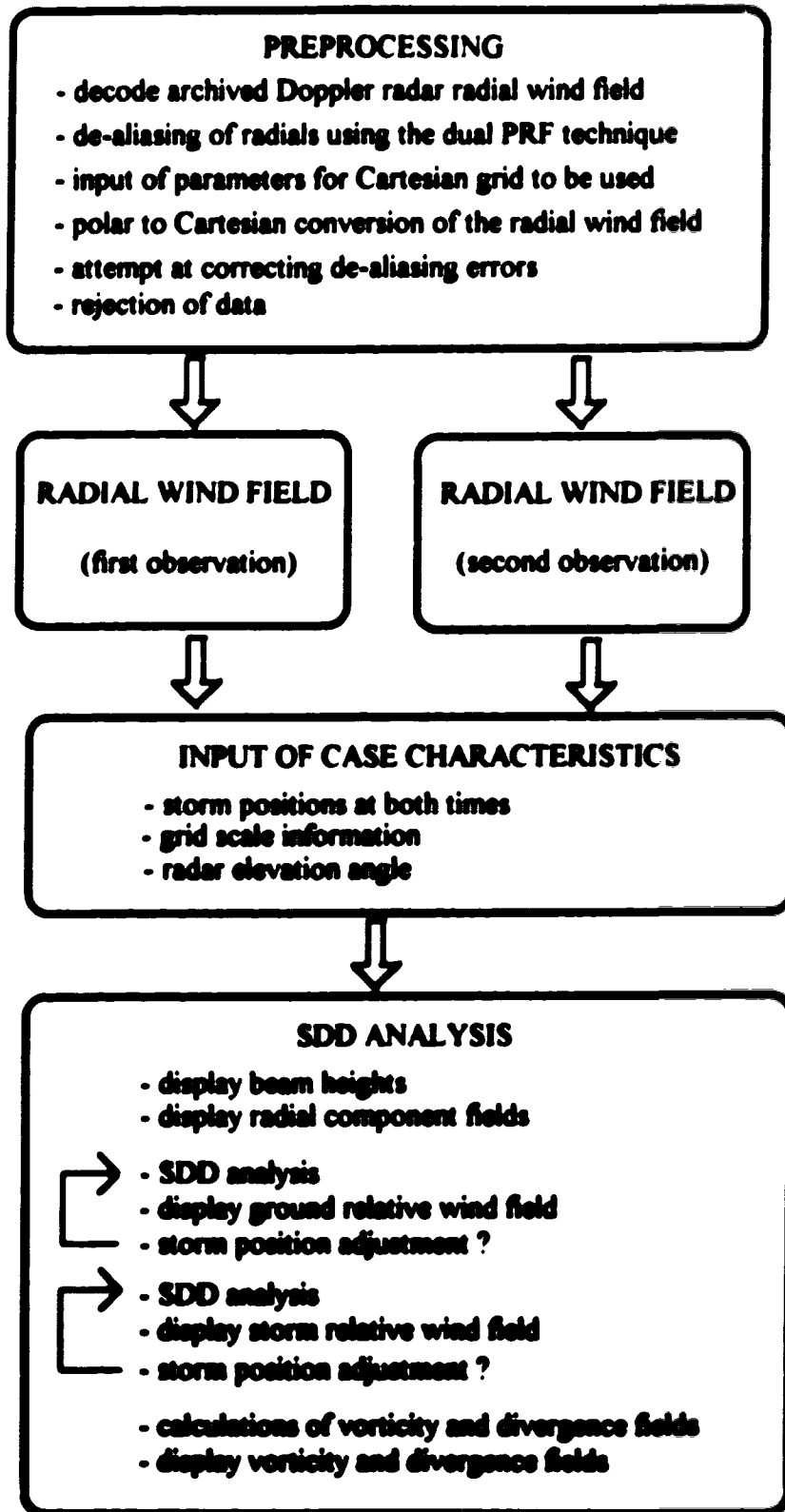


Figure 3.2 Outline of the SDD analyzer.

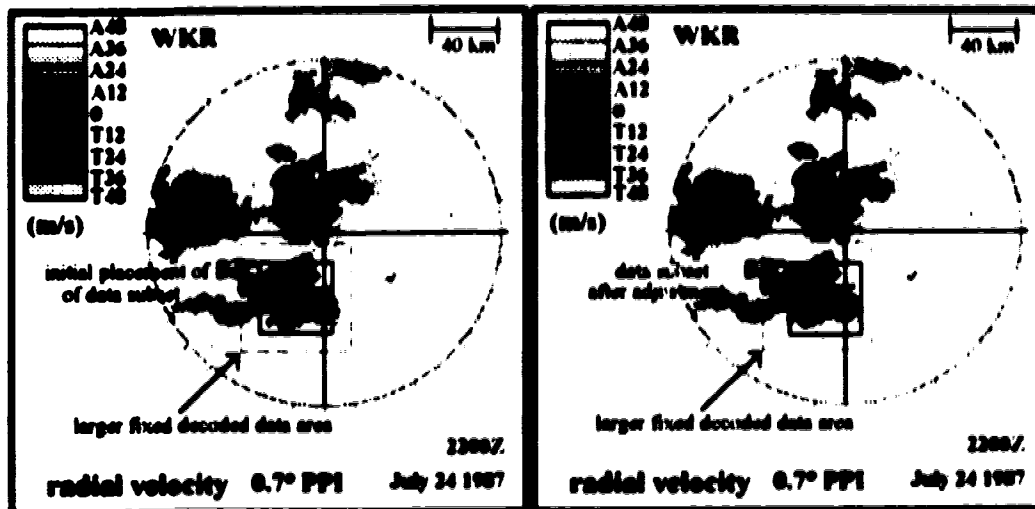


Figure 3.3 "Sliding windows". The solid window on the velocity field indicates the area used for the SDD analysis. The larger window is the area within which the smaller window can be slid to adjust the analysis. Such an adjustment can be made to both observations of the radial wind field.

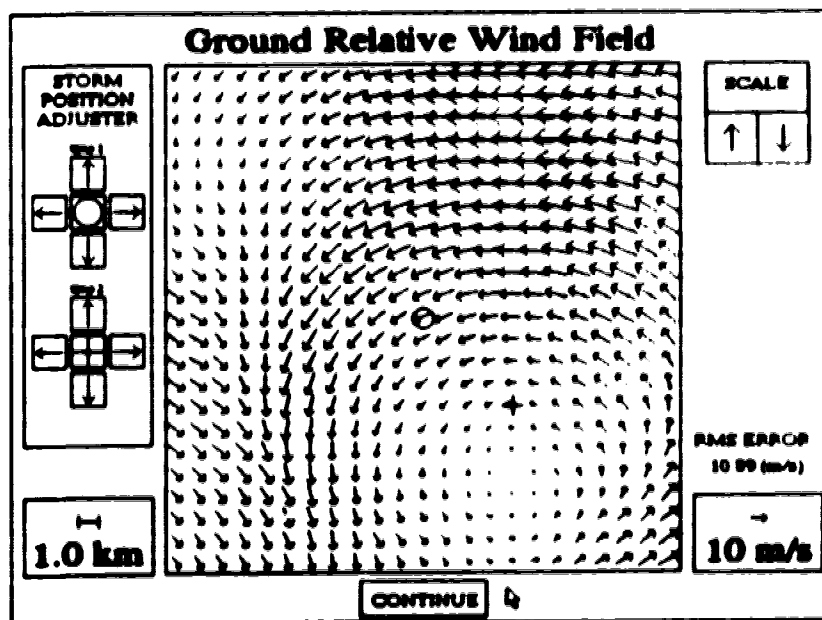


Figure 3.4 Using "sliding windows" on the SDD analyzer. The circle indicates the offset from center of the storm area for the first observation, and the cross indicates the offset for the second storm area. Either storm area can be moved relative to the other. The "storm position adjuster" buttons on the left are used to make the adjustments

4. Sensitivity tests on the synthetic dual-Doppler technique

The simulator described in the previous chapter is used to test the sensitivity of the synthetic dual-Doppler technique. The influence of inaccuracies inherent to Doppler wind observations is considered, as well as the effect of inexact storm position matching and a non-steady wind field. The degree to which angular separation and wind orientation affects the synthesis of a wind field is examined and a positive speed bias is linked to noisy data.

A "typical" mesocyclone is used in many of the simulations. Its characteristics are taken from Burgess' (1976) study. It consists of a Rankine combined vortex ¹ with a radius of 2.85 km and an outer rim speed of 22 m/s. The area analyzed is 22.5 km by 22.5 km at a resolution of 0.5 km. The average wind speed within this domain is 9.82 m/s. This mesocyclone is referred to as a "Burgess mesocyclone" in this chapter.

4.1. Errors caused by spectral broadening mechanisms

Turbulence, shear and imprecise beam pointing result in spectral errors to the radial wind field of 1 to 3 m/s (section 2.4.1). The SDD simulator can be used to examine the relationship between these spectral errors and the accuracy of a synthesized wind field.

As an example, a Burgess mesocyclone is placed at a range of 60 km, with 20° between the Doppler observations. Results show that the general features of the mesocyclone are easily recognizable with errors up to 3 m/s (Figures 4.1A-B). However, the RMS speed errors are quite large relative to the mean initial wind speed. With uncertainties of 3 m/s, the RMS speed error is greater than the initial mean flow, yet the overall pattern is quite similar to the initial field. Simulations have also been done with spectral noise of 4 and 6 m/s (Figure 4.1C). Significant deterioration of the wind field is noted at 4 m/s, and the pattern is almost totally obliterated with errors of 6 m/s.

Since a Burgess mesocyclone contains winds of various directions and speeds, the above findings are also relevant to observations of an arbitrary wind field where the Doppler measurements are separated by about 20°.

¹Such a vortex (Rankine 1901) consists of solid body rotation within the outer rim and a 1/r decrease in flow beyond the outer rim.

4.2. Errors caused by imprecise storm position matching

The problem caused by imprecise matching of radial wind fields was mentioned in section 2.4.3. In this section, the simulator is used to portray the effects of incorrect storm positioning and to determine the magnitude of the problem.

Simulations were done using a Rankine vortex with a radius of 3.0 km (Figure 4.2A). Results of the simulations (Figures 4.2B-C) show that the overall cyclonic pattern is recognizable for position mismatches of 1.4 km. A mismatch of 5.7 km, however, completely deforms the pattern. As compared to the mesocyclone dimension, this means that a mismatch of 30% is tolerable. A mismatch on the order of 200%, however, destroys the pattern and creates artifacts in the wind field. This is consistent with the conclusion that an error in storm positioning of x km will obliterate features smaller than x km (section 2.4.3).

Storm position sensitivity simulations have been done for a Burgess mesocyclone. They illustrate the asymmetric effects of storm positioning (Figure 4.3). The results are presented in terms of *error ratios*, defined as the ratio between the RMS error in the wind field reconstruction and the average wind speed of the initial field. Error ratios are shown for adjustments perpendicular and parallel to the average viewing angle from the radar. The curves show that the analysis is significantly more sensitive to inaccuracies in azimuthal positioning than it is to range errors. Further, the sensitivity is not symmetrical about the average viewing angle. Although similar asymmetries should occur for an arbitrary wind field, these particular observations are specific to mesocyclones. A downburst, for example, should show asymmetries with the opposite behavior.

General conclusions about the effect of inexact positioning can be made by considering the strength of horizontal wind shears which occur in mesoscale features. For the Burgess mesocyclone, the radial component shear is about $8 \times 10^{-3} \text{ s}^{-1}$ (or 8 m/s per km), meaning that positioning errors as small as 0.5 km can contribute more to error in the radial velocities than spectral noise. A more typical shear for larger mesoscale features is about $1 \times 10^{-3} \text{ s}^{-1}$ (or 1 m/s per km), implying that positioning errors of 1 to 3 km contribute to Δr on the same order as spectral noise.

Our findings suggest that storm position matching is potentially one of the biggest problems associated with the SDD technique. For this reason, run-time adjustment of the storm positions, as described in section 3.3, is essential to an operational SDD analyzer.

4.3. Errors caused by height changes (on limited scan radars)

When a complete radar volume scan for a given case is not available, vertical shear can cause a similar problem to that of imprecise storm positioning. A "mismatch" occurs when the radial velocity fields used for SDD analysis are taken from significantly different ranges on a PPI scan (section 2.5). Unlike positioning errors in the horizontal, no adjustment can be made to minimize the mismatch in the vertical because of the limited Doppler scan.

This problem is significant when strong vertical wind shears are present. Weisman (1986) classifies strong vertical wind shear as being greater than 5 m/s km^{-1} . For example, a vertical wind shear of 10 m/s km^{-1} gives a *maximum* error in the radial components of 1 m/s per 100 m . This implies that, under strong shear conditions, height differences of $100\text{-}300 \text{ m}$ can give errors in the radial wind field comparable to spectral broadening errors. Under more typical shear conditions of about 3 m/s km^{-1} , heights differences of $300\text{-}900 \text{ m}$ will introduce errors on the same order as those due to spectrum broadening.

4.4. Errors caused by an evolving wind field

Violation of the quasi-steady assumption can be a large source of error in most SDD analyses (section 2.4.4). The "spin-up" of a mesocyclone is modeled on the simulator to see how a typical dynamical evolution can affect the SDD results.

Initially, the modeled mesocyclone has a radius of 5.0 km with an outer rim velocity of 12 m/s . Twenty minutes later, under a constant convergence of $1 \times 10^{-3} \text{ s}^{-1}$, the radius has decreased to 2.8 km and the rim velocity has gone up to 22 m/s (Figure 4.4A) ². The mesocyclone, first viewed at 190° and 60 km , moves eastward to 170° and 60 km during the 20 minute time interval. The radial components associated with the initial and final stages are shown in Figure 4.4B.

The wind field reconstruction (Figure 4.4C) retains the general cyclonic pattern, but wind speeds in certain areas are much too strong. In addition, the reconstructed wind field is hardly the average of the initial and final stages. The computed RMS error is about 8 m/s , which is almost as large as the actual mean flow speed. As expected, the difference wind fields show that the most significant errors occur where the initial and final stages of

²See Appendix E for details on how these numbers were obtained.

the wind field differ the most. Errors of a few m/s also exist over the remainder of the domain and tend to be oriented with the wind flow.

This example shows that temporal changes to the wind field can cause errors large enough to completely obliterate even the qualitative aspects of a wind field. As such, the time between the data sets used in an SDD analysis should be kept as short as possible.

4.5. Errors caused by combined effects

Spectrum broadening, imprecise matching (horizontal and vertical) and the non-steady aspects of a wind field can combine to give quite large errors in radial components that are used in the SDD analysis. If it is assumed that these error sources are independent, unbiased and normally distributed, then the errors add in quadrature, yielding the following relationships:

$$\sigma_r = \sqrt{(\sigma_r^2)_{\text{spectrum broadening}} + (\sigma_r^2)_{\text{position mismatch, h}} + (\sigma_r^2)_{\text{height mismatch, h}} + (\sigma_r^2)_{\text{evolution, w}}}$$

$$RMS_{err} = \sqrt{(RMS_{err}^2)_{\text{spectrum broadening}} + (RMS_{err}^2)_{\text{position mismatch, h}} + (RMS_{err}^2)_{\text{height mismatch, h}} + (RMS_{err}^2)_{\text{evolution, w}}}$$

(4.1)

The second expression can be obtained from the first since RMS errors can be shown to be linearly proportional to σ , (see (4.2) and Appendix D).

Apart from the spectrum broadening term, it cannot generally be assumed that the error sources will have Gaussian distributions. However, if fairly large wind fields are being analyzed, it may be reasonable to consider the average error over the entire wind field as having a pseudo-normal distribution. In certain regions of the analysis domain, for example, error from the evolution term may be skewed and biased, but could be compensated for in other areas by an opposite bias.

Any of the four terms in (4.1) can be significant or dominant, depending on the particulars of the SDD case. The position mismatch term, however, can be made relatively small when run-time adjustments of the storm positions are possible (section 3.3). Further, if one limits SDD analyses to cases where the storm motion is mostly radial, the height error term can be neglected. On the other hand, the spectral broadening error is always present, as is the error due to a non-steady wind field. The spectral broadening term can

be approximated from the measured spectral widths (see (2.4)), but the evolution term can only be estimated in a very qualitative manner.

The simulator was used to see how errors for a "typical" SDD case combine. The wind field used consists of a modified Rankine vortex with an average convergence of $0.5 \times 10^{-3} \text{ s}^{-1}$. For the first observation, the vortex has a radius of 5.0 km and a rim velocity of 12.0 m/s. After converging for 20 minutes, the radius has decreased to 3.7 km and the rim velocity has increased to 16.2 m/s. The radius at mid-time is 4.3 km with a rim velocity of 14.0 m/s, which characterizes the average wind field with which the SDD analysis can be compared. Spectrum broadening is modeled by adding normal errors of 2.5 m/s to the radial components. The storm position mismatch is simulated by positioning the second set of radial velocities 0.7 km to the southeast of its actual location.

Figure 4.5A shows the initial and final stages of the vortex, along with the wind field at the average time. The radial components used for the simulations and those of the average field are shown in Figure 4.5B. The reconstructed and average wind fields are significantly different (Figure 4.5C). Nevertheless, a vortex is identifiable and is qualitatively similar to the average (mid-time) vortex that a dual-Doppler would have observed. The differential fields, as expected, show even more deterioration, to the point of being almost useless (Figure 4.5D).

The above simulation was repeated many times with various degrees of position and spectral broadening errors. The individual RMS error contributions were evaluated by doing simulations with one error term at a time. Results (Table 4.1) suggest that, in some cases, errors do seem to add in quadrature (4.1). This is not true, however, when the spectral broadening error is larger than about 2.0 m/s. In fact, with spectral errors of 2.5 m/s, interference between the error sources decreases the overall error to less than that from spectral broadening alone.

CASE	Spectral noise (m/s)	Position error on second observation (km)	RMS spectrum broadening (m/s)	RMS positioning errors (m/s)	RMS rotation errors (m/s)	RMS total (measured) (m/s)	RMS total (calculated) (m/s)
1	0.5	0.7 SE	2.1	2.3	4.0	4.8	5.1
2	0.5	1.5 E	2.1	6.4	4.0	7.5	7.9
3	0.5	1.1 SSW	2.1	4.1	4.0	5.6	6.1
4	1.5	0.7 SE	6.4	2.3	4.0	6.5	7.9
5	1.5	1.5 E	6.4	6.4	4.0	8.9	9.9
6	1.5	1.1 SSW	6.4	4.1	4.0	6.7	8.6
7	2.5	0.7 SE	10.5	2.3	4.0	9.0	11.5
8	2.5	1.5 E	10.5	6.4	4.0	10.8	13.0
9	2.5	1.1 SSW	10.5	4.1	4.0	9.3	12.0

Table 4.1 Simulation results for an SDD case with combined errors.

4.6. Dependence of SDD analyses on angular separation

Using the simulator, it is possible to get an estimate of the angular separation required between two storm observations for a reasonable synthesis of the horizontal wind field. A Burgess mesocyclone is again used for the simulations, with spectral noise of 2 m/s added to the radial components. Figures 4.6A-B show the SDD reconstructions for various angular separations. As observed by Klimowski (1992) in various SDD analyses, significant deterioration in the wind field occurs for angular separations less than 20°

More general conclusions can be reached by assuming that uncertainties in the radial wind field are non-biased and normally distributed. It can be shown that the RMS difference between the initial and reconstructed wind fields is given by (Appendix D):

$$\begin{aligned}
 RMS_{error} &\equiv \sqrt{(\overline{u_0 - u})^2 + (\overline{v_0 - v})^2} \\
 &= \sqrt{\overline{du^2} + \overline{dv^2}} \cong \frac{\overline{\sigma_r} \sqrt{2}}{\sin(\beta_1 - \beta_2)} \quad (4.2)
 \end{aligned}$$

where the overbars represent an average over the wind field. This expression shows that the RMS error depends linearly on the error in the radial components, σ_r , but is

independent of the wind speed itself. In addition, the RMS error is a function of the angular separation, $(\beta_1 - \beta_2)$, and becomes very large when the angular difference is small (or close to 180°). Klimowski (1992) provides a similar analysis based on the work of Pilié (1963) and Krauss (1974).

Plots of the curves defined by (4.2) are shown in Figure 4.7 for various values of σ . Results from SDD simulations using spectral noise on a cyclonic wind field³ are superimposed onto the curves. The curves show a strong increase in RMS error for angular separations less than about 30° . With typical spectral noise, separations less than 20° introduce very large errors to the synthesized wind field.

4.7. Observations of the dependence of SDD analyses to wind orientation

As mentioned in section 2.3, the best wind magnitude estimates are obtained when the true wind is aligned along the bisector of the angle between the radars while the best wind directions are obtained when the true wind is aligned perpendicular to this bisector. Klimowski's (1992) SDD cases confirmed this spatial dependency (using results of a dual-Doppler analysis as the "true" wind field). In this study, the SDD simulator is used to demonstrate this orientation dependence in the synthesis of horizontal winds.

A uniform northeasterly wind field of 12.7 m/s with spectral errors of 1 m/s in the radial velocity is used for the simulations. Two cases are examined. First, the storm positions are chosen such that the bisector of the angle between the storm observations was aligned with the true wind (45°). This scenario is then repeated but with the bisector aligned perpendicular to the true wind (135°). The initial wind field and results of the simulations are shown in Figures 4.8A-C. The RMS errors are similar for both configurations. The difference wind fields, however, clearly show that the RMS error is largely due to direction (speed) inaccuracies when the bisector of the observations is parallel (perpendicular) to the true wind.

The effect that this orientation dependent error has on the SDD reconstruction of a Burgess mesocyclone is shown in Figure 4.9. The difference wind field is largely perpendicular to the average viewing angle from the radar.

³As (4.2) suggests, any wind field can be used to run simulations since the RMS error only depends on the noise in the wind field and the angular difference between the observations.

Since a mesocyclone consists of flow in all orientations, it can be concluded that *for SDD analyses, the difference wind field due to spectral noise is mostly perpendicular to the average viewing angle from the radar*⁴. It is noted, however, that this effect decreases as the angular separation between the observations is increased. Figures 4.10A-B show the difference wind fields for the Burgess mesocyclone using various angular separations. The difference wind field is largely perpendicular to the average viewing angle for separations of less than 30°. However, at an angular separation of 90°, the difference wind vectors are randomly oriented.

This behavior of the difference wind field also applies to dual-Doppler analyses, but is of lesser importance (than in SDD) since angular separations for dual-Doppler observations are often close to 90°. For example, flight tracks for Doppler equipped aircraft are often designed such that the storm observations are perpendicular to one another. SDD scenarios, on the other hand, almost always have angular separations less than 40°.

The orientation dependence can be formulated by expressing the component errors as a function of average viewing azimuth and angular separation. The following expressions were obtained from equations (2.2) by averaging over a wind field and denoting β_1 and β_2 in terms of the average viewing angle $\beta = 0.5(\beta_1 + \beta_2)$ and the angular separation $\Delta\beta = \beta_1 - \beta_2$:

$$\begin{aligned} \overline{|du|} &= \frac{\sigma_r}{\sin(\Delta\beta)} \sqrt{\cos^2(\beta + \Delta\beta) + \cos^2(\beta - \Delta\beta)} \\ \overline{|dv|} &= \frac{\sigma_r}{\sin(\Delta\beta)} \sqrt{\sin^2(\beta + \Delta\beta) + \sin^2(\beta - \Delta\beta)} \end{aligned} \quad (4.3)$$

The overbars represent an average over a wind field with a normal distribution of noise. The component errors for the x and y components can be normalized by dividing by the magnitude of the total error. Results from spreadsheet computations (Figure 4.10C) show that the component errors vary such that the resultant error vector *tends* to be perpendicular to the average viewing angle. The orthogonality property is perfect when the angular separation is 0° but gradually decreases as the angular separation increases.

⁴Although Doviak (1976) gives a related treatment, a search of the SDD and dual-Doppler literature reveals no such generalization.

When the angular separation is equal to 90°, the error components have equal weight. Simulations on a Burgess mesocyclone, not shown in this thesis, confirm (4.3).

It is reasonable to expect that the largest errors in the wind field synthesis will be in the components perpendicular to the average viewing angle because this is the component which the Doppler radar does not measure. For the same reason, the orthogonality of the error field decreases when larger angular separations are used and vanishes when the radar observations are perpendicular to one another.

4.8. Observations of a speed bias due to errors in radial velocities

After doing many SDD simulations, it was noted that spectral uncertainties in radial velocities cause a reconstructed wind field to be stronger than the initial wind field from which the radial components are generated. We can define the speed bias ratio (*SBR*) for a given wind vector as the ratio of the reconstructed and initial wind speeds:

$$SBR \equiv \sqrt{[u^2 + v^2] / [u_0^2 + v_0^2]} \quad (4.4)$$

where u, v and u_0, v_0 represent the reconstructed and initial wind fields. Substituting $u = u_0 + du$ and $v = v_0 + dv$ into (4.4) and averaging over unbiased Gaussian distributions of du and dv , it is possible to derive an expression for the average *SBR* (Appendix D):

$$\overline{SBR} \equiv \sqrt{1 + 2 \left(\frac{\overline{\sigma_r}}{\sqrt{u_0^2 + v_0^2}} \right)^2 \frac{1}{\sin^2(\beta_1 - \beta_2)}} \quad (4.5)$$

This relation shows that the average speed bias is related to the error ratio ⁵, and to the angular separation between the observations.

Using a uniform speed wind field, 24 SDD simulations were done with error ratios of 0.5, 0.10, 0.34 and 0.51. Figure 4.11 shows these simulation results, along with predicted curves for the corresponding error ratios. The excellent agreement between the calculated and simulated results confirms the validity of (4.5).

⁵Defined here as the ratio between the mean uncertainty in the radial velocity and the mean magnitude of the "true" horizontal wind

There is no reason to suppose that a speed bias does not also exist in actual dual-Doppler analyses. However, uncertainties in the mean radial velocities with actual dual-Doppler systems are smaller than with SDD. In some instances, interpolation schemes done on full volume dual-Doppler radar scans can reduce uncertainties in the velocity fields to less than 1 m/s (Doviak 1978). This relatively small error, combined with rather large angular separations (typically 40-90°) implies that the speed bias on real dual-Doppler cases is usually small.

As mentioned in section 4.5, incorrect position matching and a non-steady wind field can introduce significant errors to the radial wind field. It can not be assumed that these errors will be normally distributed, so their effect on (4.5) is unknown. Nevertheless, the results of simulations involving incorrect positioning and non-steady wind fields usually show a tendency to overestimate the overall wind flow. This suggests that, for a typical SDD case, the matching and non-steady errors averaged over a fairly large analysis domain tend to have a Gaussian distribution.

Addition in quadrature of representative values for the various error sources gives an effective spectral noise in the radial components of 3-6 m/s. Combined with the usually small angular separation used in SDD cases, this potentially large error in the radial components may lead to quite significant speed biases. For example, with an uncertainty of 3 m/s on a 10 m/s wind flow and an angular separation of 20°, the average flow will be overestimated by 60%. Figure 4.11 suggests that, *wind speeds in SDD analyses can often be overestimated by 10 to 80%*⁶. Klimowski (1992) reported such differences (10-70%) when comparing an SDD case to a dual-Doppler analysis.

In practice, (4.5) can be used to "reduce" wind speeds on a SDD analysis. An estimate of the unbiased wind field magnitudes can be computed using average values for $\sqrt{u^2 + v^2}$, $\beta_1 - \beta_2$ and σ_r . Rewriting (4.5) to remove the right-hand-side dependency on $\sqrt{u_0^2 + v_0^2}$ leads to the following expression (Appendix D):

$$\overline{SBR} \cong \sqrt{1 + \frac{2\overline{\sigma_r^2}}{\left(\sqrt{u^2 + v^2}\right)^2 \sin^2(\overline{\beta_1 - \beta_2}) - 2\overline{\sigma_r^2}}} \quad (4.6)$$

⁶A search of the SDD and dual-Doppler literature did not reveal the hypothesis and formulation of such a bias.

where the overbars represent the mean over a given wind field. With (4.6) it is possible to calculate the average unbiased wind speed based on the mean reconstructed wind speed, angular separation and uncertainty in the radial components.

Several simulations were done on a Burgess mesocyclone to see to what degree such a bias correction could improve the final wind field. The results of these simulations (Table 4.2) suggest that a significant reduction in RMS errors is possible when the radial wind field spectral noise is relatively large and/or when angular separations for the SDD analysis are small.

CASE	Actual $\sqrt{u_0^2 + v_0^2}$ (m/s)	σ_r (m/s)	$\beta_1 - \beta_2$ (deg)	$\sqrt{u_0^2 + v_0^2}$ (m/s)	Reduced $\sqrt{u_0^2 + v_0^2}$ (m/s)	RMS error (m/s)	Reduced RMS error (m/s)	\overline{SBR}
1	9.8	1.0	10	12.8	9.9	8.3	6.8	1.3
2	9.8	3.0	10	26.1	9.2	24.3	10.7	2.8
3	9.8	1.0	20	10.7	9.9	4.2	3.9	1.1
4	9.8	3.0	20	15.9	10.0	12.5	8.6	1.6
5	9.8	1.0	30	10.2	9.8	2.8	2.8	1.04
6	9.8	3.0	30	13.1	10.0	8.8	7.2	1.3

Table 4.2 Simulator results of bias reduction on a Burgess mesocyclone 80 km south of the radar.

It is important to note, however, that although this bias reduction may lower RMS errors, a particular vector may actually deviate more from the real wind after the reduction than it did initially.

4.9. Concluding Remarks

Simulations under typical SDD conditions have shown that spectral broadening of radial velocities, storm positioning errors and the non-steadiness of a wind field can lead to important errors in a reconstructed wind field. Positioning errors can usually be minimized, which leaves spectral broadening and the evolution effects as the main contributors to error. Results of various simulations suggest that SDD can give qualitative estimates of mesoscale horizontal wind fields provided that angular separations between observations are larger than 20° and that the features are quasi-steady.

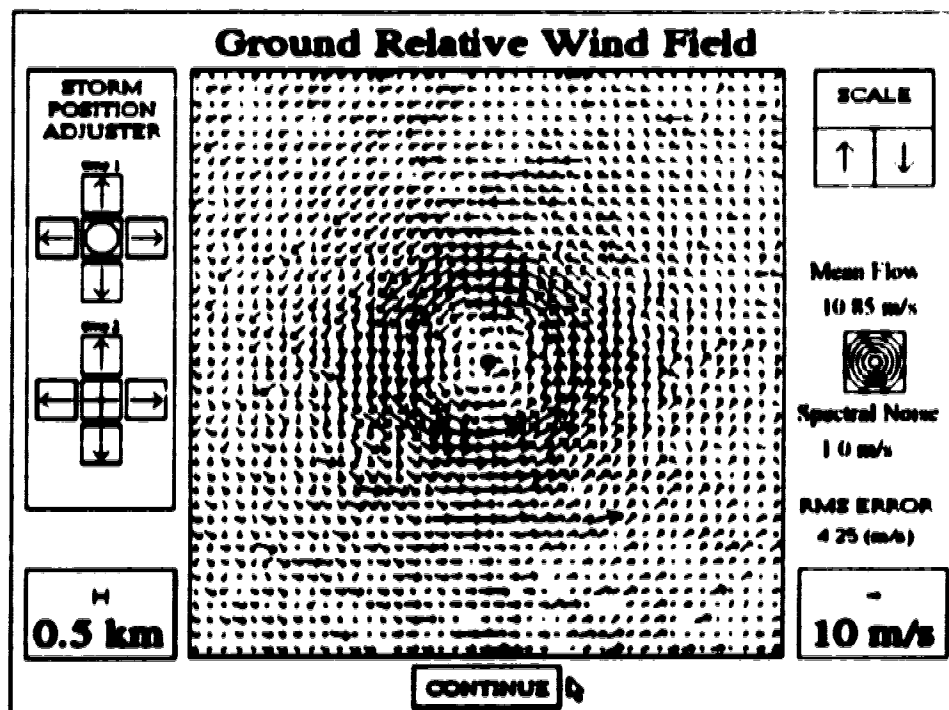
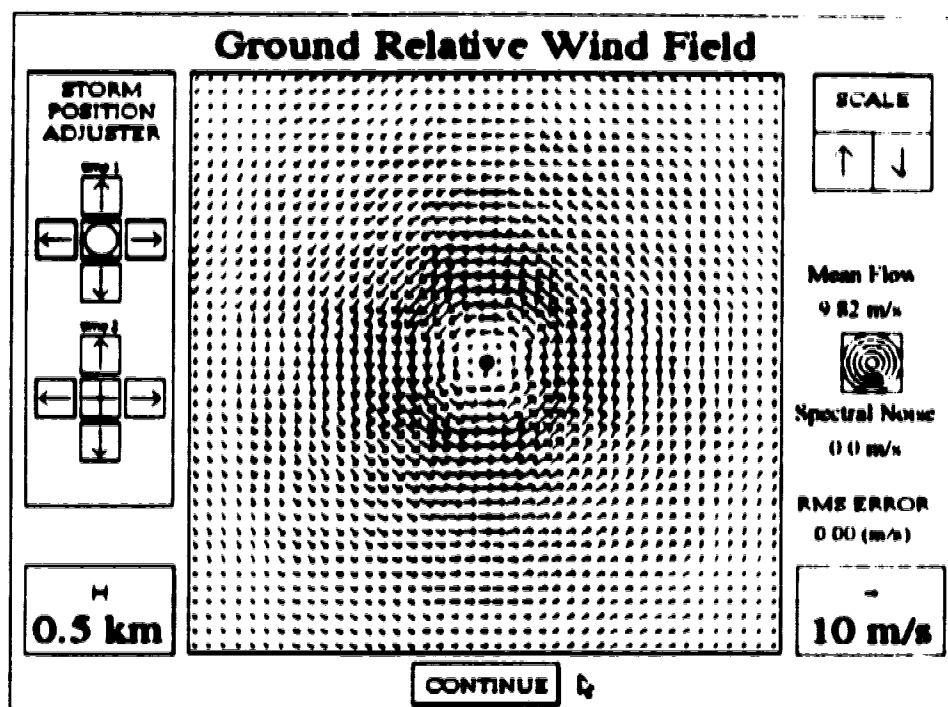


Figure 4.1A Effect of spectral noise on SDD synthesis. The initial wind field is shown on the top panel. The lower panel shows the wind field reconstruction and RMS error for an uncertainty of 1 m/s. Angular separations of 20° are used with the mesocyclone at a range of 60 km.

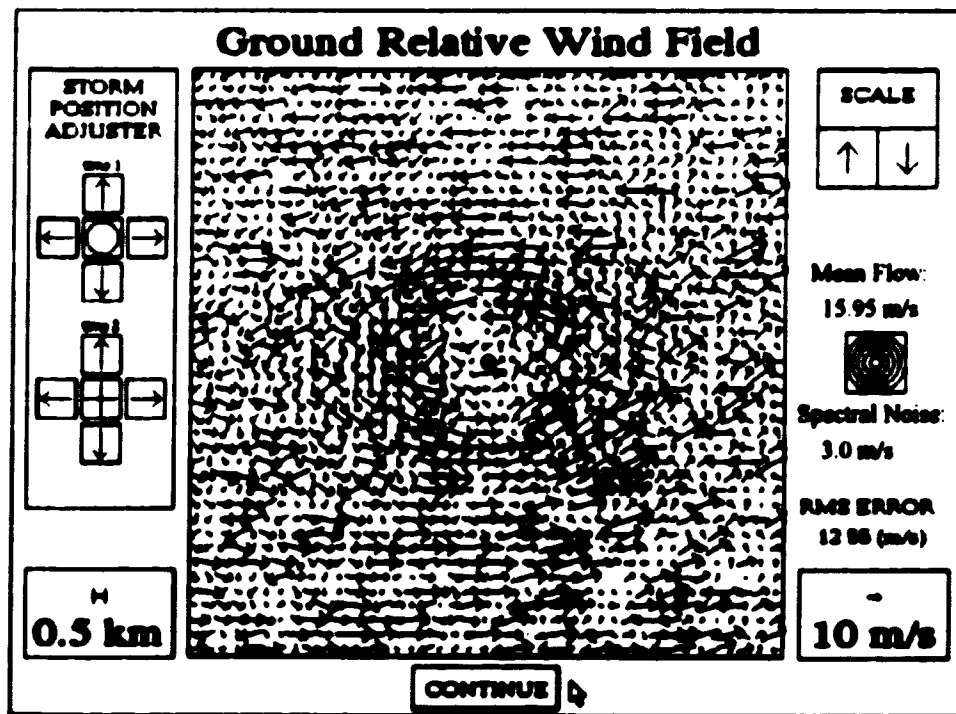
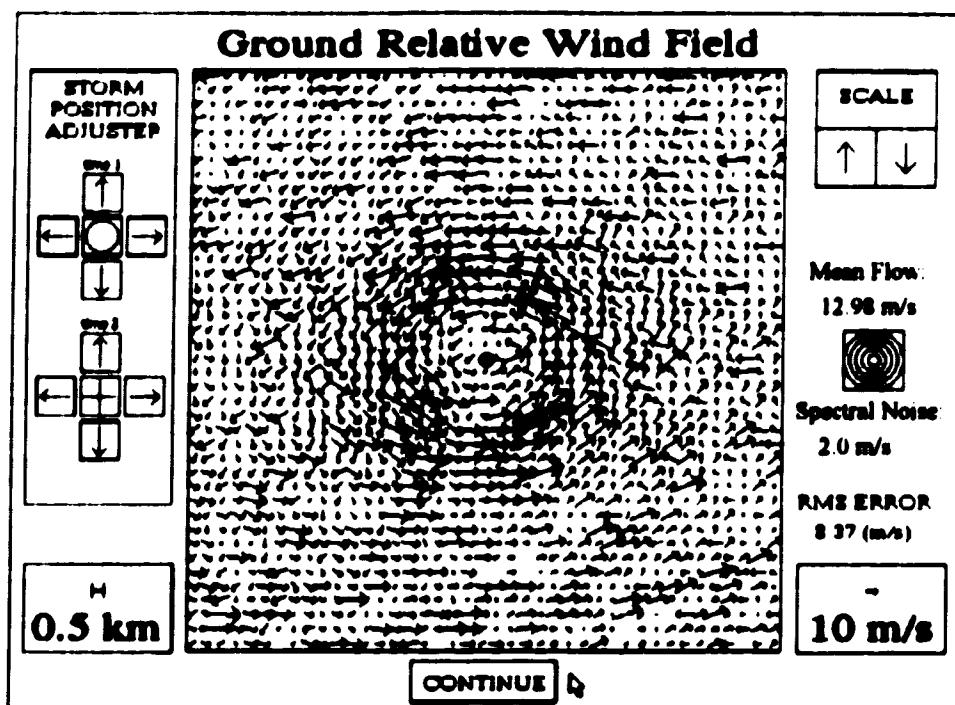


Figure 4.1B Same as in Figure 4.1A but for uncertainties of 2 and 3 m/s.

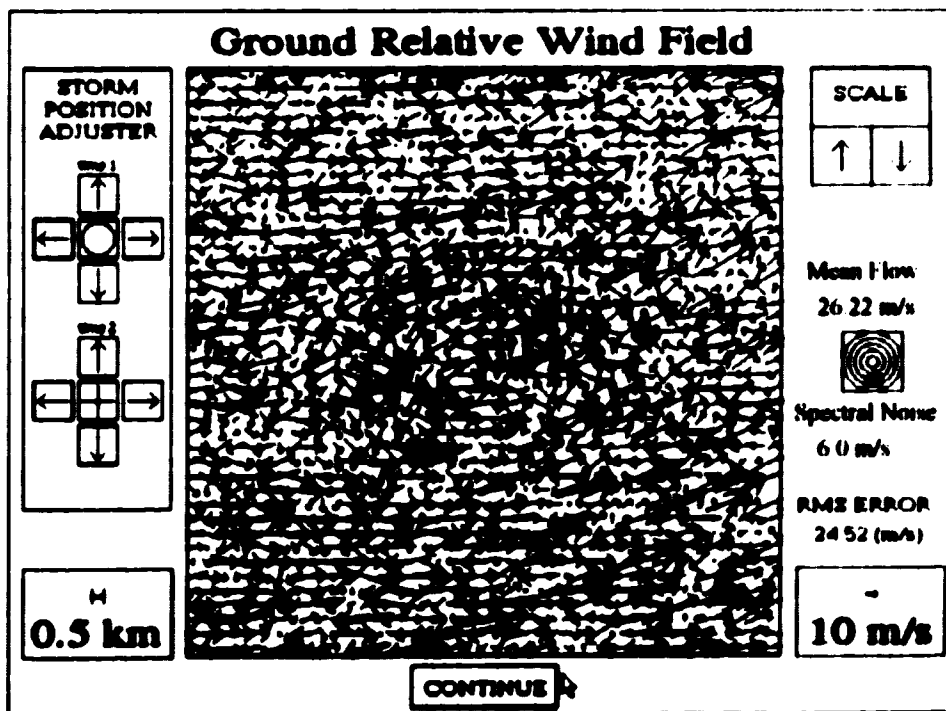
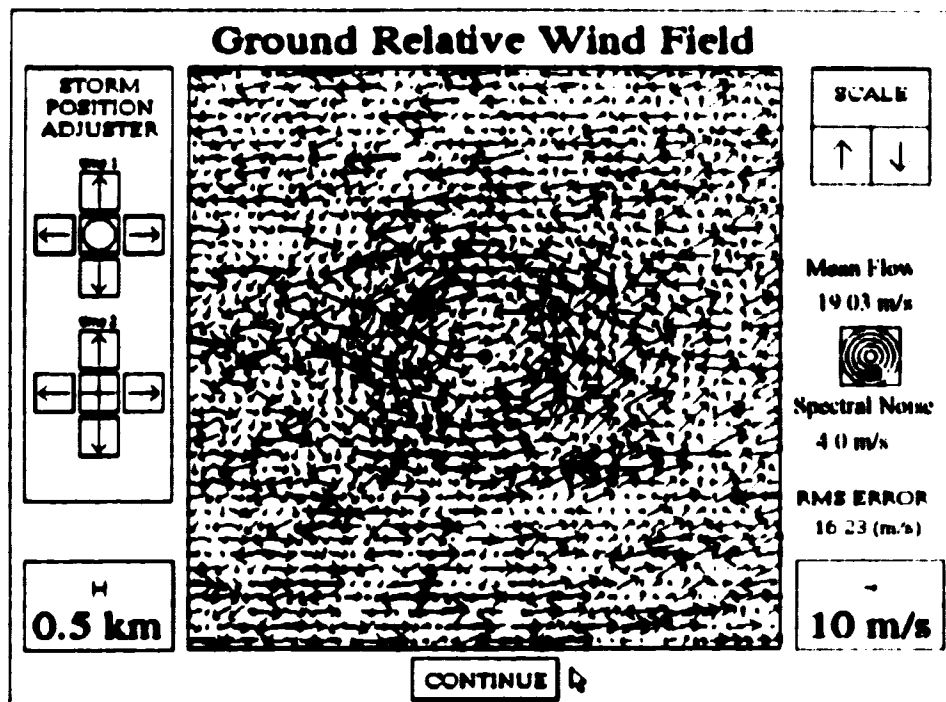


Figure 4.1C Same as in Figure 4.1A but for uncertainties of 4 and 6 m/s.

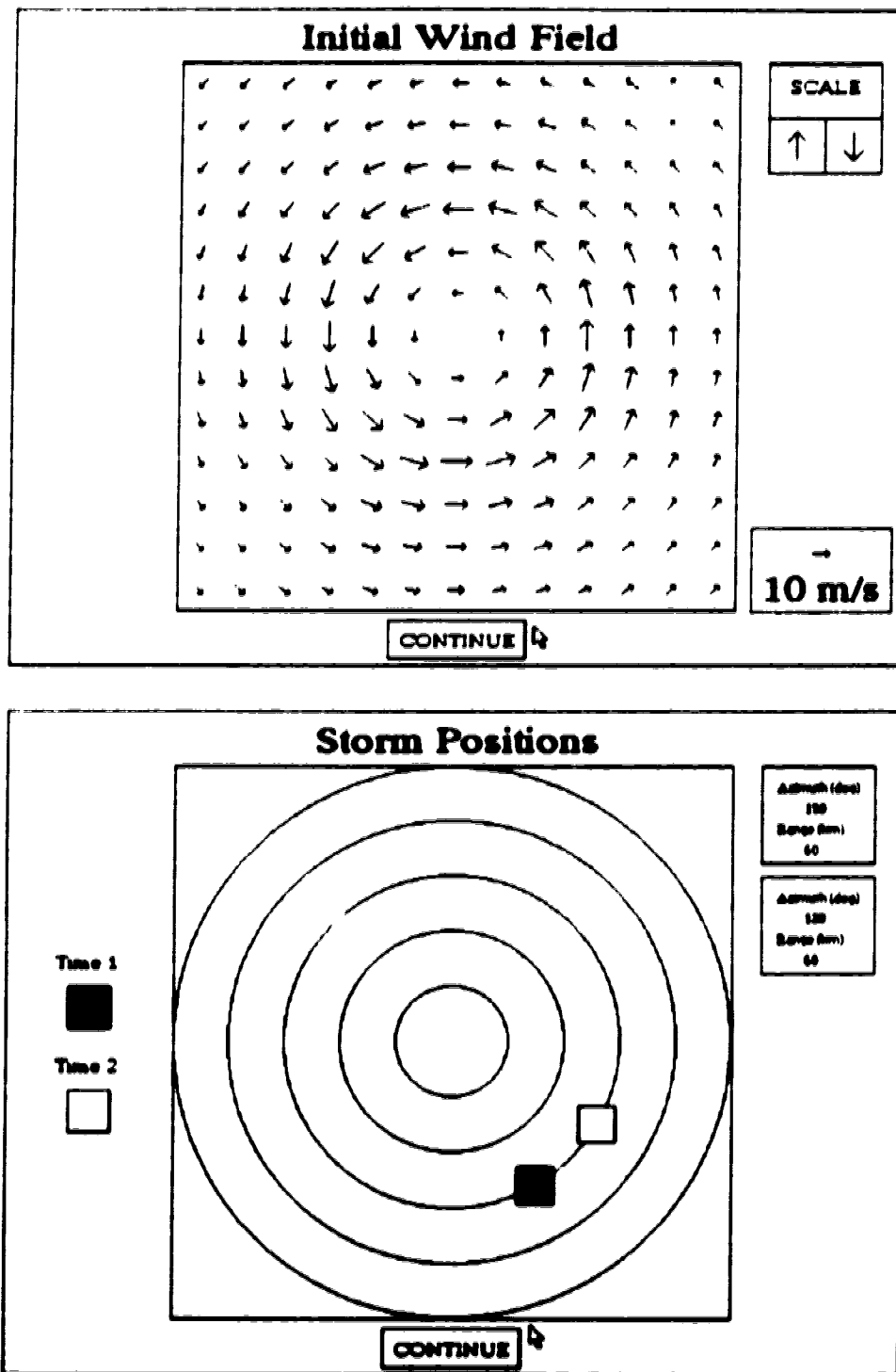


Figure 4.2A Initial wind field and SDD layout used for showing the effect of incorrect horizontal position matching of a storm.

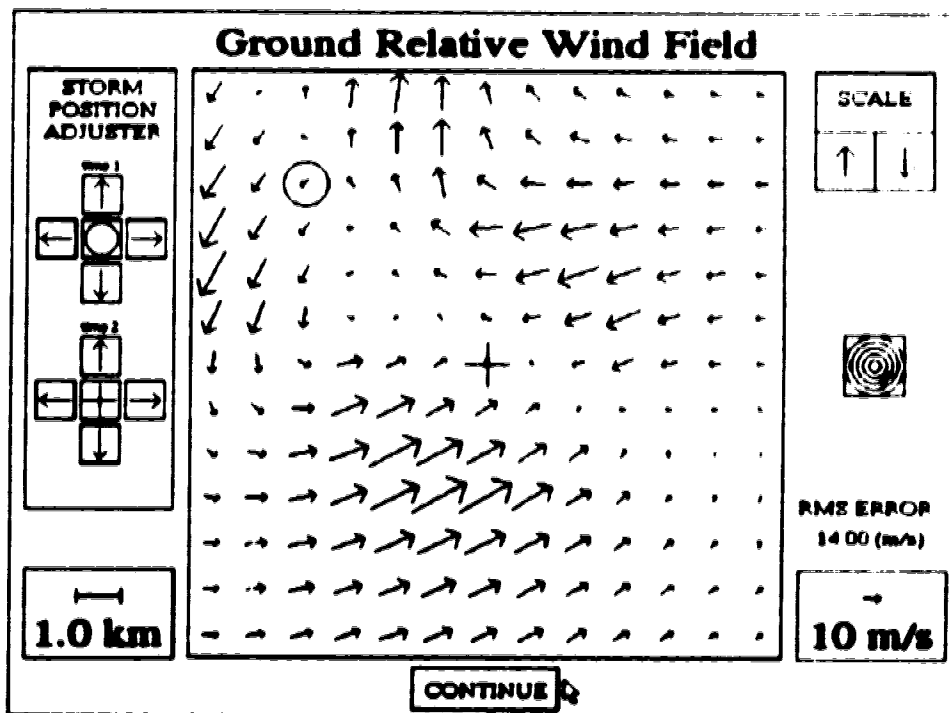
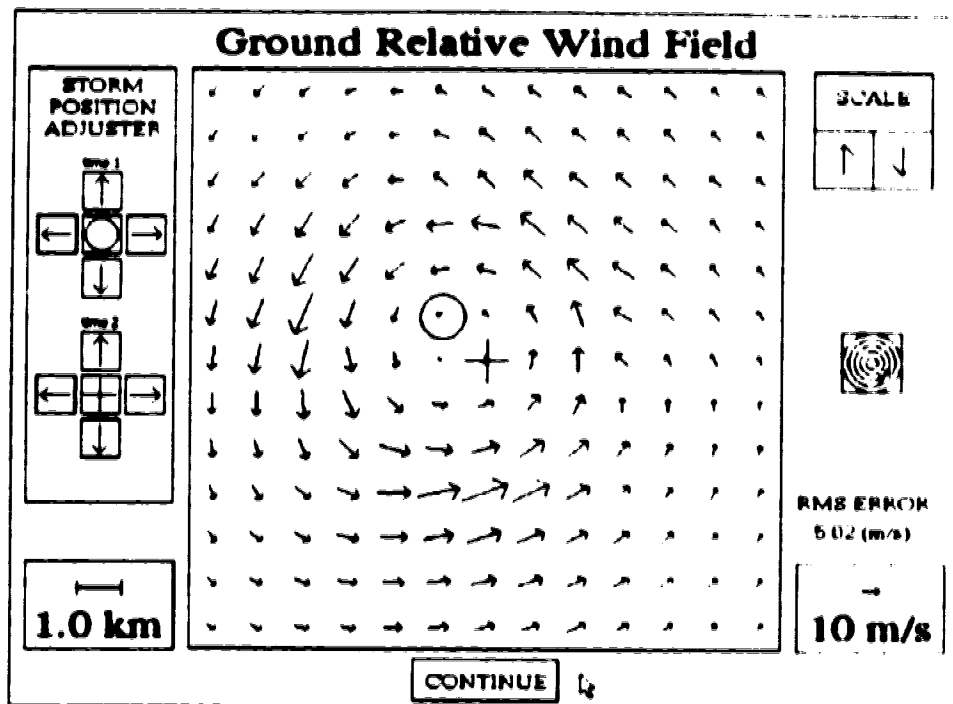


Figure 4.2B Changes in SDD synthesized wind field due to incorrect horizontal storm position matching. The circle and cross indicate the relative offsets of the radial wind fields for the first and second observations (respectively).

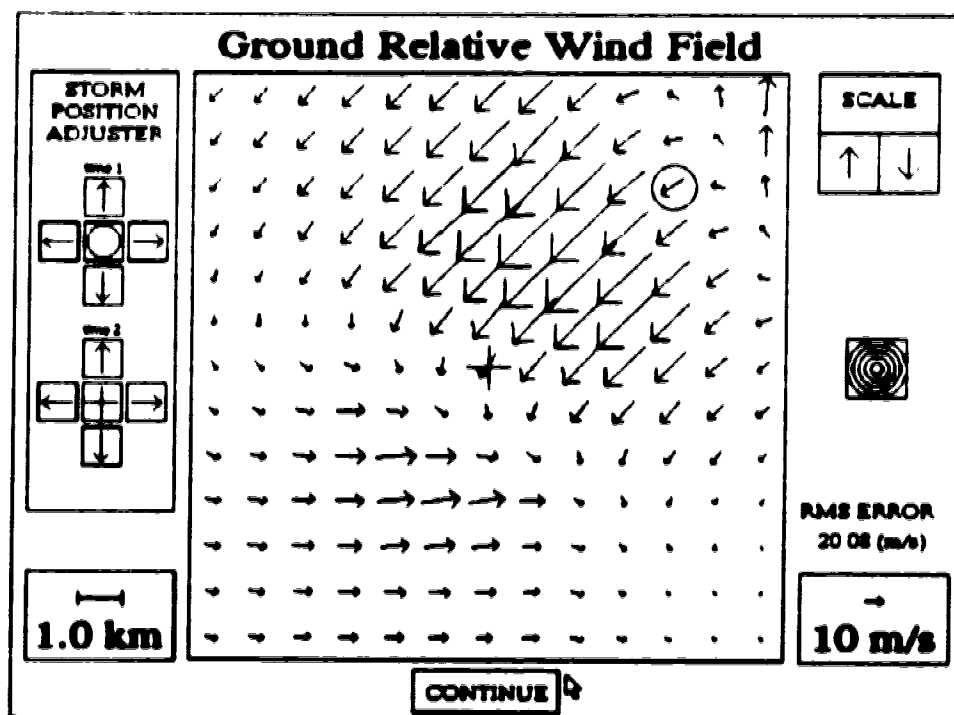
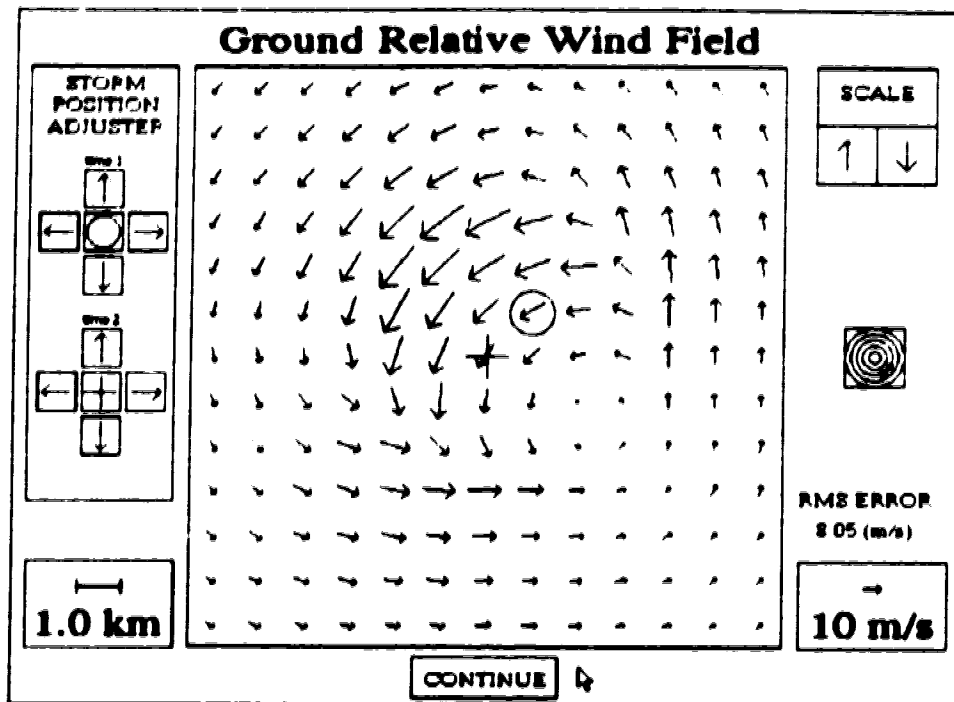


Figure 4.2C Same as in Figure 4.2B but for different offsets.

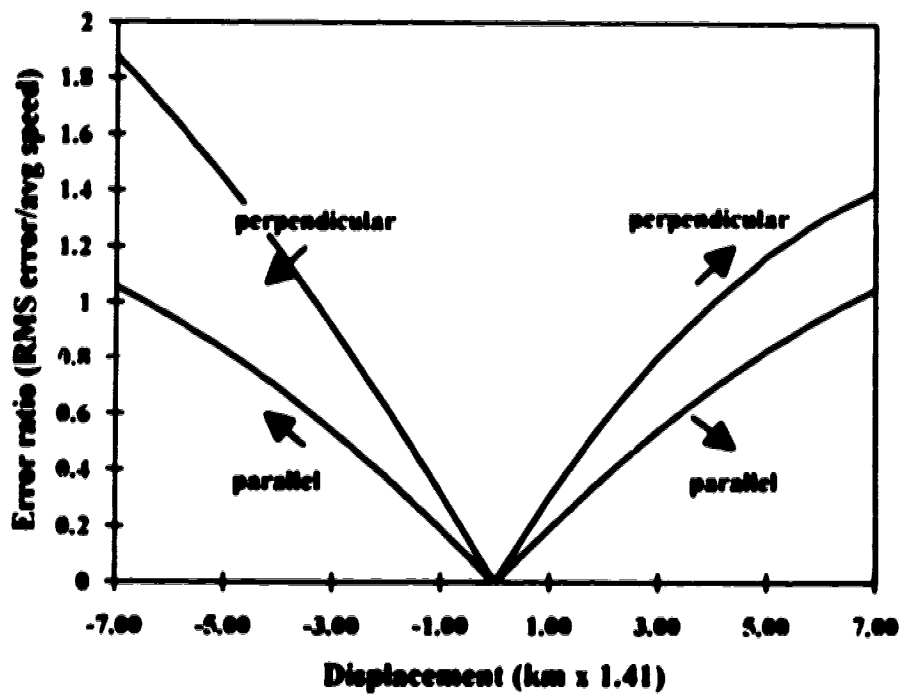
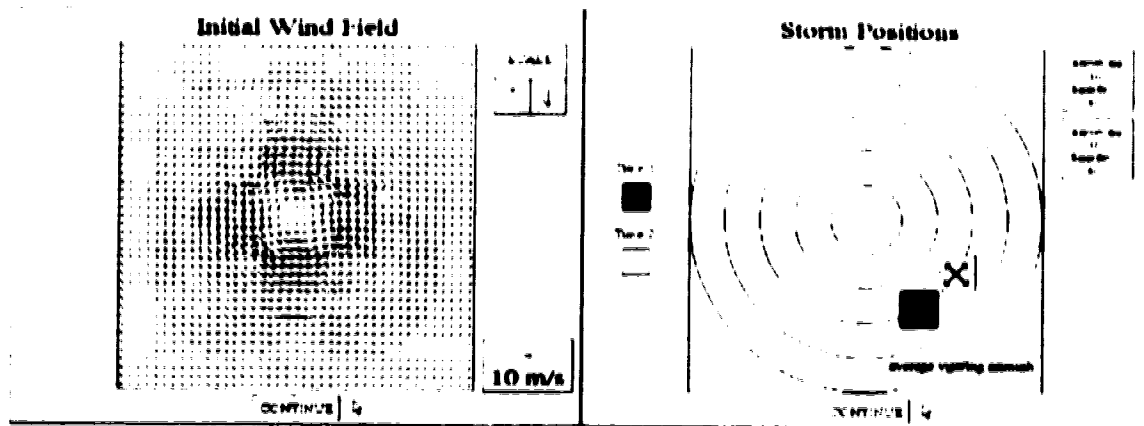


Figure 4.3 Sensitivity of SDD mesocyclone analysis to storm position matching errors. The positions used for the simulation are shown on the top panel. The lower panel shows the error ratios for adjustments to the second observation parallel and perpendicular to the viewing angle from the radar.

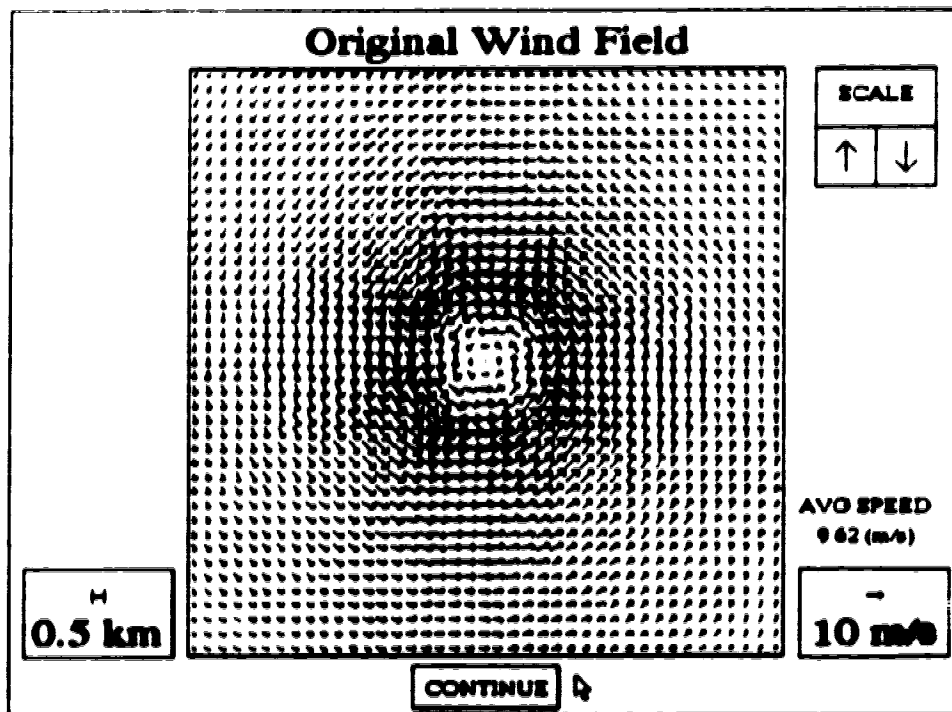
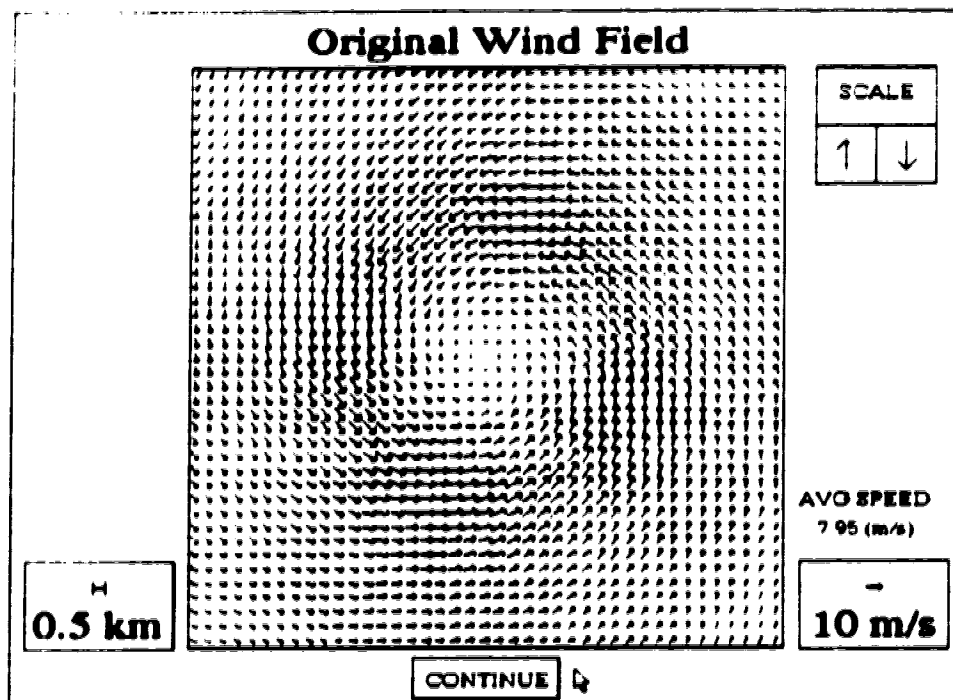


Figure 4.4A Storm relative wind fields used to simulate the effects of temporal changes on an SDD analysis. Top (bottom) panel shows a mesocyclone with a radius of 5.0 (2.8) km and an outer rim velocity of 12 (22) m s. The convergence for both mesocyclones is about $1 \times 10^{-3} \text{ s}^{-1}$.

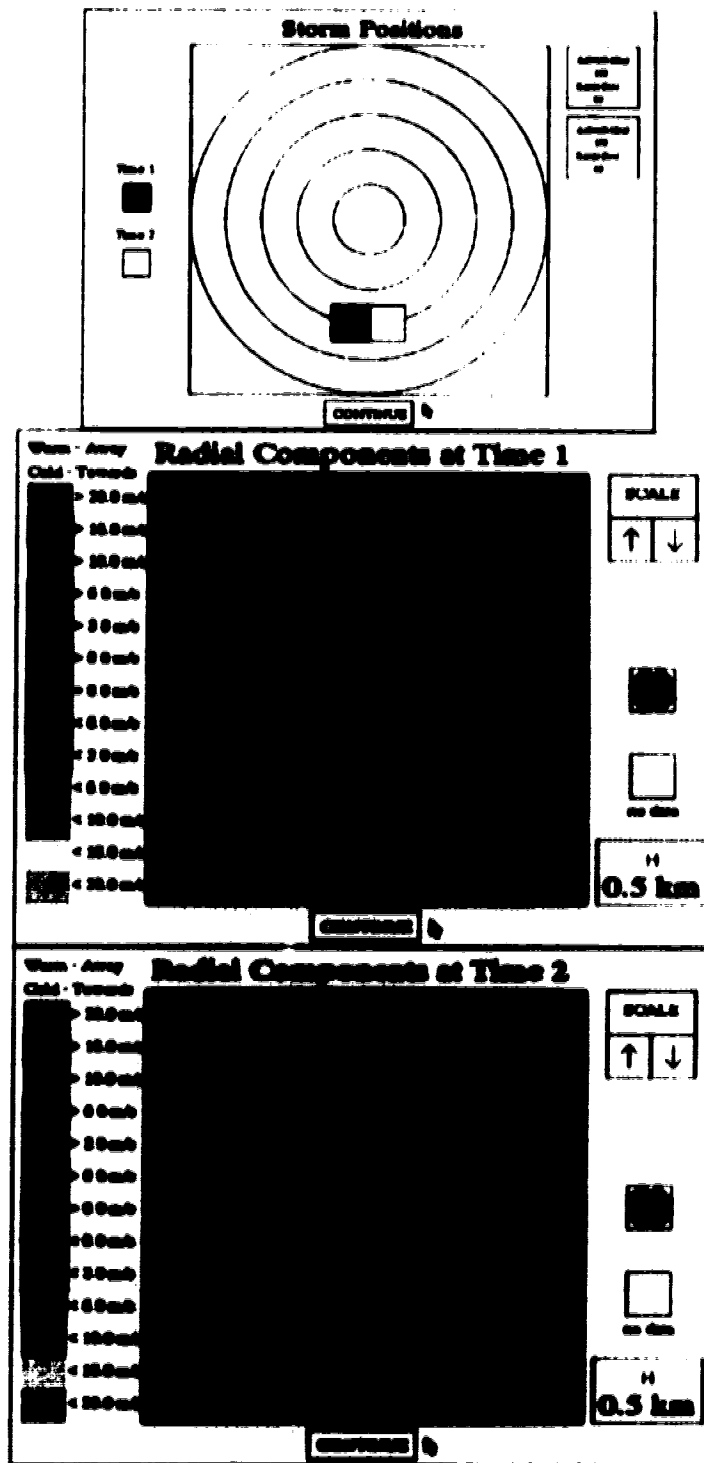


Figure 4.4B Storm relative radial component wind fields for an evolving mesocyclone as generated from wind fields in Figure 4.4A. The observing positions are shown at the top. The clockwise shift of the velocity couplet with respect to the viewing angle is a result of the convergence.

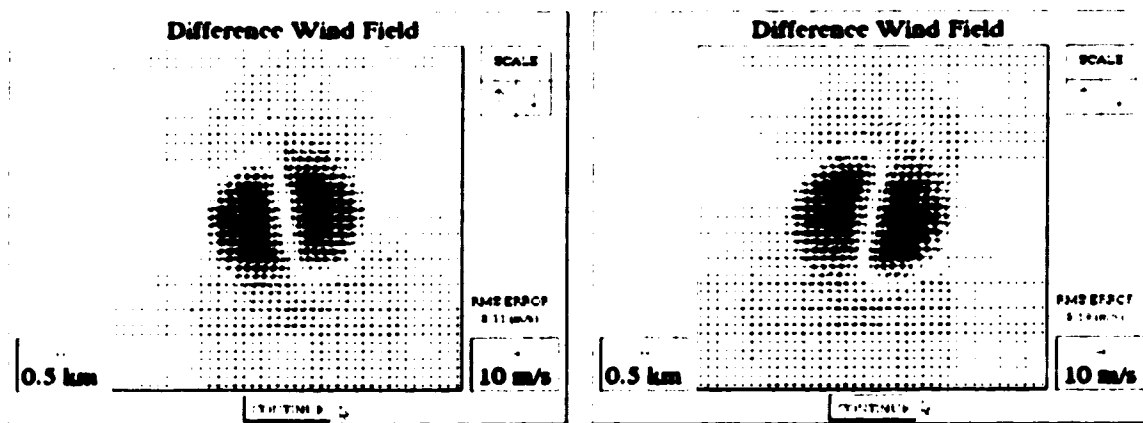
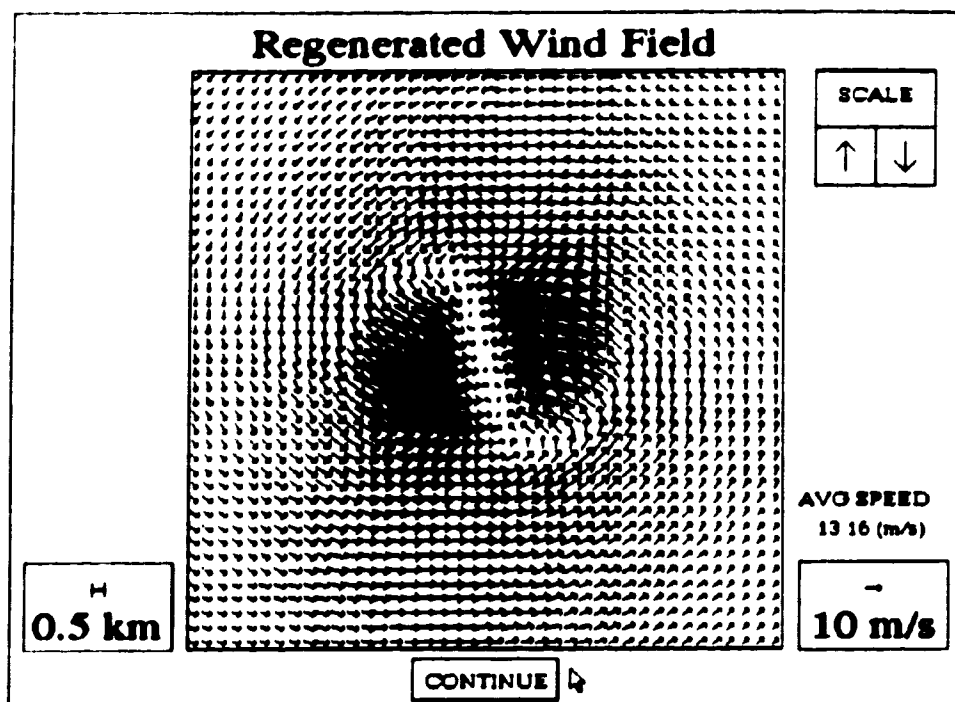


Figure 4.4C Storm relative SDD regenerated wind field for evolving mesocyclone (see Figures 4.4B). The difference between the reconstruction and original wind fields (Figure 4.4A) are shown on the bottom panels.

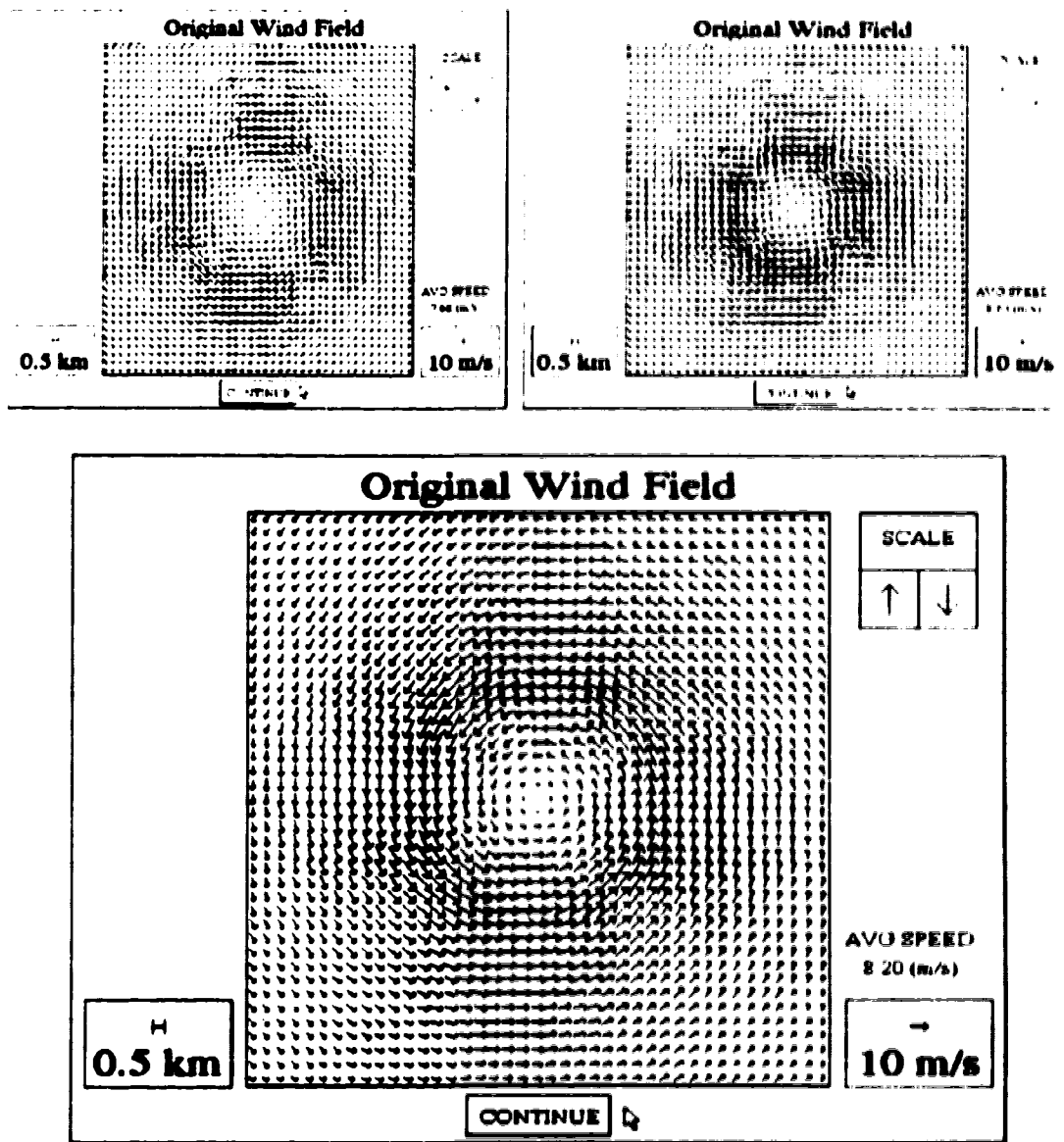


Figure 4.5A Initial (upper left) and final (upper right) stages of evolving mesocyclone used in combined error simulation. The wind field at mid-time is shown on the lower panel.

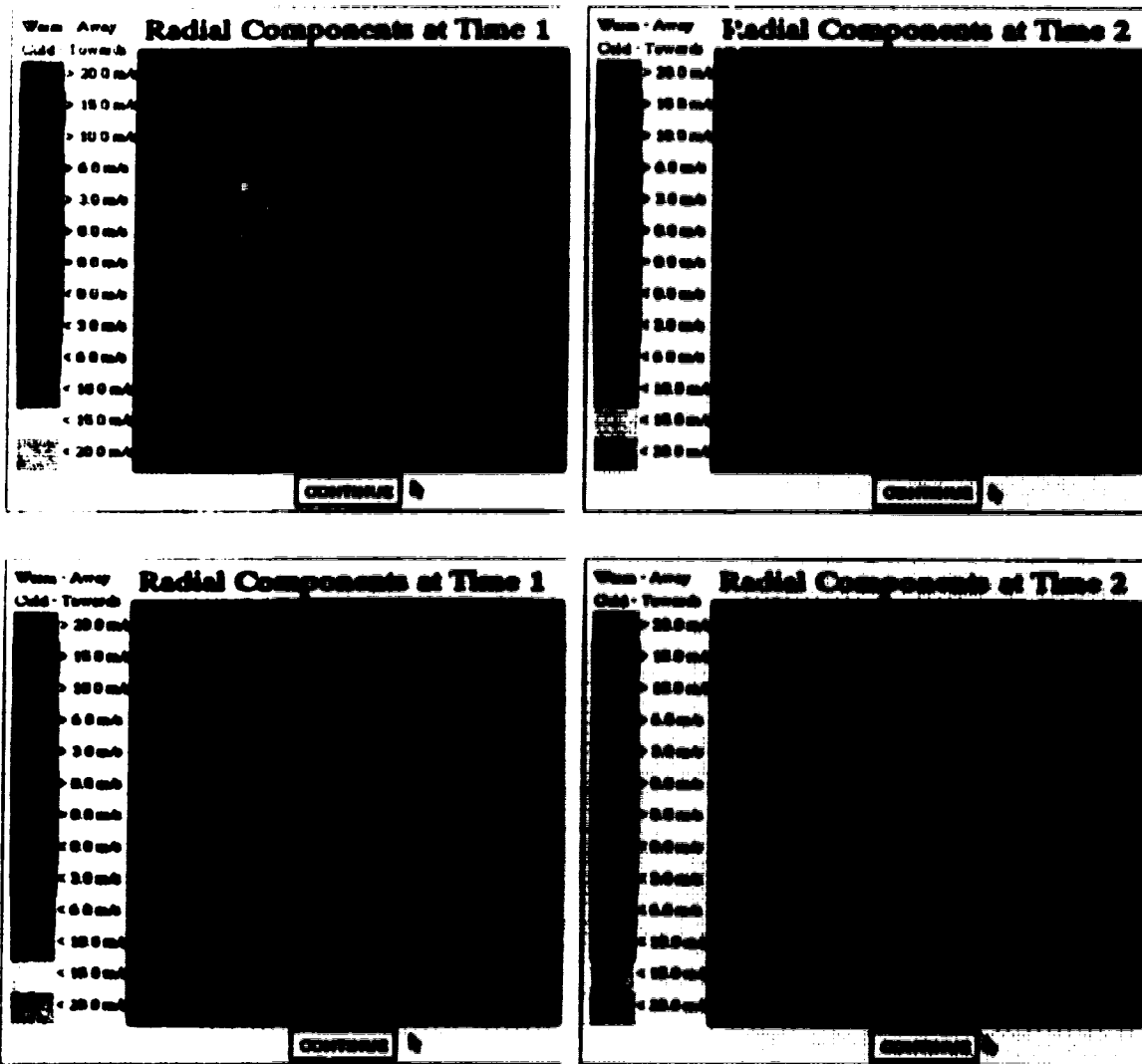
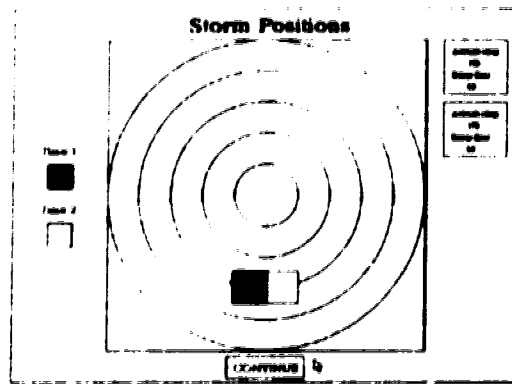


Figure 4.5B Radial component wind fields used in combined error simulation for the evolving (center) and the "average" (bottom) mesocyclones. The storm positions used for the simulation are shown on the top panel.

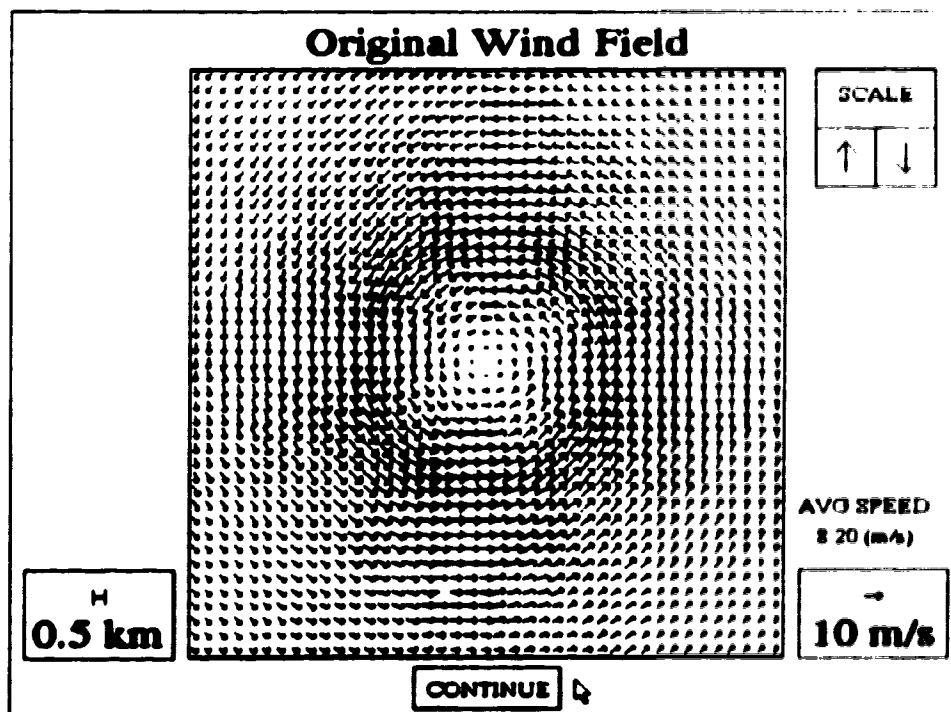
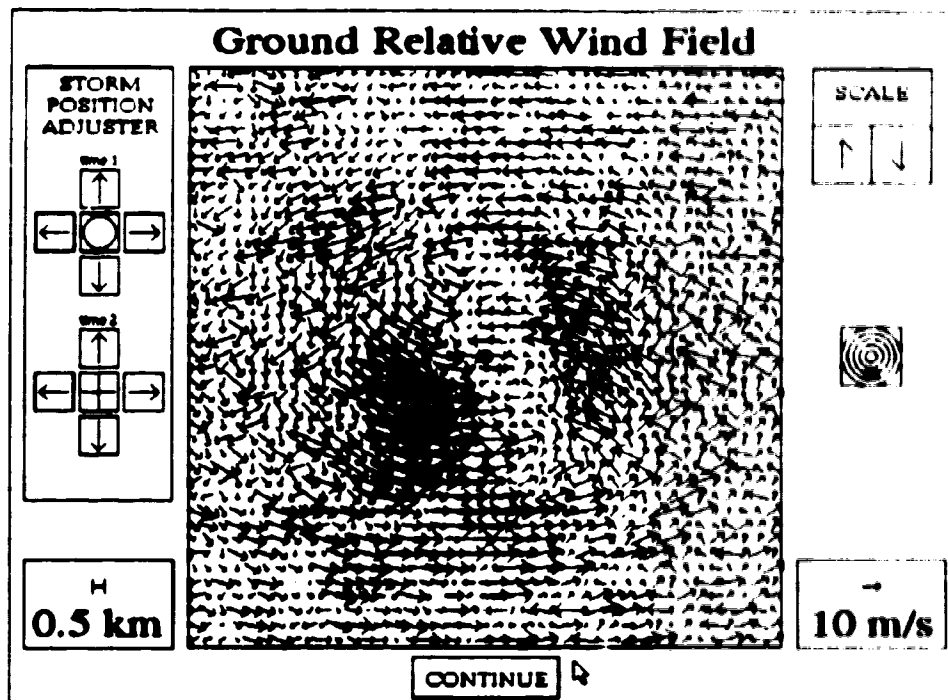


Figure 4.5C Reconstructed (top) and original (bottom) wind fields for the combined error simulation. The mesocyclone is converging, the radial wind fields have spectral noise of 2.5 m/s and the horizontal positions are mismatched by 0.7 km.

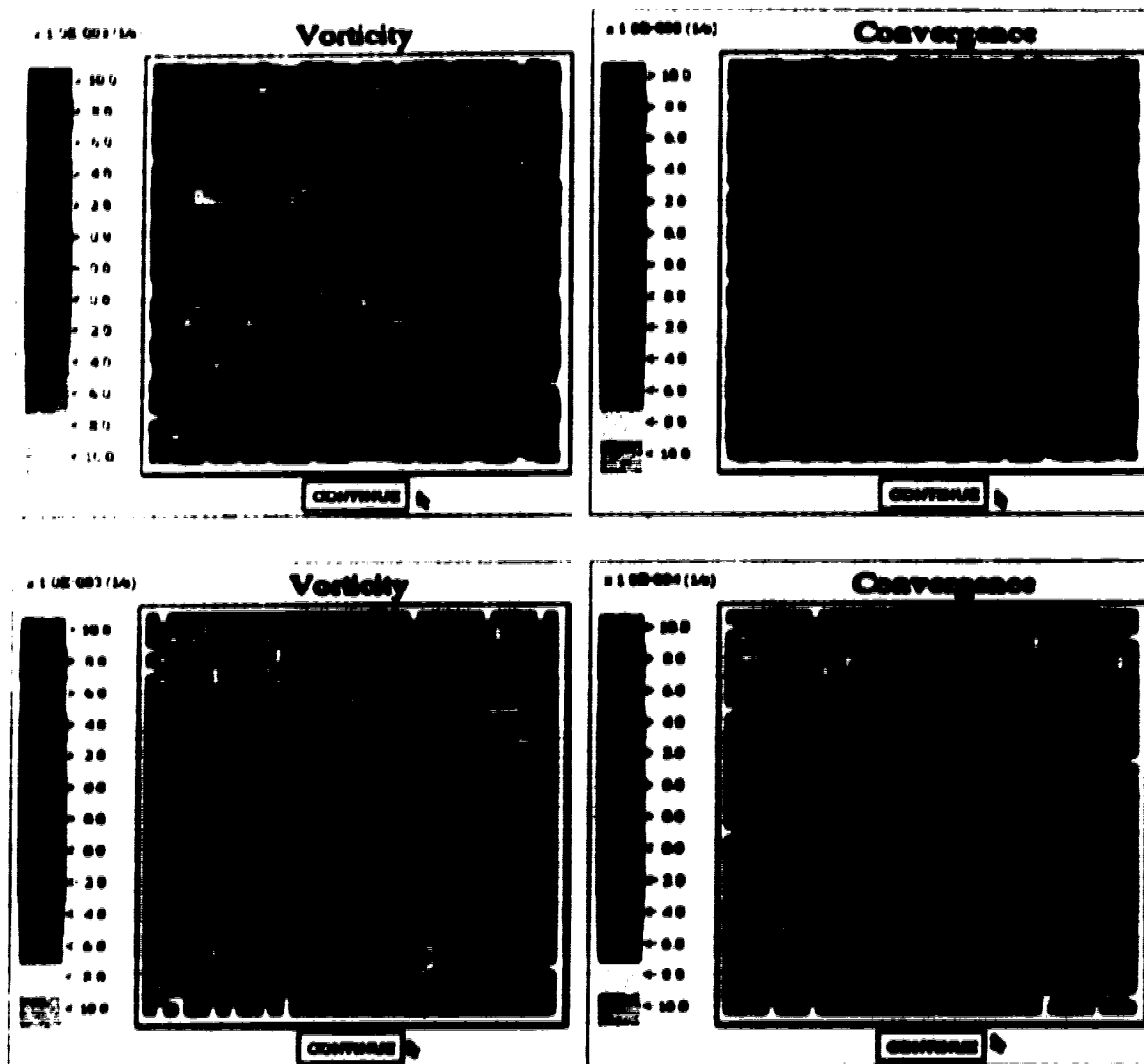


Figure 4.5D Reconstructed (top) and original (bottom) vorticity and divergence fields for the combined error simulation. The mesocyclone is converging, the radial wind fields have spectral noise of 2.5 m/s and the horizontal positions are mismatched by 0.7 km.

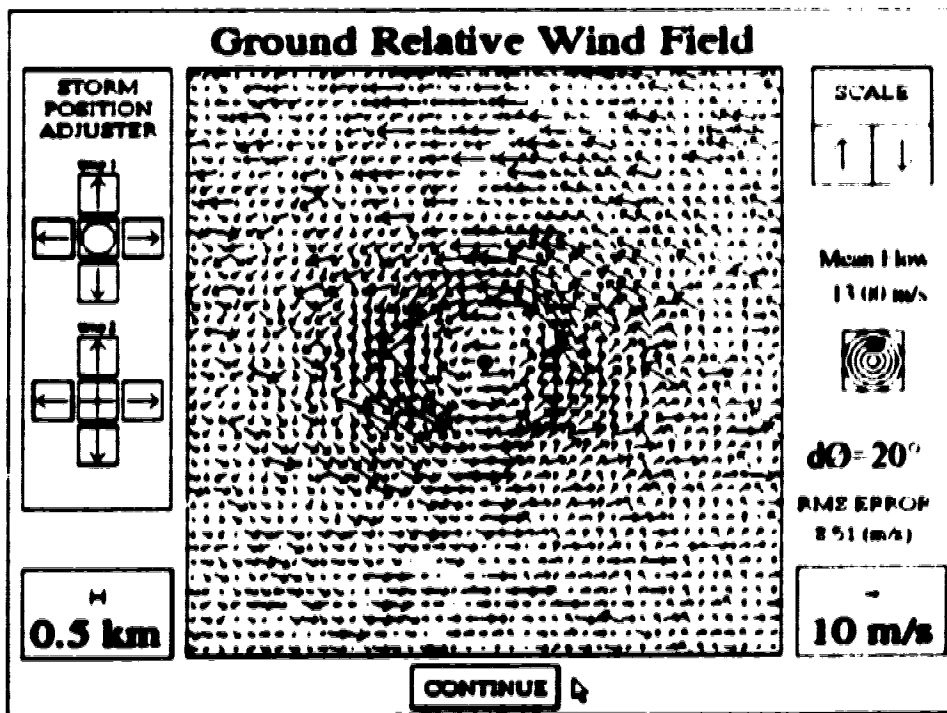
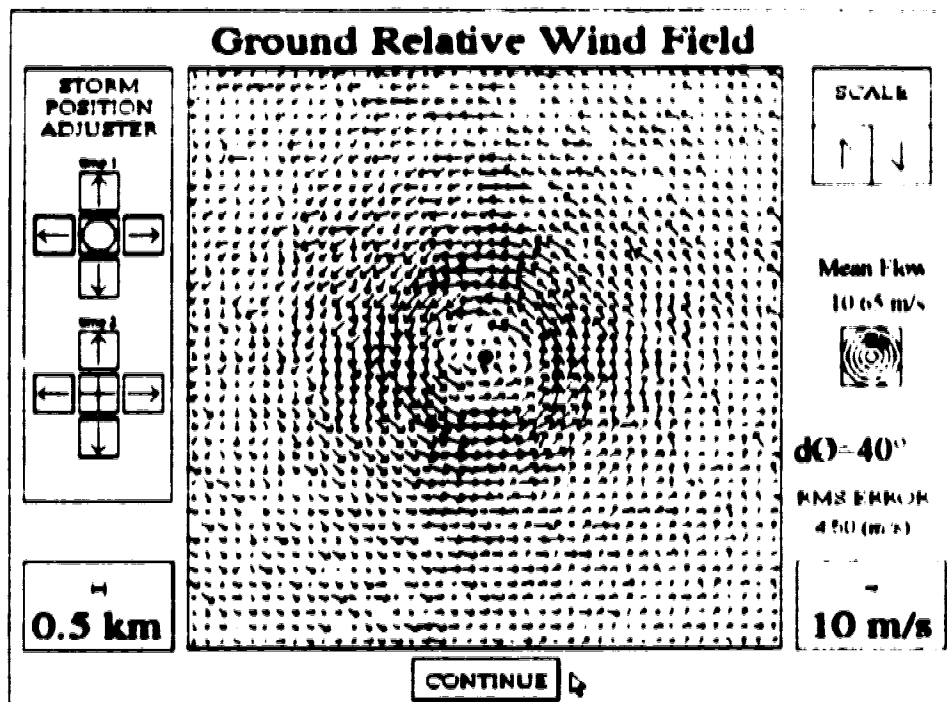


Figure 4.6A SDD wind field synthesis dependence on angular separation. Reconstructed wind fields and RMS errors are shown for angular separations of 40 and 20°. Spectral noise is constant at 2 m/s and the mesocyclone is modeled to be at 60 km from the radar.

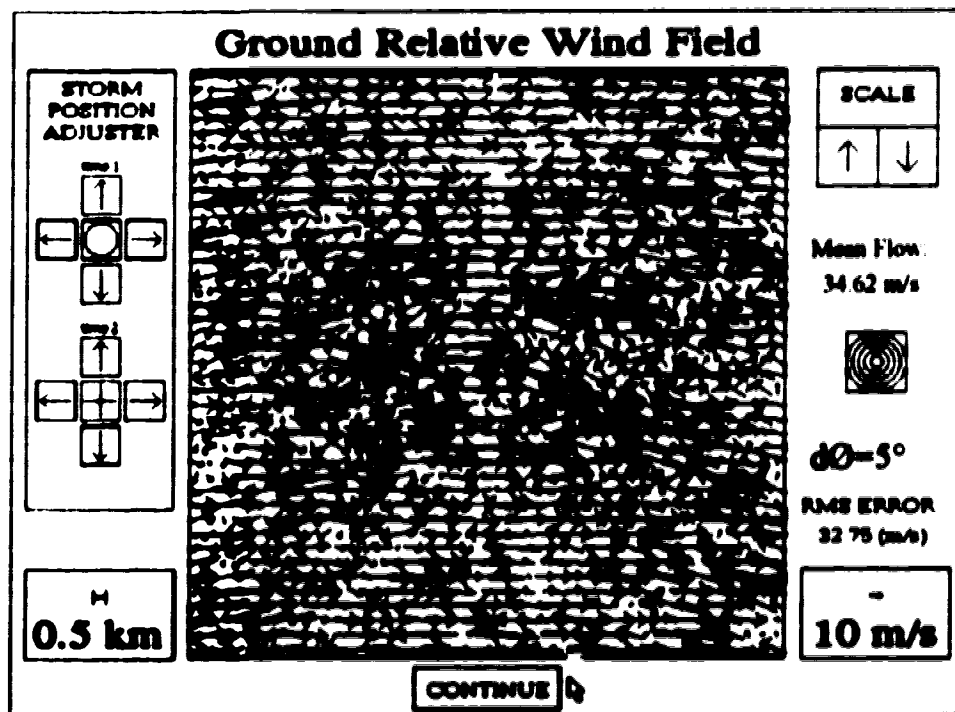
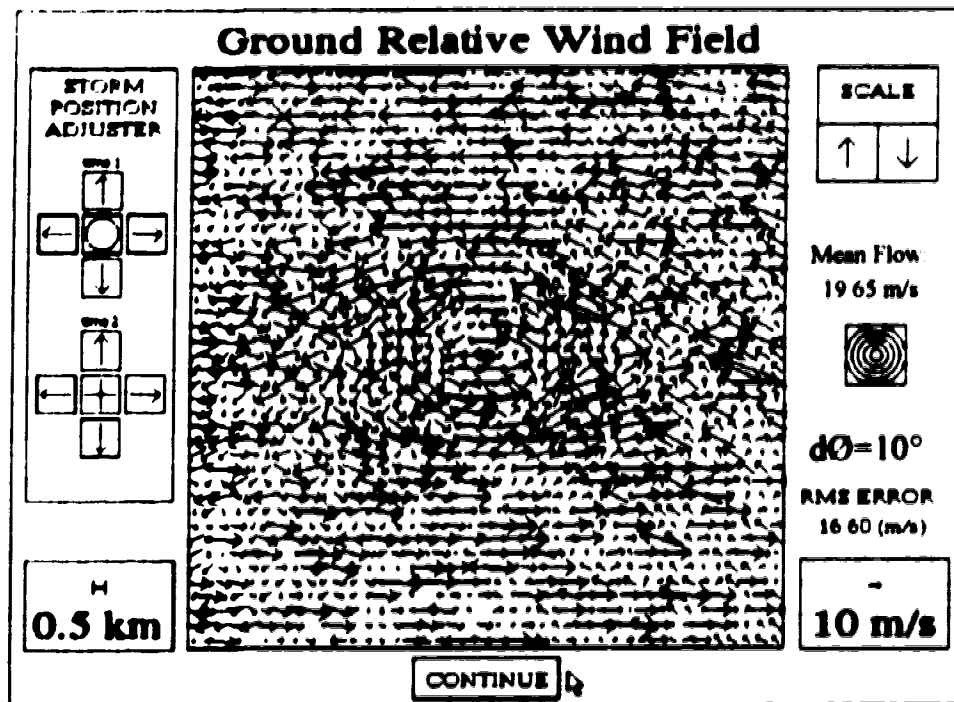


Figure 4.6B Same as in 4.6A but for 10 and 5°.

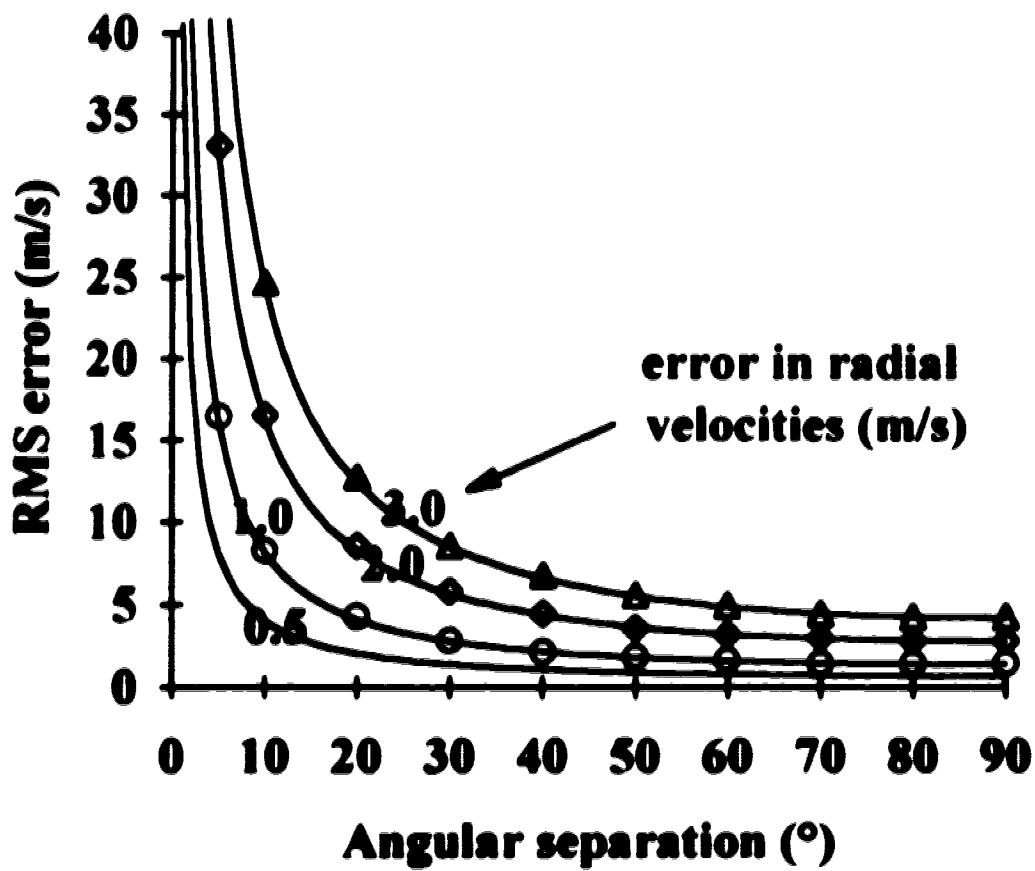


Figure 4.7 *RMS errors for SDD reconstruction as a function of angular separation between observations. Curves are plotted for spectral noise of 0.5 to 3 m s. Results from simulations are indicated with the various symbols.*

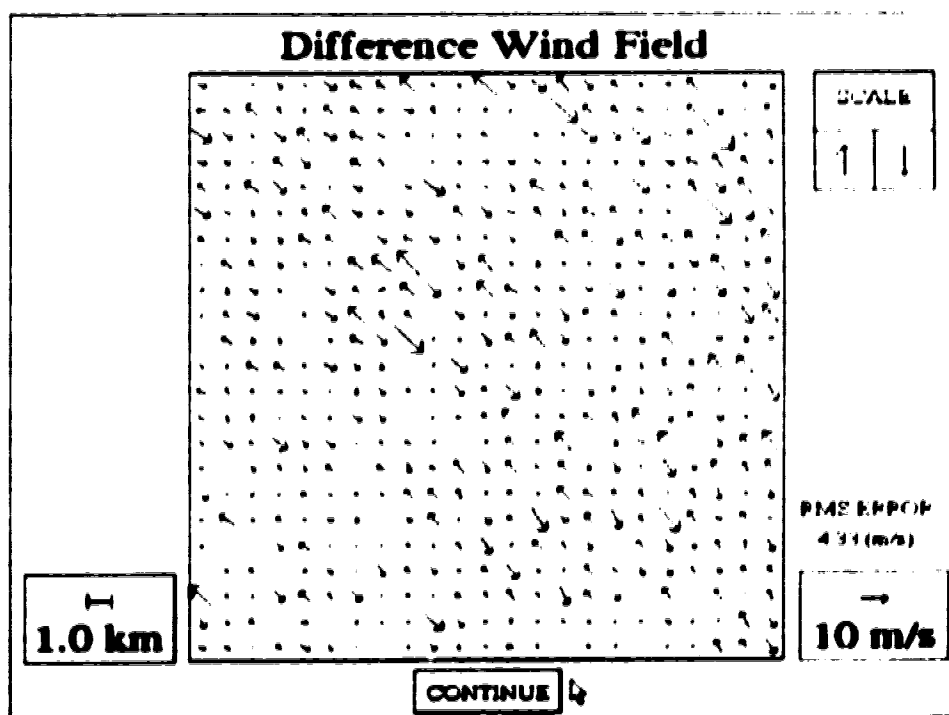
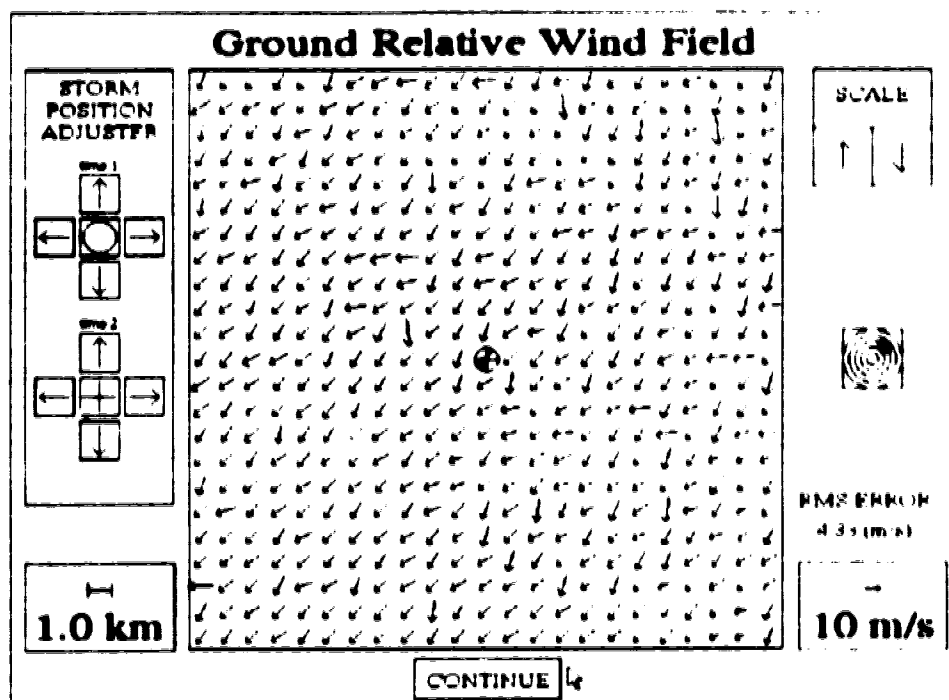


Figure 4.8B SDD wind and error fields for best wind speed synthesis (see also Figure 4.8A).

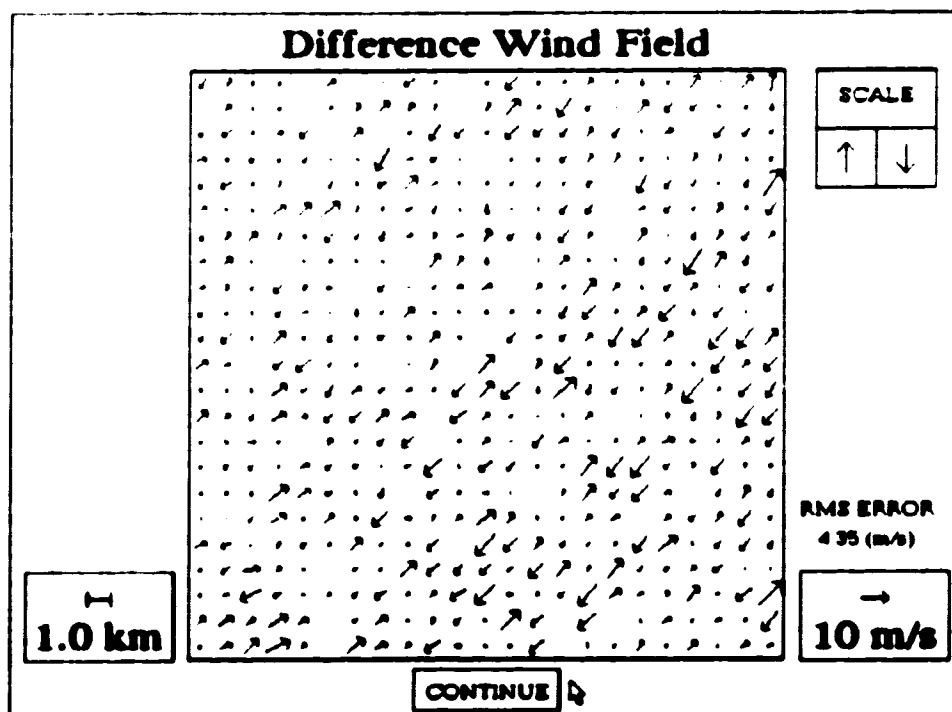
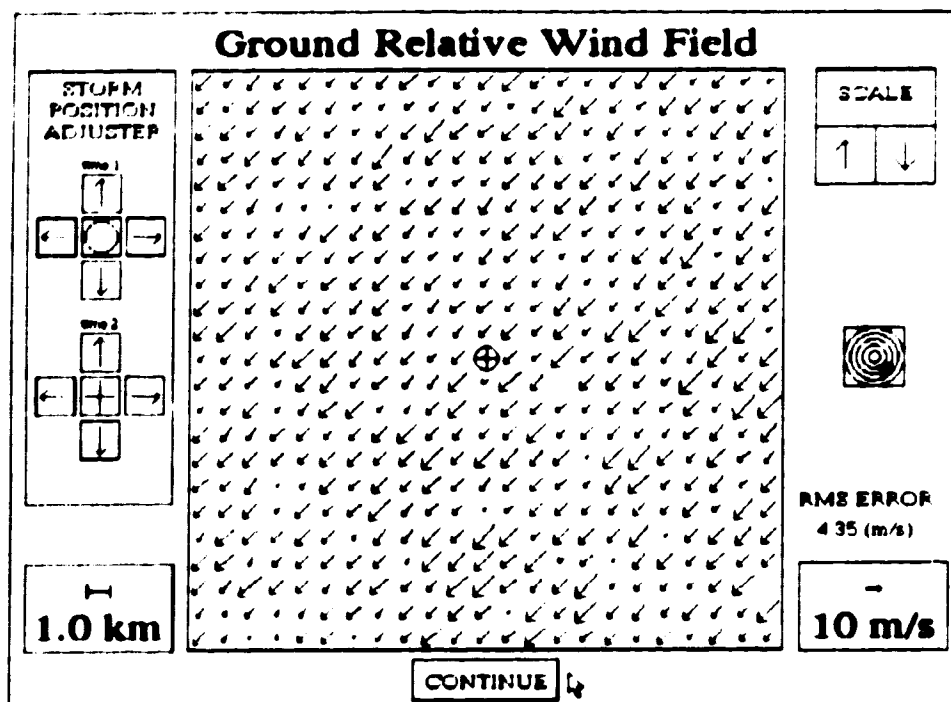


Figure 4.8C SDD wind and error fields for best direction synthesis (see also Figure 4.8A).

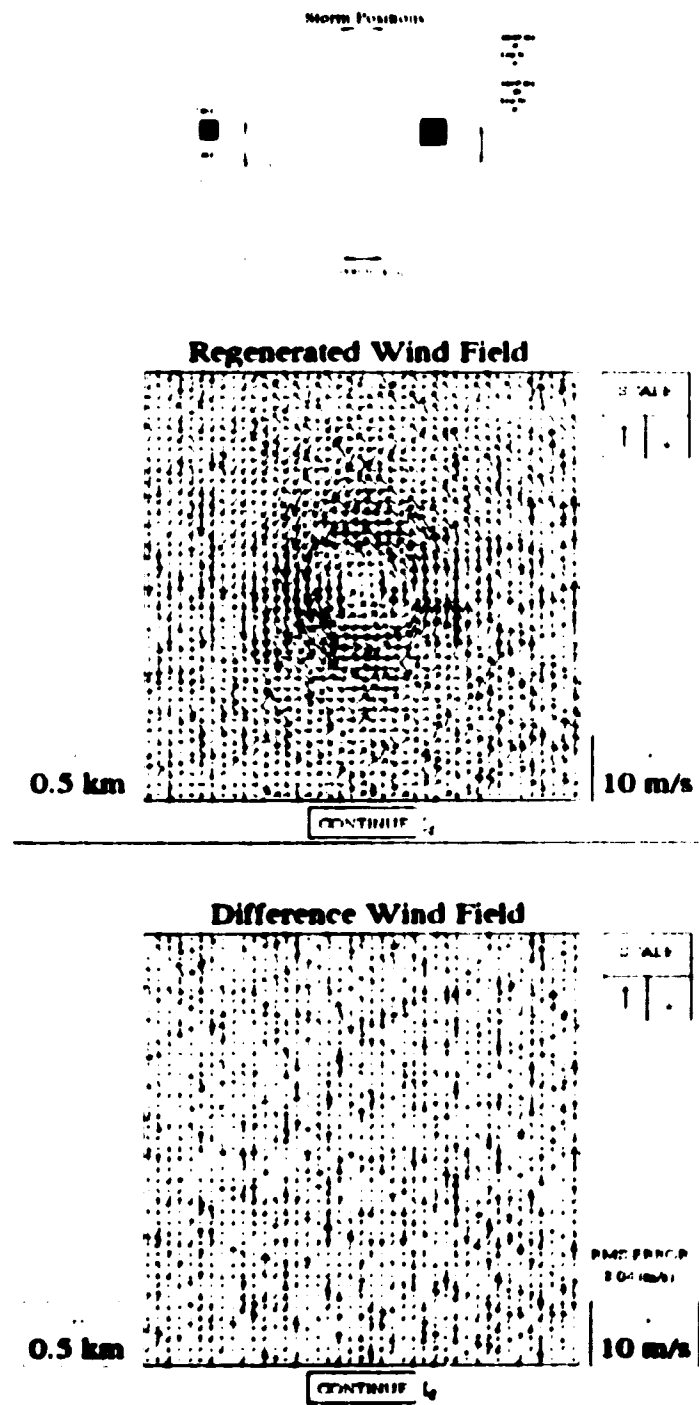


Figure 4.9 Dependency of true wind orientation on SVD reconstruction of mesocyclones. The difference wind field is mostly perpendicular to the average viewing angle of the mesocyclone. Errors of 2 m/s were added to the radial components before synthesis.

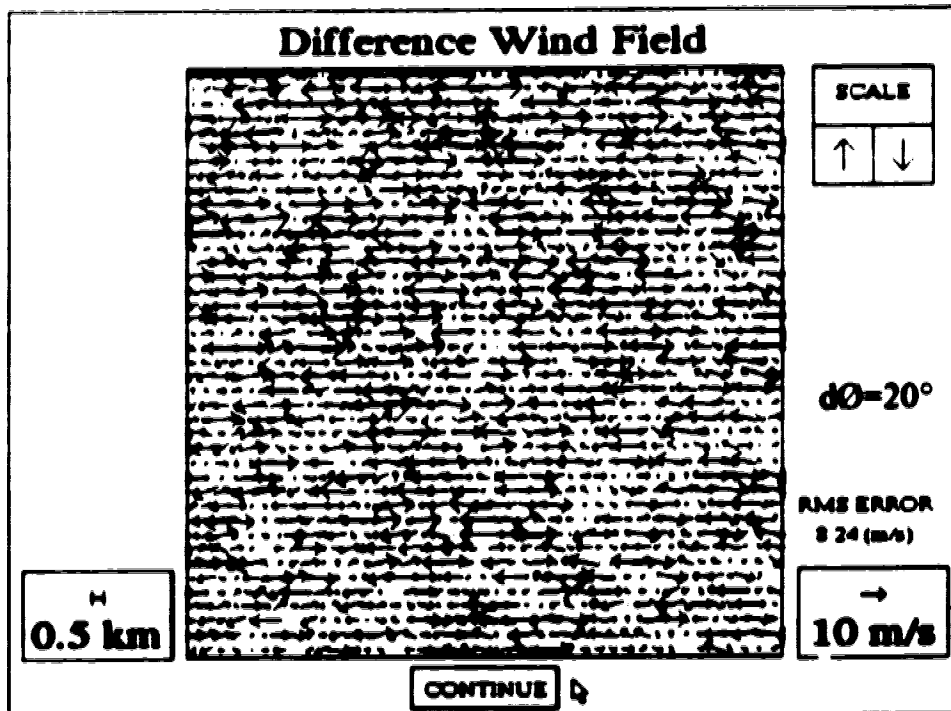
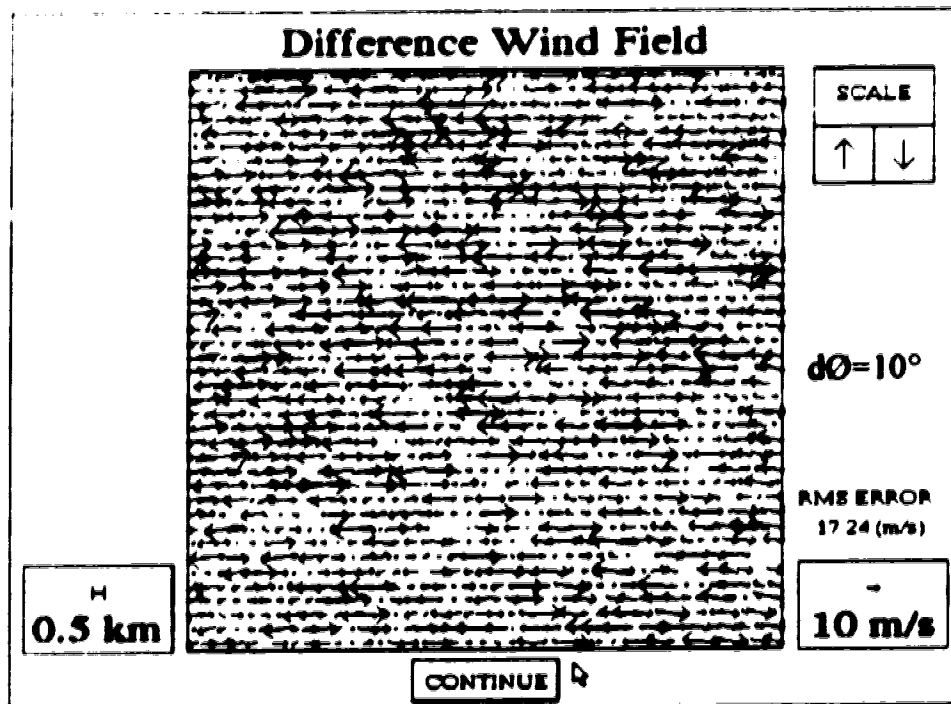


Figure 4.10A Velocity difference fields for a SDD reconstruction of a mesocyclone at 60 km to the north of the radar. The top panel is for an angular separation of 10° , the bottom for 20° . Spectral noise of 2 m/s was added to the radial components.

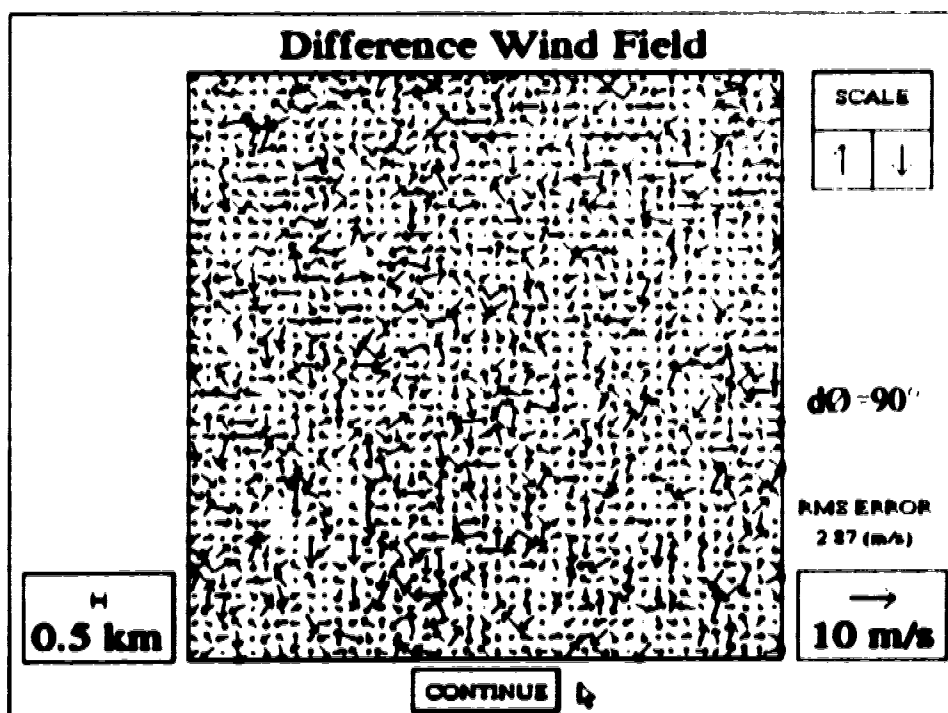
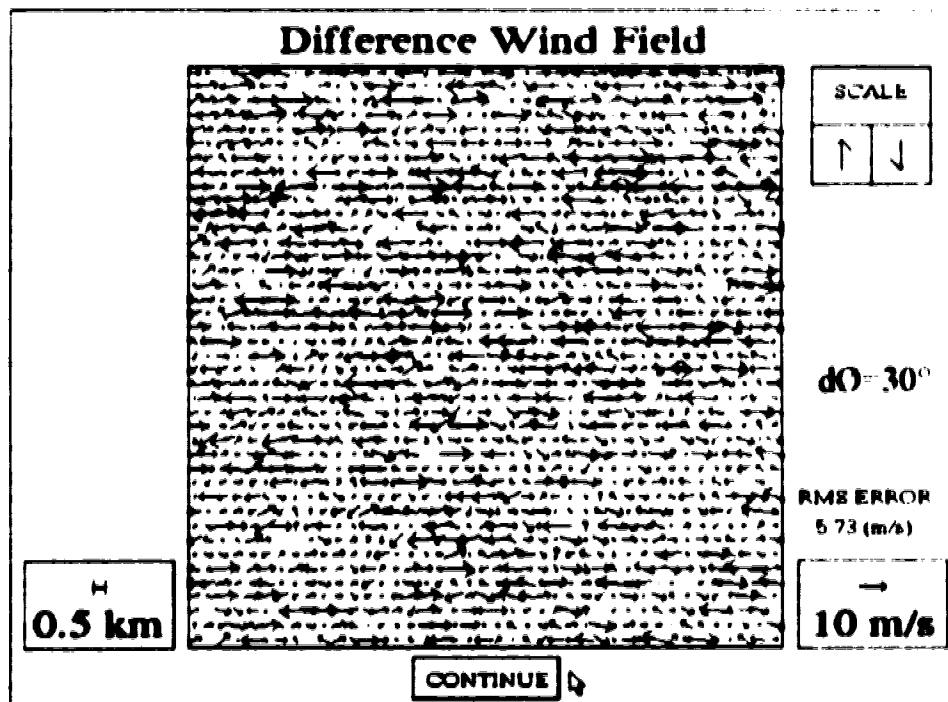


Figure 4.10B Same as in Figure 4.10A but for angular separations of 30° (top) and 90° (bottom).

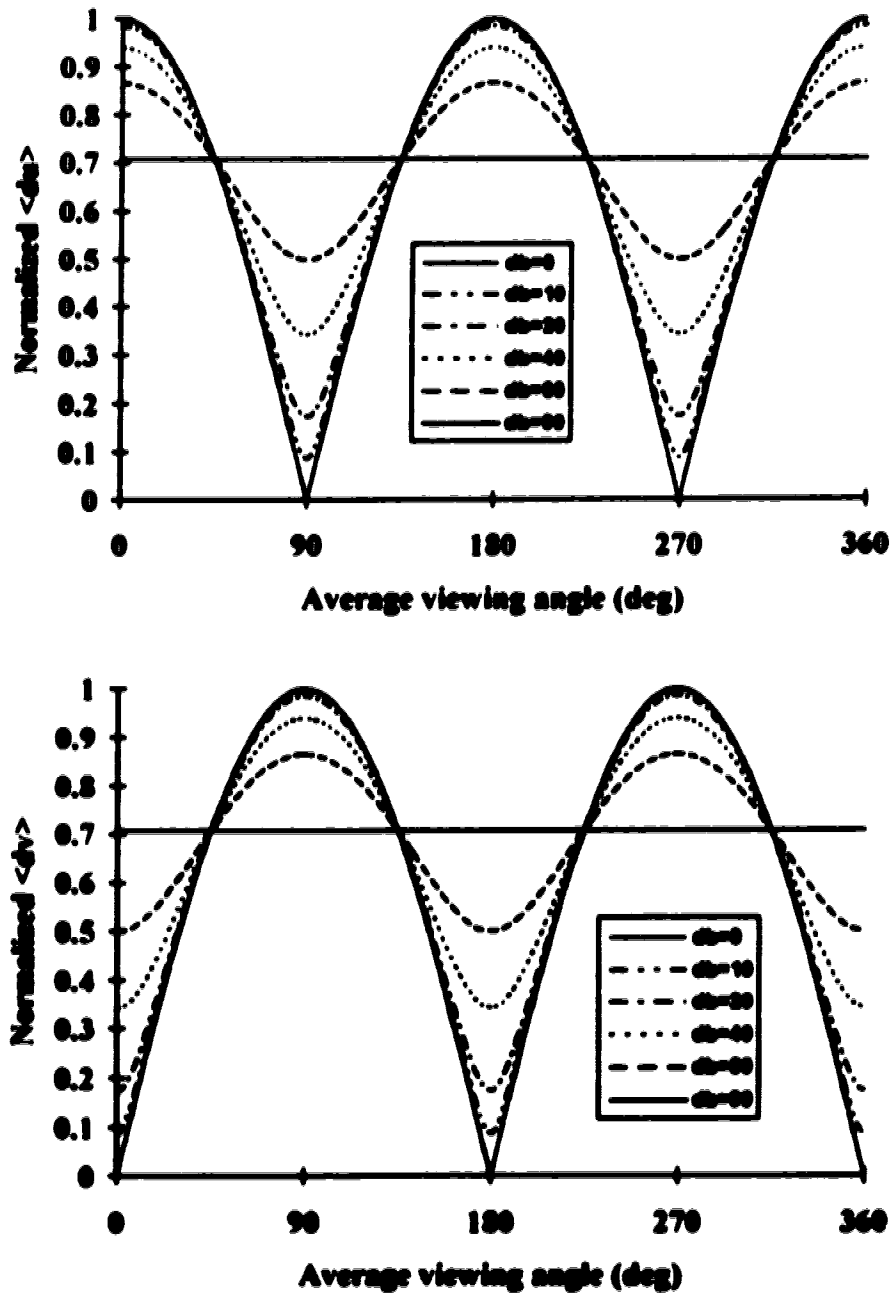


Figure 4.10C Orthogonality of the error wind field for SDD (and dual-Doppler) analyses. Variation of the component errors (normalized to total error) is shown as a function of the average viewing angle and the angular separation (db on the legend). When $db=0^\circ$, the error field is perfectly perpendicular to the average viewing angle. When $db=90^\circ$, the errors are evenly distributed on the x and y axes (i.e. random orientation).

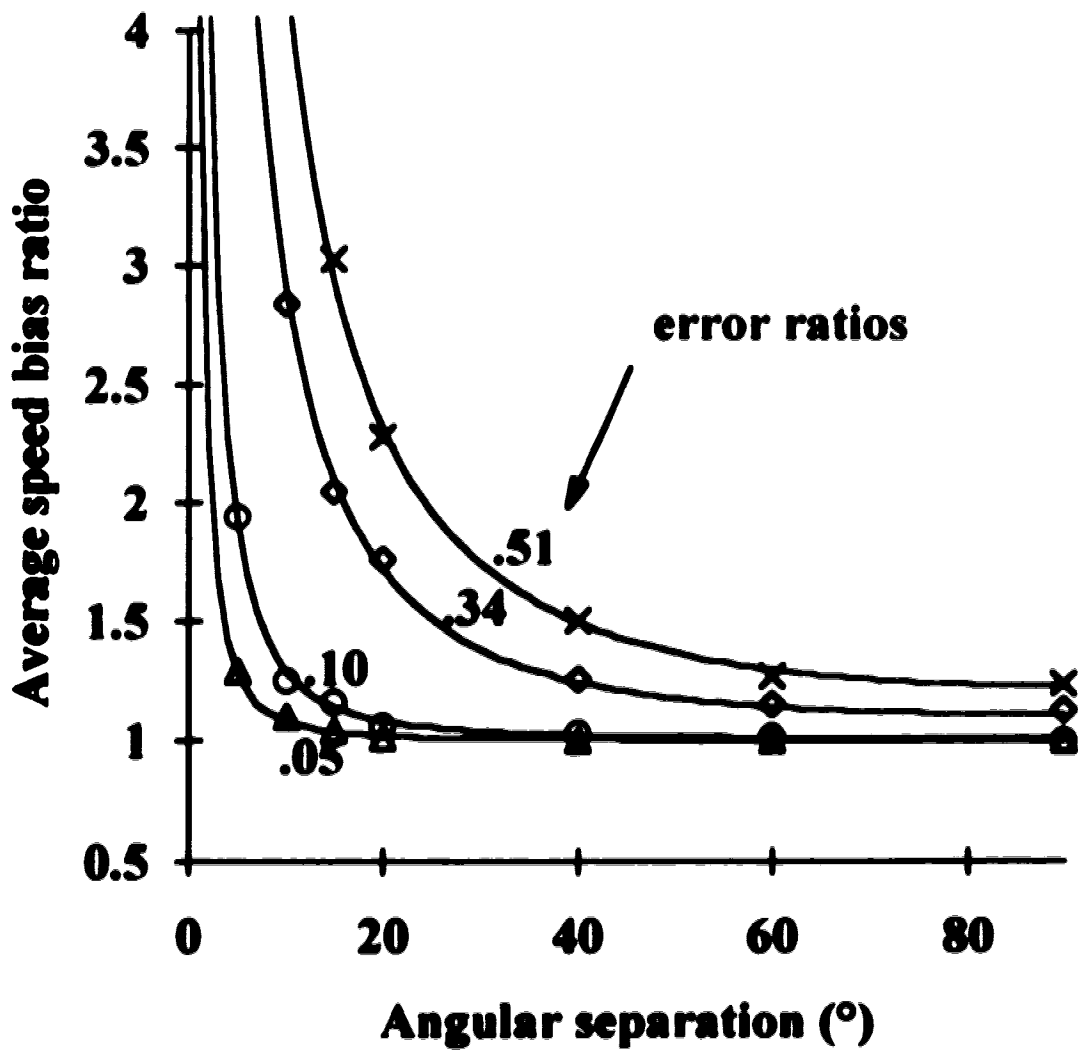


Figure 4.11 Average speed bias ratio for SDD or dual-Doppler vector synthesis as a function of angular separation and error ratio. The solid lines represent the values calculated from (4.3). The data points indicated by the various symbols are simulation results.

5. Synthetic dual-Doppler analyses of mesoscale phenomena over Alberta

Two convective storms and one gust front which were observed by the Carvel radar in central Alberta during the summer of 1993 are studied using the SDD technique. SDD results obtained are compared and combined with results from research experiments and current conceptual models in order to give credence to the technique and to infer case specific conceptual models for the observed phenomena.

5.1. The gust front of August 06 1993

A long gust front was observed on the Carvel radar on August 06 1993. This gust front originated from storms which were beyond the short Doppler radar range ¹. The reflectivity and velocity fields from the 0.5° PPIs are shown in Figure 5.1. The front first became apparent in the northwest quadrant of the radar domain at 1930Z. It then progressed eastward and maintained its identity until about 2300Z. Examination of the 0.5° and 1.5° PPI scans revealed that the gust front had a depth of 1500 to 1800 m, as evidenced by the disappearance of echoes due to overshooting (not shown). The radar imagery showed the gust front to be about 100 km in length during its lifetime of over 3 hours.

The radar data used in this case come from the 0.5° PPI scans. This is the lowest scan available and the best for the analysis since gust fronts tend to be relatively shallow features. The reflectivity and velocity structure appeared to be quasi-steady between 2010Z and 2210Z based on an animation of the 0.5° PPI radar imagery. The analysis presented here is based on three observation times: 2050Z, 2120Z and 2150Z.

5.1.1. SDD analysis results

Figure 5.2 shows the regions used for the SDD gust front analysis using the 2050Z and 2150Z radar scans. Within this hour, the gust front moved eastwards, changing significantly the angle at which it was viewed from the radar. The computed height and

¹The short (unfolded) Doppler range is 113 km. This is the range to which the dual PRF technique is used, allowing the data to be de-aliased. The long (folded) Doppler range extends to 256 km, but the data may be aliased since the measurements are made at only one PRF.

height change of the radar beam in the center and at the four corners of the areas chosen is shown in Figure 5.3. Beam heights being compared are within about 300 m. The decoded radial wind fields for the analysis regions (Figures 5.4-5.5) show how the "red" gust front changed to a "red-blue"² during the eastward progression. Contained in this change of "color" is the information which allows the synthesis of the horizontal wind field for the feature.

The wind field derived from the SDD technique (Figure 5.6) shows the calculated ground relative wind field. The flow is west-southwesterly at 15 to 20 m/s, the direction of the flow being the same as the translation of the gust front and perpendicular to the line of echoes. This finding conforms to what is observed with conventional observations of gust fronts as they pass through weather stations. Unfortunately, no such observations were available for this front as it tracked through an area void of weather stations. Figure 5.7 shows the flow when the front motion is removed (i.e. the flow relative to the gust front). The relative wind values are much lower than the ground relative field, suggesting that most of the momentum in this gust front came from its translation. Nevertheless, the relative flow shows a speed of 5 to 10 m/s, mostly from the west-southwest, suggesting that other processes were giving an additional "push" to the gust front.

Figure 5.8 shows the vorticity of the derived wind field. As expected, no obvious patterns are apparent in this linear feature. The convergence field however shows that convergence was occurring at the leading edge of the front while divergence dominated on the trailing edge (Figure 5.9).

5.1.2. Inference of a "roll" circulation

In an attempt to further analyze the circulation associated with the gust front, the SDD analysis was repeated on more northerly sections of the front (Figure 5.10A-B). Keeping in mind that the Doppler observations come from PPI scans, this gives a way to analyze wind flow as a function of height. The analyzed wind field indicates that the flow at the northern part of the front is weaker than that at the south (Figure 5.10C). Alternatively, by considering beam heights, it can be said that the westerly flow at 1500 m AGL is weaker than that at 500 m. Combining this finding with the low level convergence-divergence pattern depicted in Figure 5.9, a schematic flow pattern of a "roll" circulation is inferred (Figure 5.11). The axis of this "roll eddy" is parallel to the gust front. A similar

²Analogous to the optical Doppler effect, targets receding from the radar are displayed in red while targets approaching the radar are displayed in blue.

roll within a gust front was detected near Denver on June 20, 1986, using lidar observations (Christian 1993)

5.1.3 Test of the quasi-steady assumption

Fulfillment of the quasi-steady requirement can be tested by using different time intervals in the SDD analyses of a given case. If a feature is steady, the resulting wind fields should be similar regardless of the time intervals used. The test was performed by doing two more SDD analyses using the additional observation at 2120Z. Analyses were done for the 2050Z to 2120Z and the 2120Z to 2150Z time frames. The ground relative wind field results for these two cases are shown in Figures 5.12 and 5.13. Comparisons with Figure 5.6 show that the wind fields from the 30 minute syntheses are similar but noisier than the 60 minute synthesis. This is due to the smaller angular change undergone by the front during 30 versus 60 minutes. These results suggest that the front was quasi-steady from 2050 to 2150Z.

5.2. The severe storms of July 29-30 1993

July 29 and 30 1993 proved to be very active severe weather days over central Alberta (ALWC 1993 severe weather log book). Several long lived severe storms tracked rapidly from the southwest on the afternoon and evening of July 29 and into the night of July 30. Moist, unstable and sheared conditions provided the environment to sustain such storms. The 500 and 250 mb height charts (not shown) suggest that a short wave embedded in a strong south-southwest flow triggered the storms. One of these storms was examined during two stages of its lifetime using the SDD technique. Figure 5.14 shows the 0.5° PPI reflectivity and velocity fields of the storm as it tracked northeastward. The windows on the velocity frames show the areas used for the analyses. The Doppler scans of 2310Z and 2340Z were used to look at the storm at an early stage, while the 0030Z and 0100Z observations were used to study a latter stage.

5.2.1. SDD analysis results

The analysis results using the 2310Z and 2340Z observations are shown in Figure 5.15, along with the storm positions, beam heights and radial wind fields used for the case. The ground relative flow is quite weak in sharp contrast to the rapid movement of the storm (50 km/hr from the southeast). By subtracting the storm translation, we infer

that a strong northeasterly storm relative flow dominates the area examined. In addition, a cyclonic structure can be seen on the southeastern edge of the storm. It is likely that the strong northeasterly flow is the warm and moist inflow into the storm. Average beam height calculations show this inflow to be at a height of about 600-1200 m.

The 0030Z and 0100Z observations yield similar results (Figure 5.16). Being at a shorter distance to the radar, these observations come from a level of 400-900 m. The inflow is still dominant, however it is stronger and more northerly than that observed at higher levels. The cyclonic structure seen in the 2310-2340Z analysis is not apparent. Since the results between the two cases are comparable, the quasi-steady assumption of the SDD technique is justified.

By using the 1.5° Doppler scans, the northeasterly inflow was further investigated. Results from the scan using the 0030Z and 0100Z observations (Figure 5.17) suggest that the inflow remains dominant from 1000 to 2500 m.

5.3. The Holden tornadic storm (July 30 1993)

One of the July 29-30 1993 supercell storms (section 5.2) formed 160 km south of the Carvel radar at 0000Z on July 30. This cell tracked northeastward at 50 km/hr during the evening and dissipated by 0500Z, 160 km east of the radar. A tornado spawned from this storm did significant damage in the Holden area, 120 km east-southeast of the radar. Various damage occurred to several farm installations, including the complete destruction of one home. Based on the damage, inspectors from the ALWC classified the tornado as F3 on the Fujita scale³. The Doppler displays showed a weak velocity couplet from 0140Z to 0410Z. Unfortunately, the cell was out of the short range Doppler domain when the tornado occurred. Nevertheless, an SDD analysis of the storm prior to the touchdown was done since the cell was visible on short range Doppler for over 2 hours before the tornadic event. The analysis reveals the existence of the mesocyclone which eventually led to the tornado. Figure 5.18 shows the reflectivity and velocity fields of the 0.5° PPI scans at 0150Z, 0220Z and 0250Z. Associated with the intense storm tracking along the edge of the radar range in the southeast quadrant is a small velocity couplet, just visible on the periphery of the images. Only the 0.5° scans were used in the case shown here, as precipitation was not detected over much of the suspected couplet on the 1.5° and 3.5° Doppler scans.

³An F3 tornado consists of winds from 158-206 mph giving severe damage (Fujita 1971).

5.3.1 SDD analysis results

An SDD analysis was performed using the 0150Z and 0250Z observations (Figure 5.19). The motion is almost purely azimuthal - an ideal configuration for the SDD technique. The beam heights are shown in Figure 5.20. Beam height changes are quite small, being almost always less than 300 m. The average height is about 1500 m above ground. The radial component sets used for the analysis are shown in Figures 5.21 and 5.22, with the velocity couplet visible on both time frames. Areas to the southeast of the couplet are void of data because they are beyond the unfolded Doppler range.

The ground relative wind field generated from the two observations is shown in Figure 5.23. The storm relative flow, shown in Figure 5.24, consists of a strong northeasterly flow over most of the area. As in the storms earlier that day, it is likely that this represents the warm moist inflow to the storm. The 0300Z surface analysis indicated dew points of 16 to 20°C and temperatures of 20 to 26°C in the area within 200 km to the northeast of the storm.⁴ This is consistent with the notion that moist warm air entered the storm from the northeast.

A cyclonic circulation is visible near the center of the storm relative wind field depiction (Figure 5.24), as is strong shear on the ground relative wind field (Figure 5.23). With this mesocyclone being at a range of 105 km, the pulse volume has a diameter of about 2.5 km with a length of 75 m. A grid spacing of 1.0 km was used on the SDD Cartesian grid, which represents a compromise between the angular and range resolutions. With its diameter of about 6 km, the vortex is just being resolved.

The vorticity and convergence fields derived from the generated wind field are shown in Figure 5.25 and 5.26. Both are "noisy" because of the limited angular resolution and the long time interval used in the SDD wind synthesis. A rough guess at the vorticity of this mesocyclone can be made by approximating it to a Rankine vortex with a solid body rotation radius of 3 km and an outer rim tangential velocity of 15 m/s. These approximations would give vorticity values of $1.0 \times 10^{-2} \text{ s}^{-1}$ within 3 km of the center of the feature. Burgess (1976) reports that mesocyclones have an average radius of 2.8 km with a mean velocity of 22 m/s on the outer rim. These values give a vorticity value of $1.5 \times 10^{-2} \text{ s}^{-1}$ within the solid core.

⁴Reporting stations: WVI (Vegreville), YLL (Lloydminster), WLB (Lac La Biche) and YOD (Cold Lake).

5.3.2. Test of the quasi-steady assumption

The quasi-steady requirement was tested by using a third observation of the radial wind field at 0220Z. Results for the 0150Z-0220Z and 0220Z-0250Z runs are shown in Figure 5.27. Both fields reveal the mesocyclone feature as well as the northeasterly storm relative flow previously discussed. The difference fields between the 30 minute time frame analyses and the 60 minute time frame analysis are shown in the bottom panels of Figure 5.27. The wind fields were aligned for comparison using the mesocyclone center, indicated by the arrow at the center. The difference wind field is quite significant in both cases, showing RMS speed differences of almost 10 m/s. This relatively large value is a reflection of changes that occurred in the wind field during the observations. Similar computations were done by Bluestein (1991) and Klimowski (1992) on SDD cases, and RMS speed errors of 5-10 m/s were common, while errors of 10-20 m/s or more existed in certain areas of the analysis. Despite these RMS speed errors, visual inspection of the wind fields obtained using different time frames shows them to be qualitatively similar. Use of the quasi-steady assumption may be justified.

5.3.3. Ground truthing

Figure 5.28 shows the layout of the observations used for the SDD analysis in conjunction with ground truthing available for the tornadic event (ALWC 1993 severe weather log book). Evidently, the observed mesocyclone led to the development of the tornado near Holden. The potential usefulness of the SDD technique for severe weather forecasting stands out in this case. The *added information* generated by the SDD analyzer could have been available to the forecaster shortly after 0220Z. The tornado was not reported on the ground until about 0350Z, implying the potential for 90 minutes of lead time. Usually, a 30 minute lead time is considered excellent for tornadic events.⁴

5.3.4. Insight into storm structure

Some insight into the structure of the July 30 1993 storms can be obtained by using the SDD results in conjunction with other radar products and the Stony Plain upper

⁴In this case, the ALWC issued a tornado warning for the Camrose area at 0122Z, based on radar data. At that time, residents of the Beaver area, in which the tornado eventually touched down, were advised to stay tuned for updates.

air station (WSE) sounding. WSE is located a few kilometers east of the Carvel radar site. Using routinely available conventional radar products, a bounded weak echo region (BWER) can be seen on the southeast flank of the storm. Figure 5.29 shows the various products used to identify the BWER. The 0.4° long range Doppler scans show an indentation (as shown by the arrow) on the right flank. Over this same area, strong reflectivities (or rainfall rates) exist at higher levels. The MAX HEIGHT depiction shows returns greater than 40 dBZ at heights between 10.5 and 12.0 km over the BWER while the ECHO TOPS display shows maximum return heights of 14 km in the same area. The MAX R and CAPPI depictions are consistent with these observations.

A conceptual cross section of the Holden storm is shown in Figure 5.30. This model is based on the various conventional radar products available, the SDD analyses (for locating the mesocyclone in relation to the BWER), and Lemon's (1980) observations of the BWER in a supercell. Part of the mesocyclone is in the BWER, particularly at higher levels. This is consistent with the observation that the mesocyclone couplet was barely visible on the 1.5 and 3.5° Doppler scans, as mentioned previously.

Going one step further, Lemon and Doswell's (1979) conceptual model for supercell airflow was "customized" to the observations available for the Holden storm to produce the three dimensional model in Figure 5.31. The mid and upper level environmental air flow shown is storm relative, with the directions and speeds obtained from the WSE July 30 0000Z upper air sounding. The low level inflow and the placement of the mesocyclone are modeled from the SDD results. The downdrafts (rear and forward flank) were not detected in any way but are included for completeness.

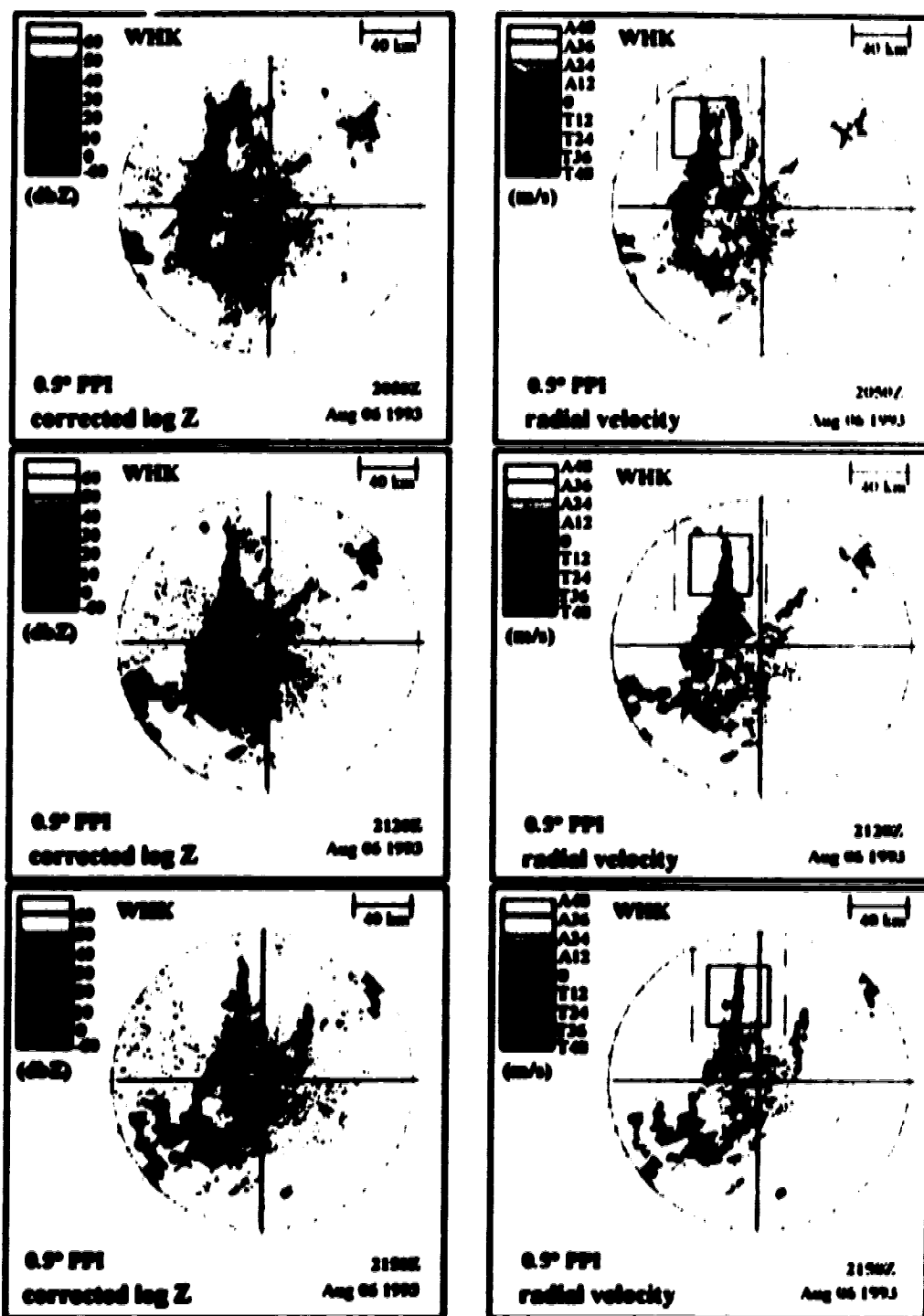


Figure 5.1 The August 06 1993 gust front case showing reflectivity and radial velocity fields at 2030Z, 2120Z and 2150Z. The solid window on the velocity field indicates the areas used for the analysis. The larger window is the area within which the smaller window can be slid to adjust the analysis.

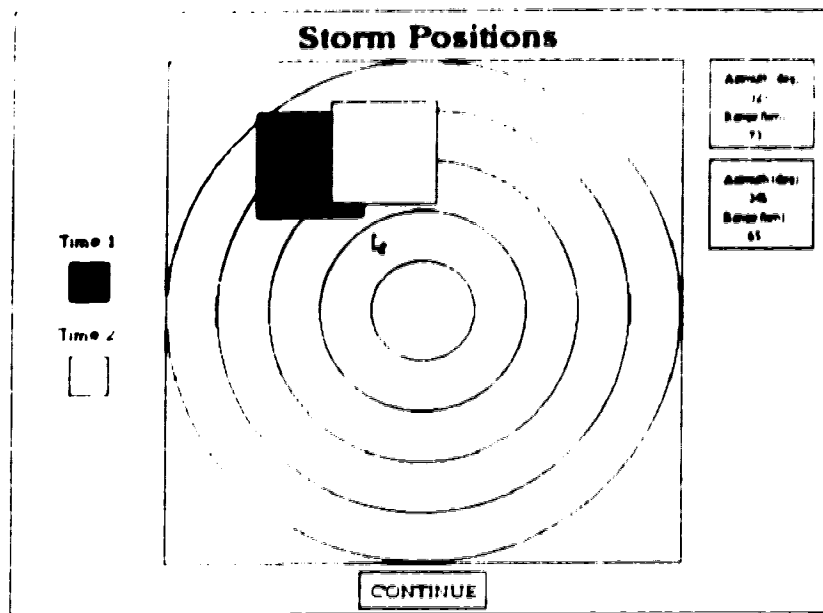


Figure 5.2 Storm positions at 2050Z and 2150Z for the August 06 1993 gust front case. The spacing between rings is 20 km.

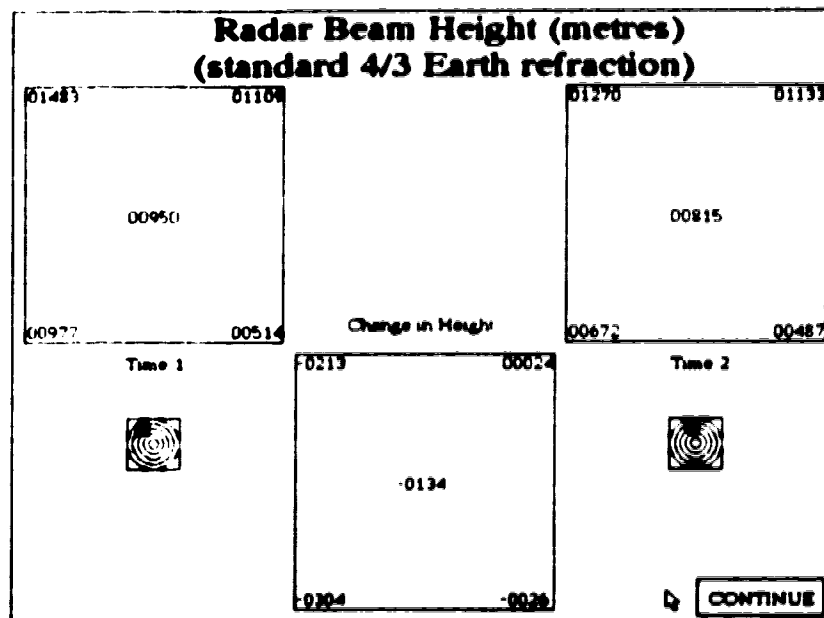


Figure 5.3 Radar beam heights at 2050Z and 2150Z for the August 06 1993 gust front case. Heights for both observations are shown along with the computed change between them.

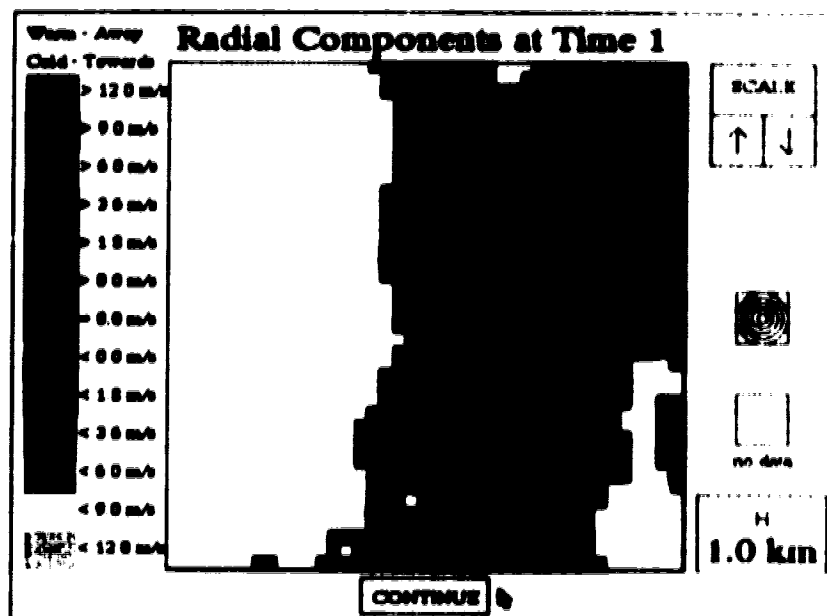


Figure 5.4 2050Z radial wind field for the August 06 1993 gust front case.

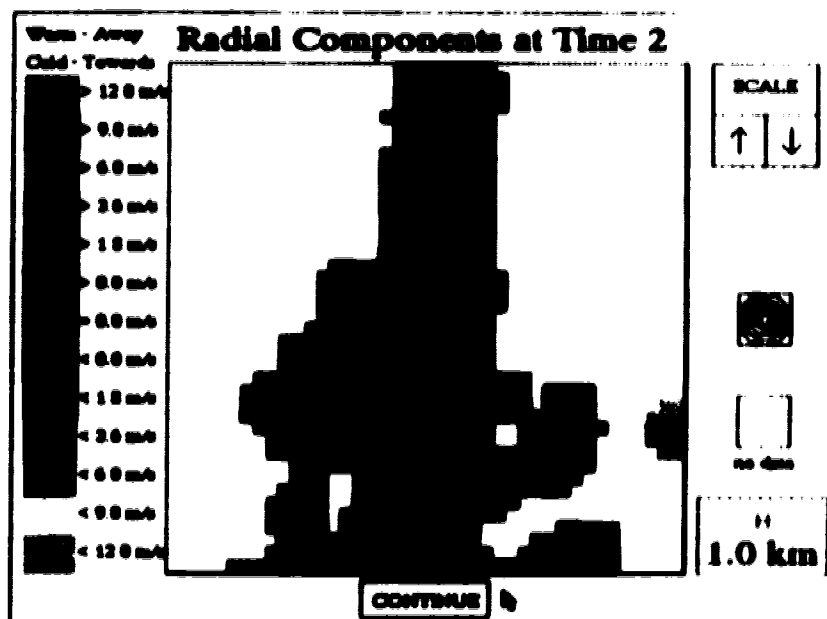


Figure 5.5 2150Z radial wind field for the August 06 1993 gust front case.

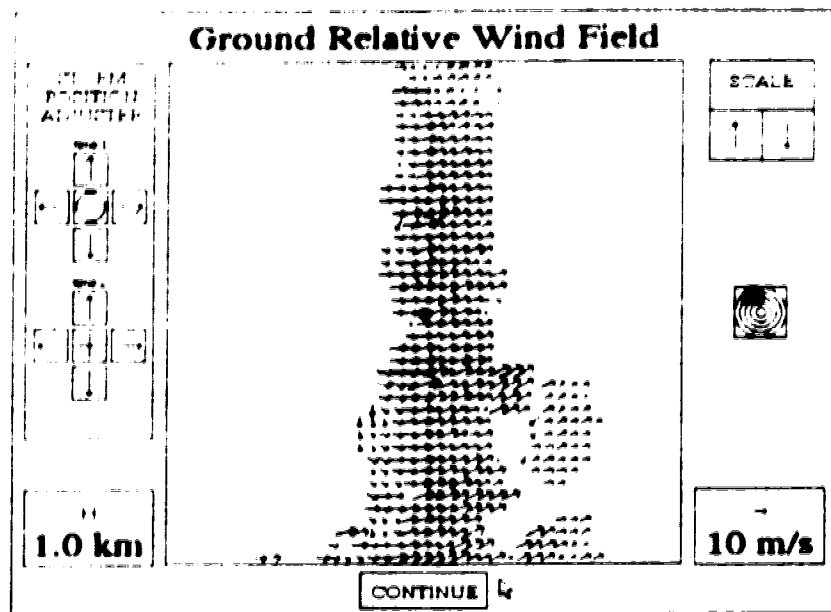


Figure 5.6 Ground relative wind field generated from the 2050Z and 2150Z observations of the August 06 1993 gust front case.

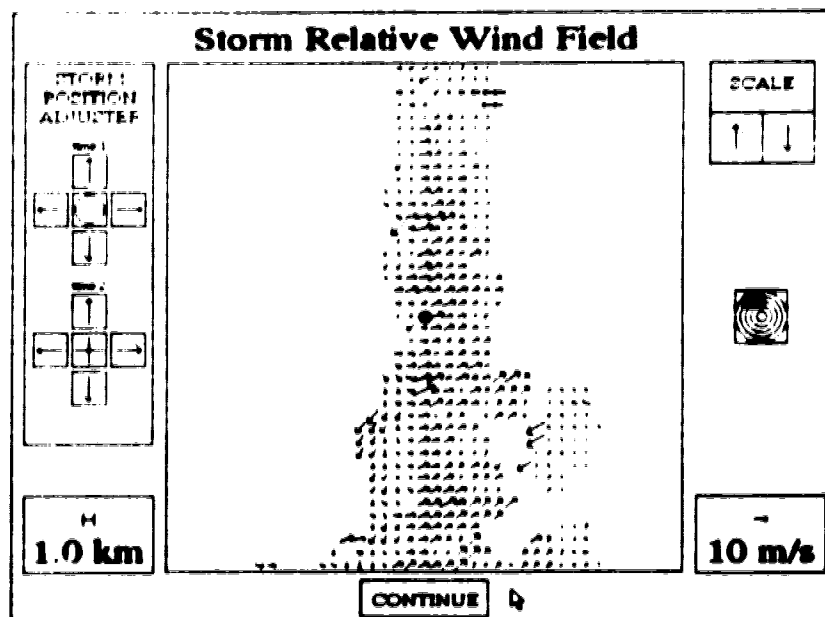


Figure 5.7 Storm relative wind field generated from the 2050Z and 2150Z observations of the August 06 1993 gust front case.

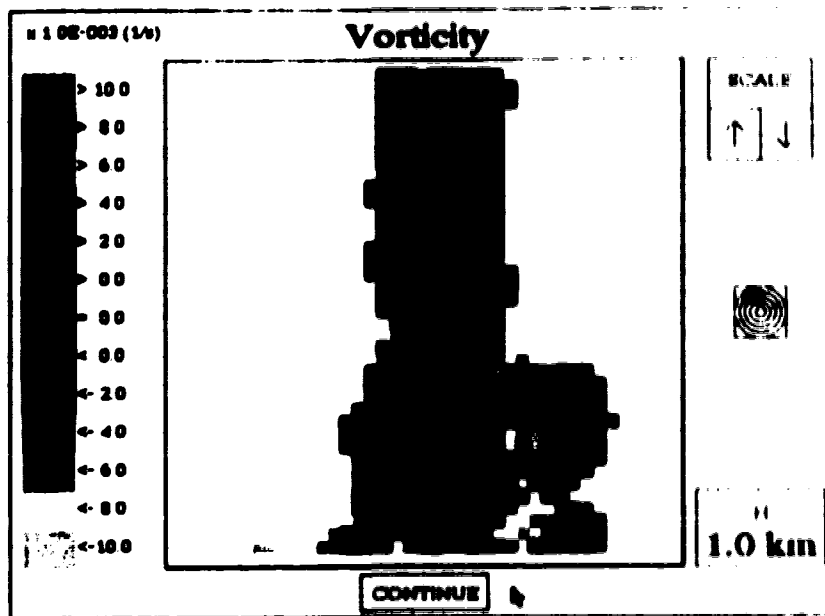


Figure 5.8 Vorticity of the wind field generated from the 2050Z and 2150Z observations on the August 06 1993 gust front. Warm colors indicate cyclonic vorticity.

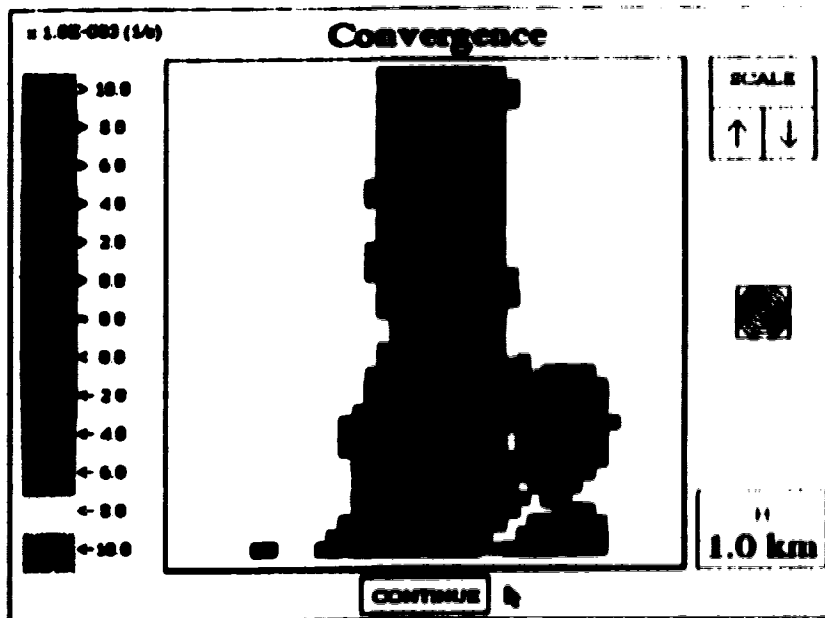


Figure 5.9 Divergence of the wind field generated from the 2050Z and 2150Z observations on the August 06 1993 gust front. Warm colors indicate convergence.

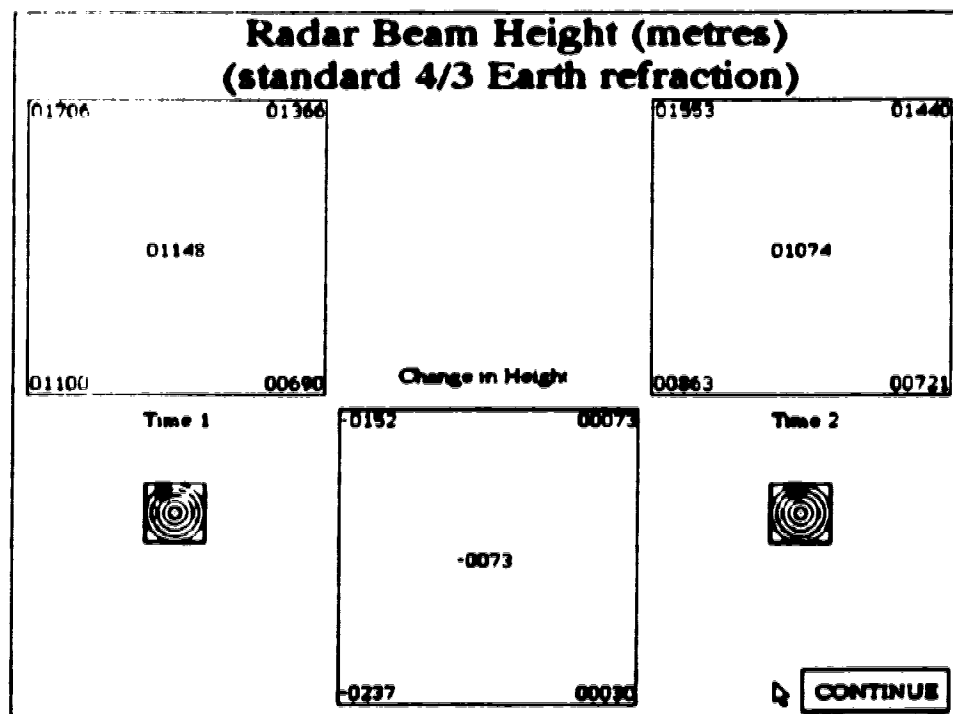
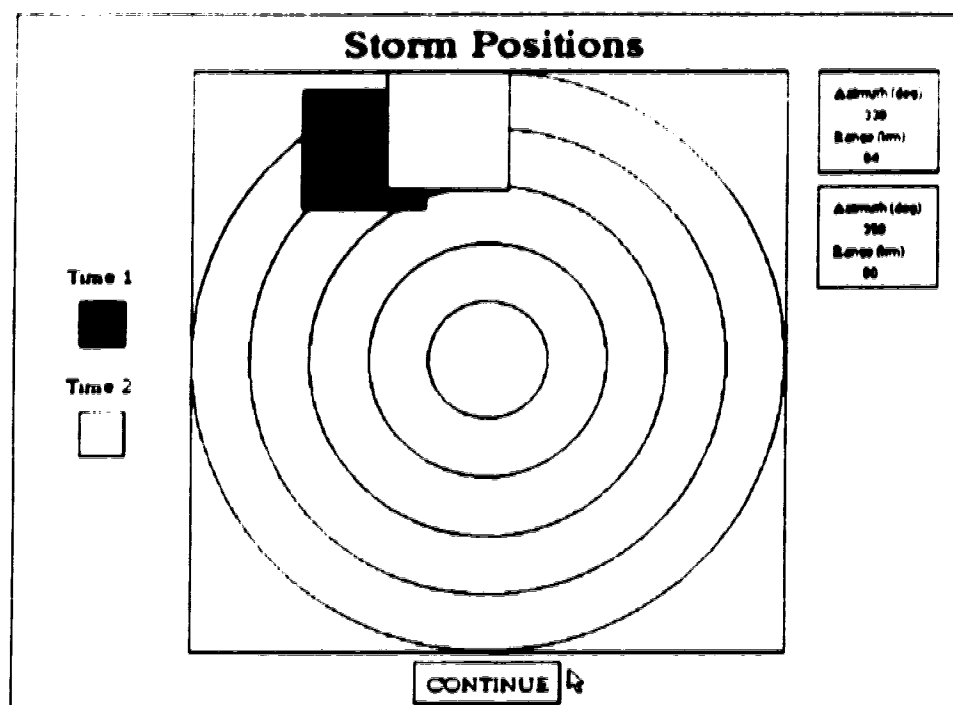


Figure 5.10A SDD storm positions and beam heights for the August 06 1993 gust front using the 2050Z and 2150Z 0.5° radar scans.

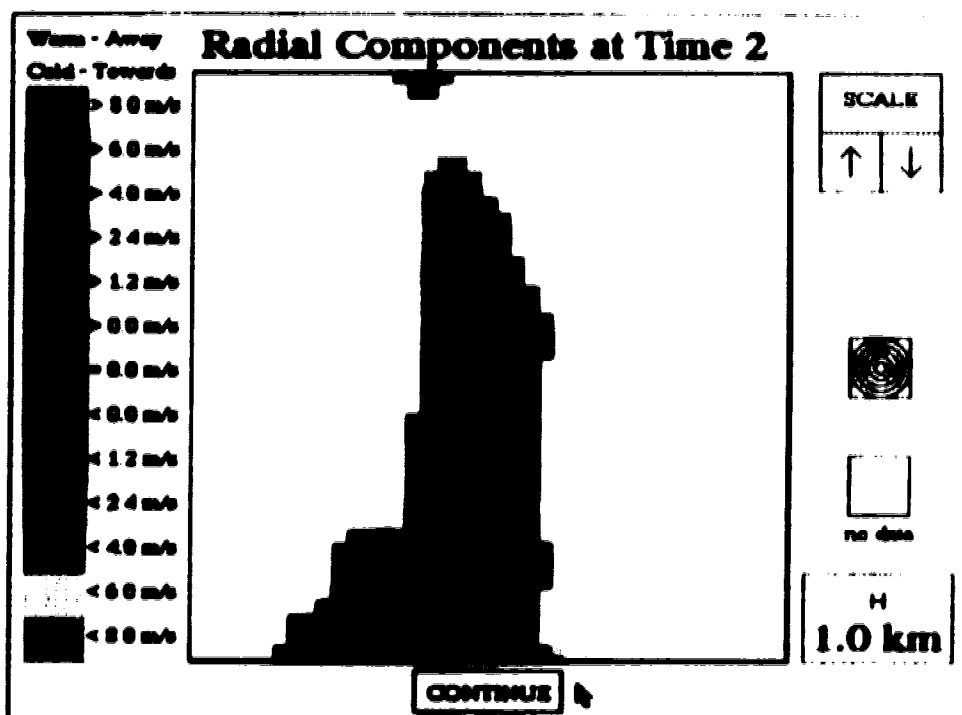
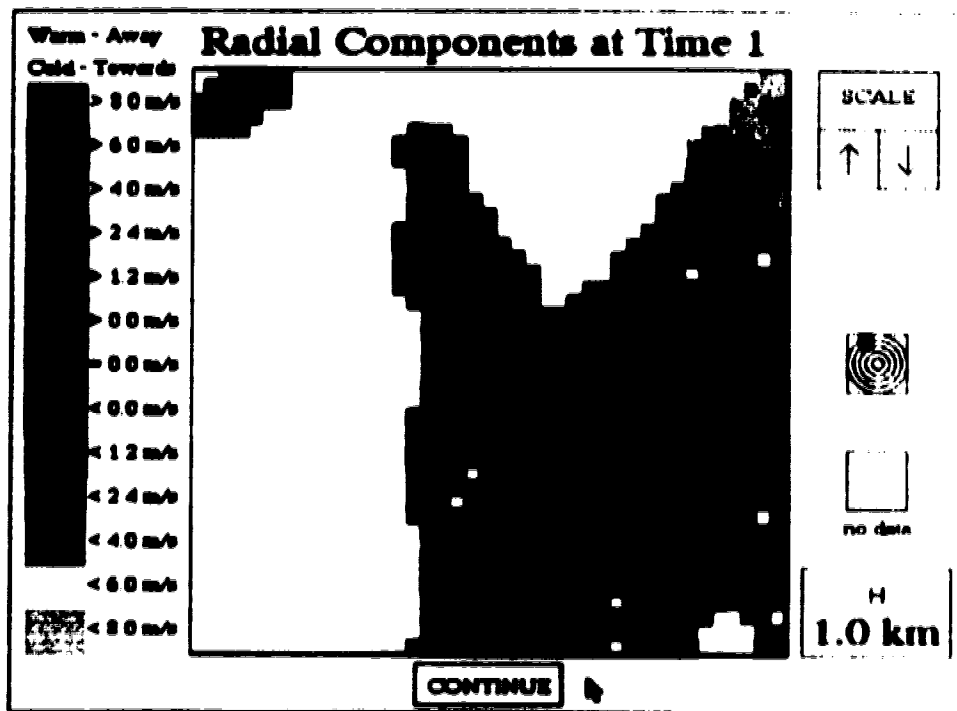
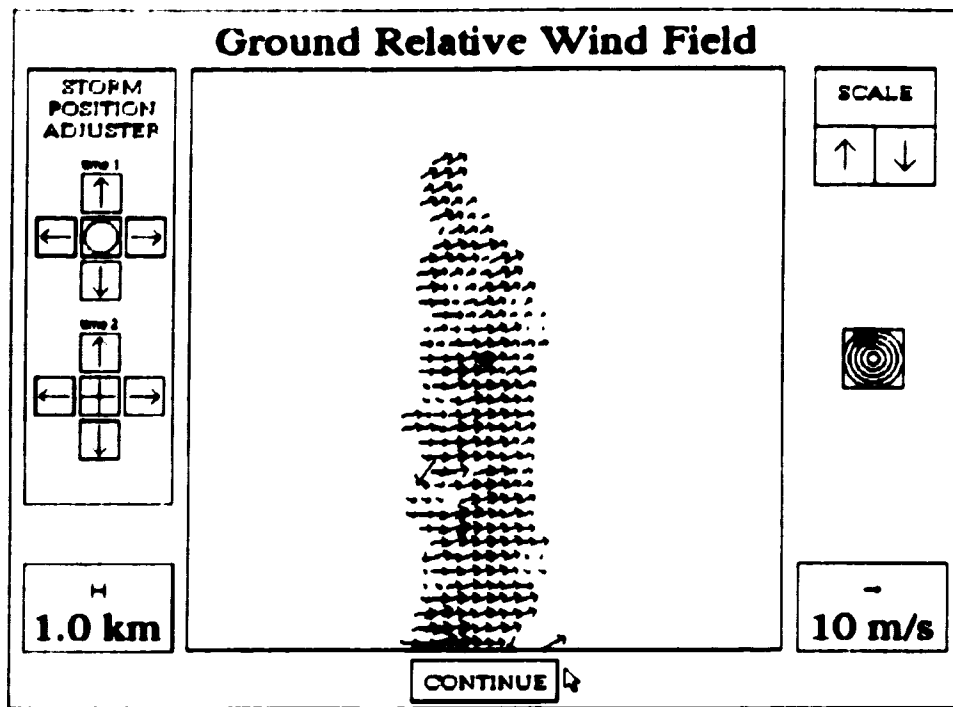


Figure 3.10B 0.5° radial velocity fields for the August 06 1993 gust front (2050Z on top panel, 2150Z on bottom panel).



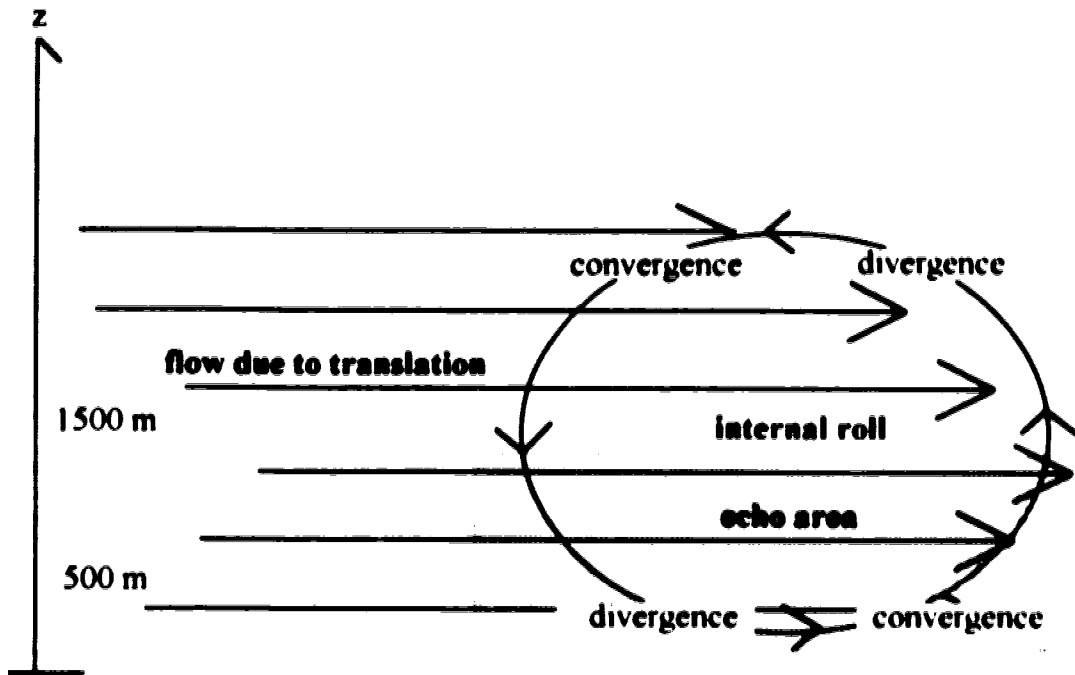


Figure 5.11 Schematic of a gust front cross section based on an SDD analysis of the gust front observed by Carvel radar on August 06 1993. Note areas of horizontal convergence and divergence caused by the storm relative roll circulation.

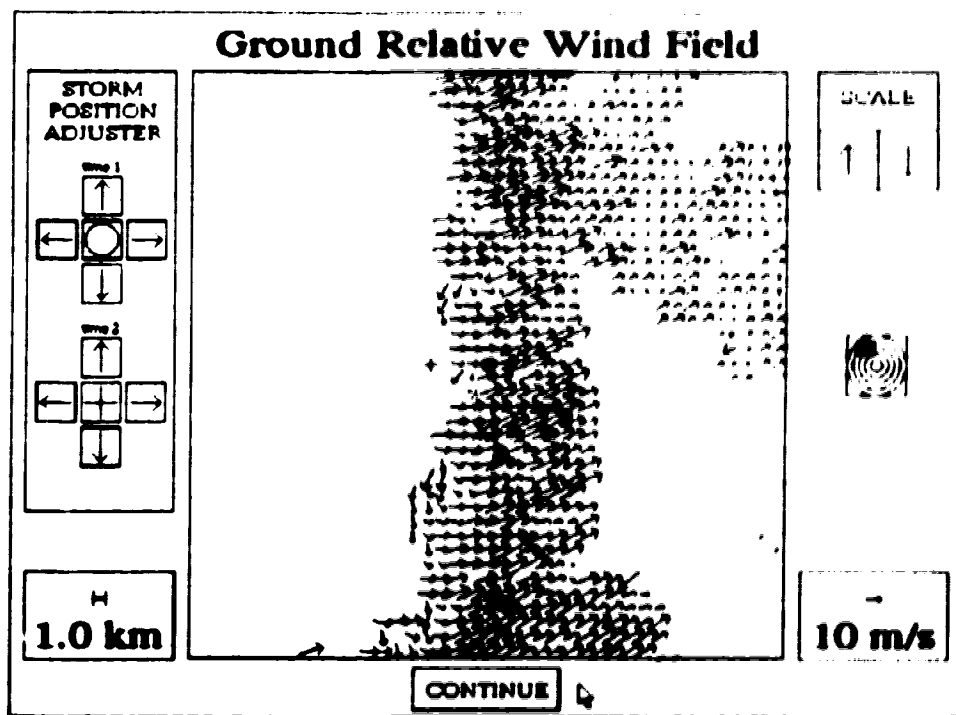
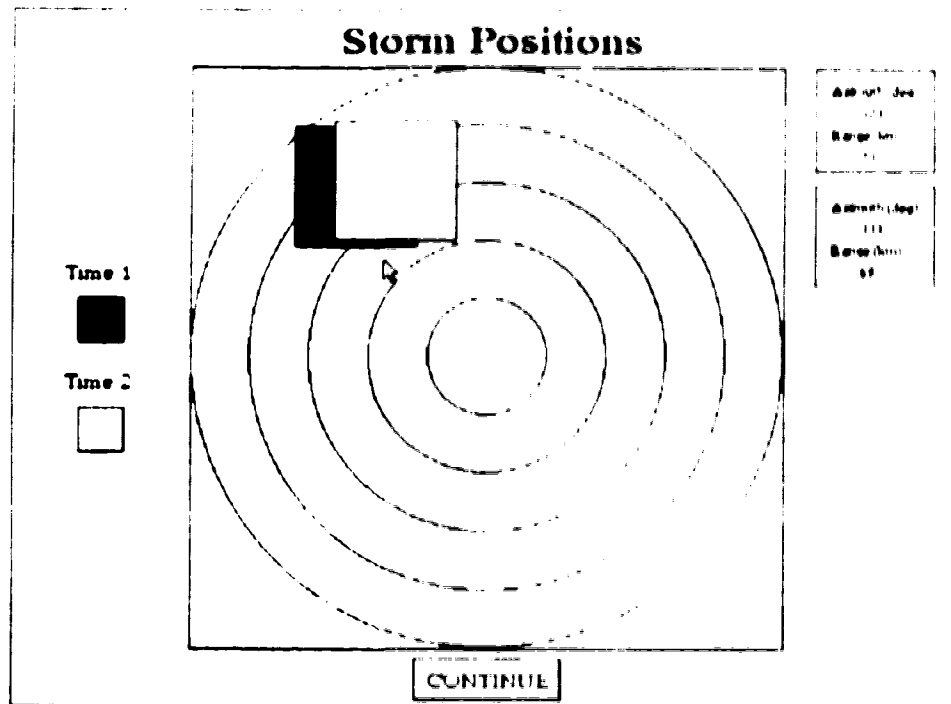


Figure 5.12 SDD analysis results of the August 06 1993 gust front case using the 2050Z and 2120Z 0.5° Doppler scans.

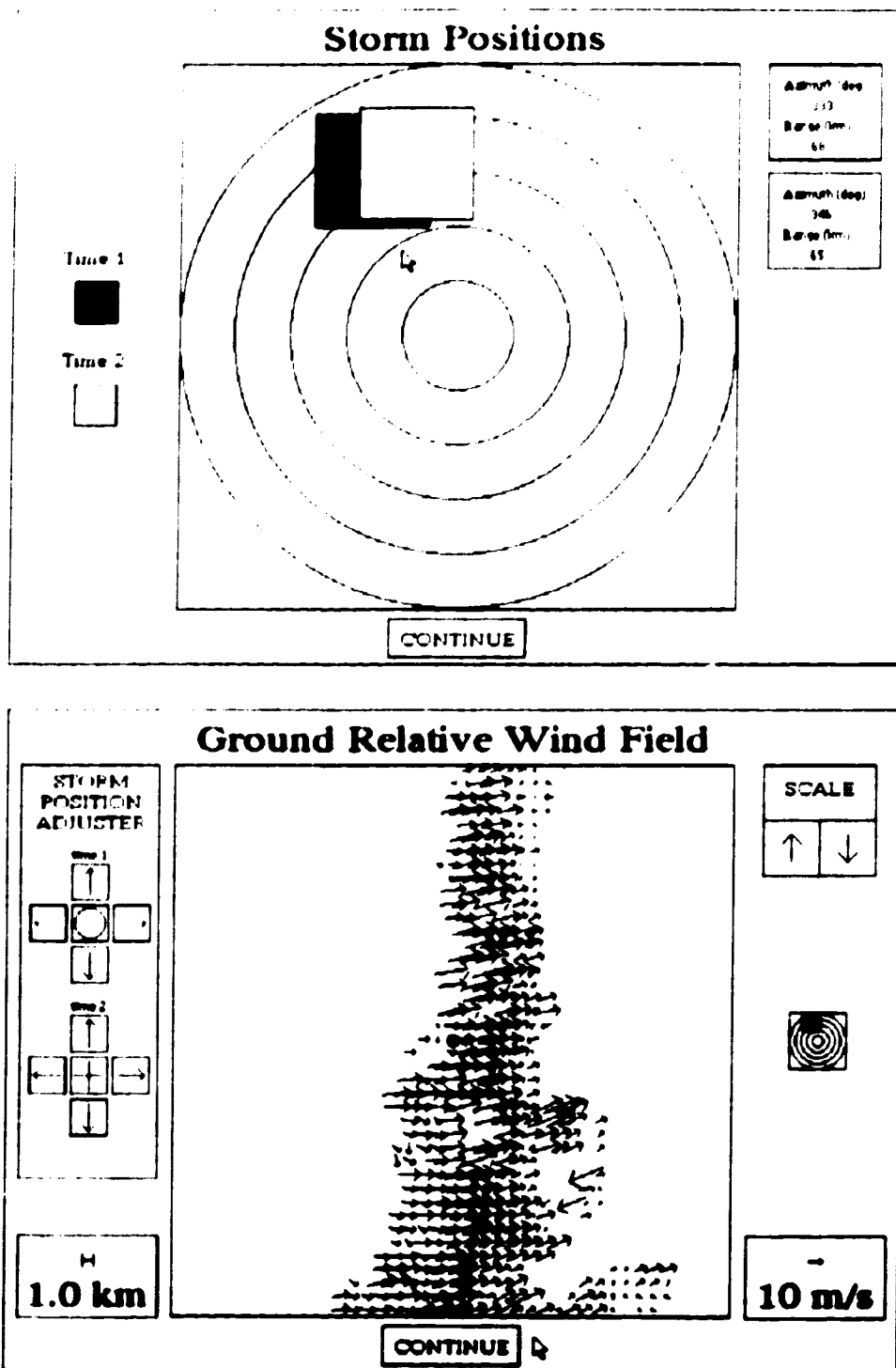


Figure 5.13 SDD analysis results of the August 06 1993 gust from case using the 2120Z and 2150Z 0.5° Doppler scans.

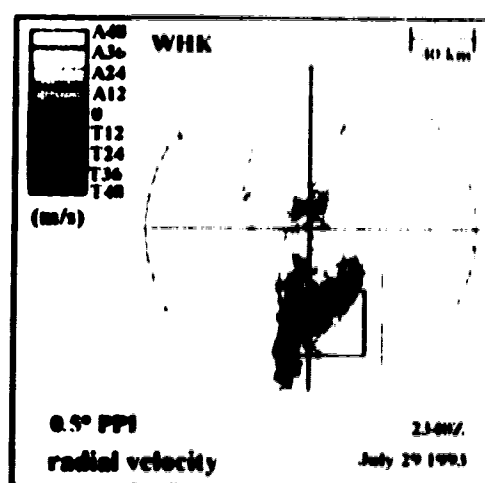
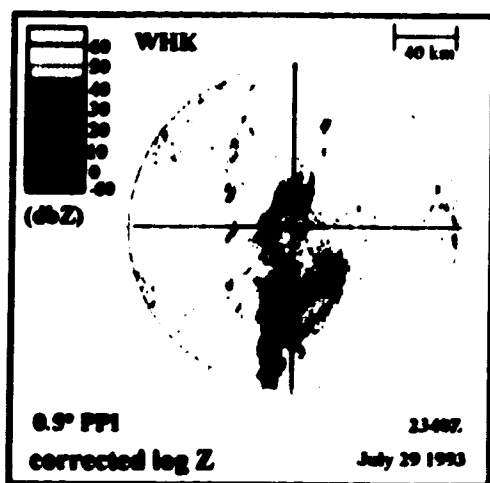
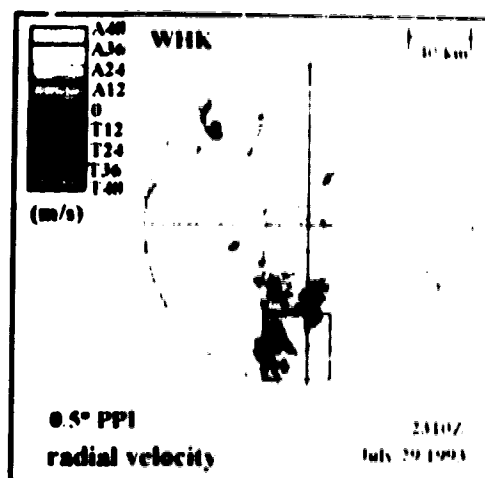
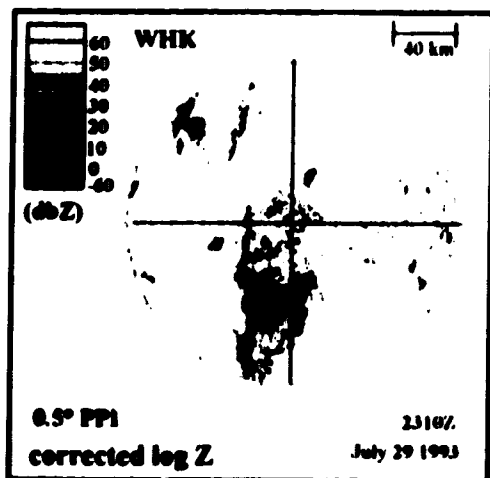


Figure 5.14A The July 29-30 1993 severe storm case (2310Z and 2340Z).

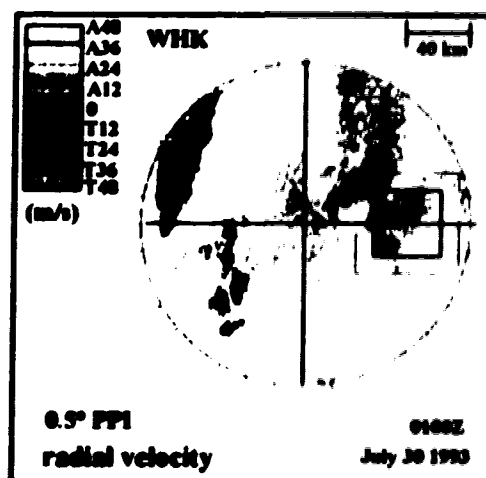
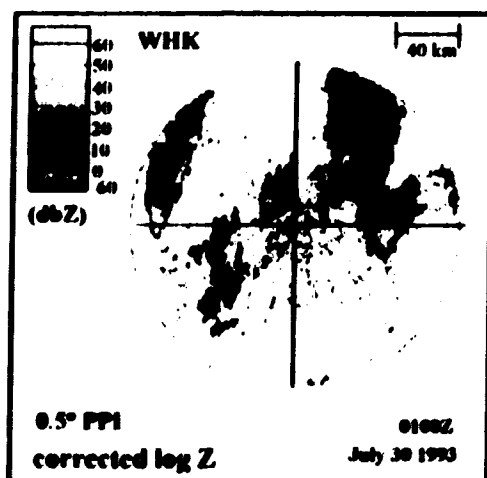
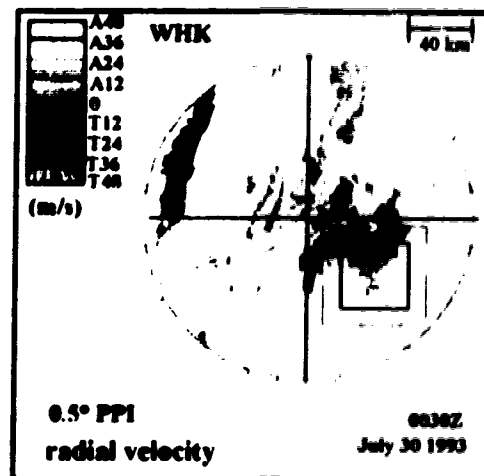
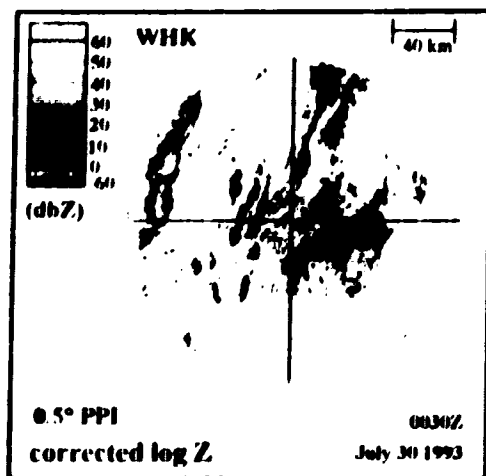


Figure 5.14B The July 29-30 1993 severe storm case (0030Z and 0100Z).

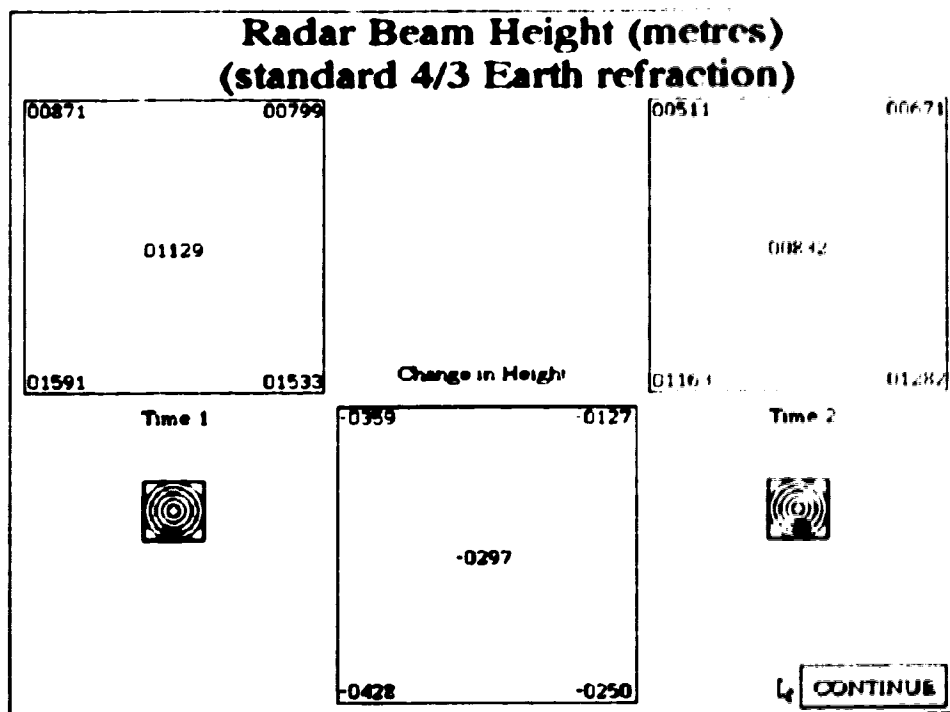
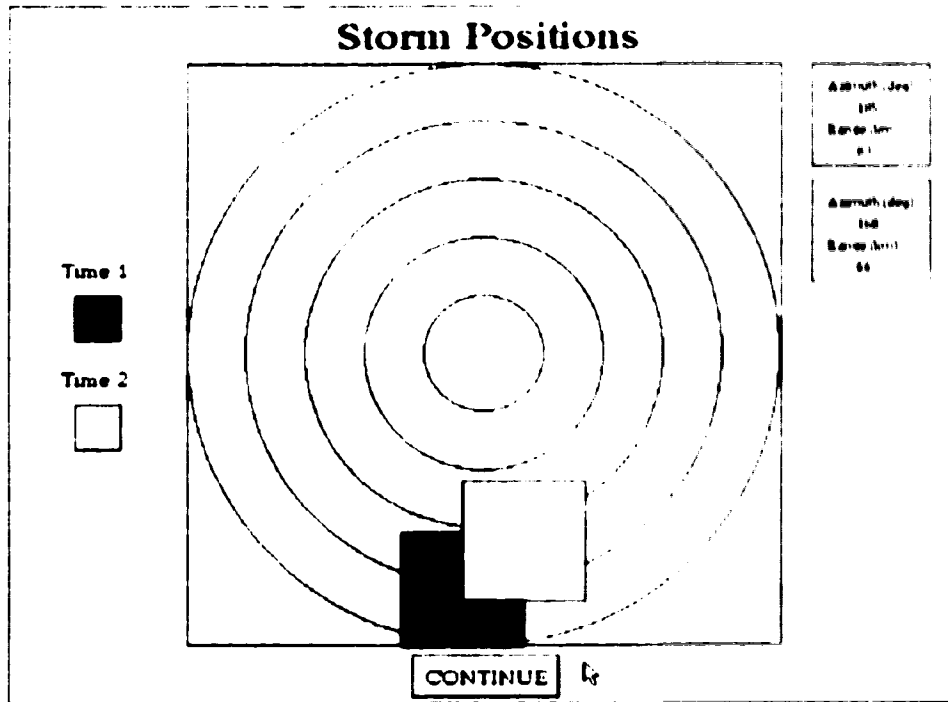


Figure 5.15A SDD storm positions and beam heights for the July 29-30 1993 severe storm case using the 2310Z and 2340Z 0.5° Doppler scans.

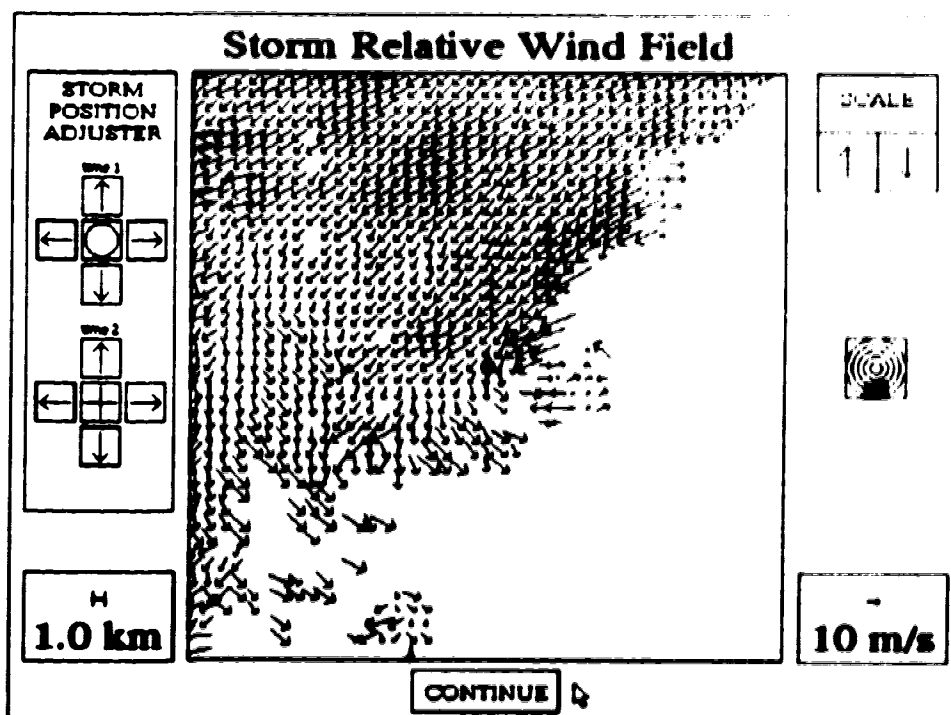
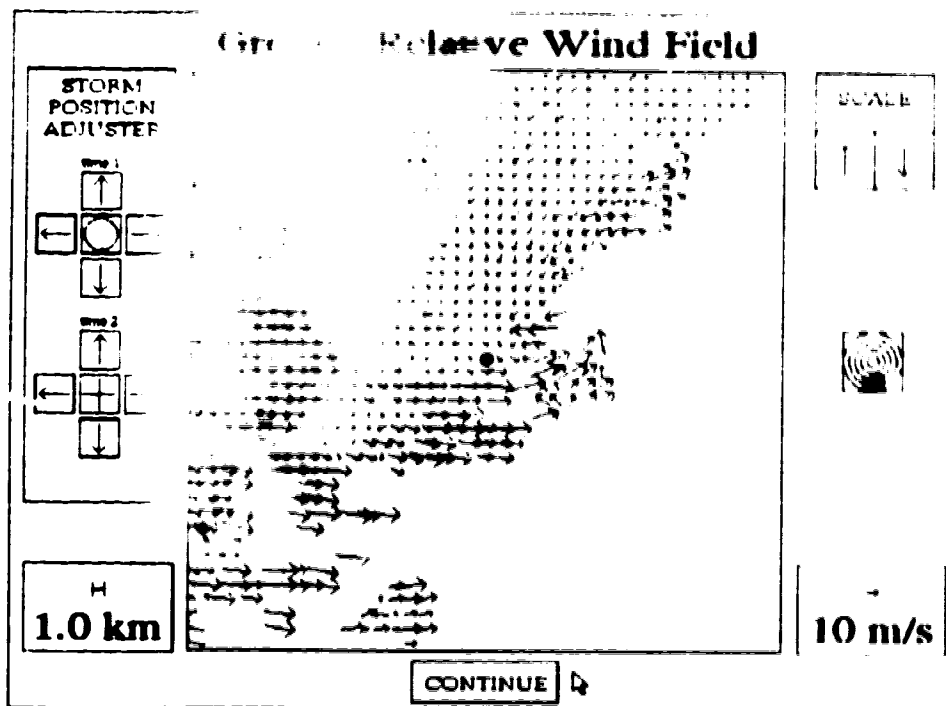


Figure 5.15C SDD wind field reconstructions for the July 29-30 1993 severe storm case based on the 0.5° Doppler scans at 2310Z and 2340Z.

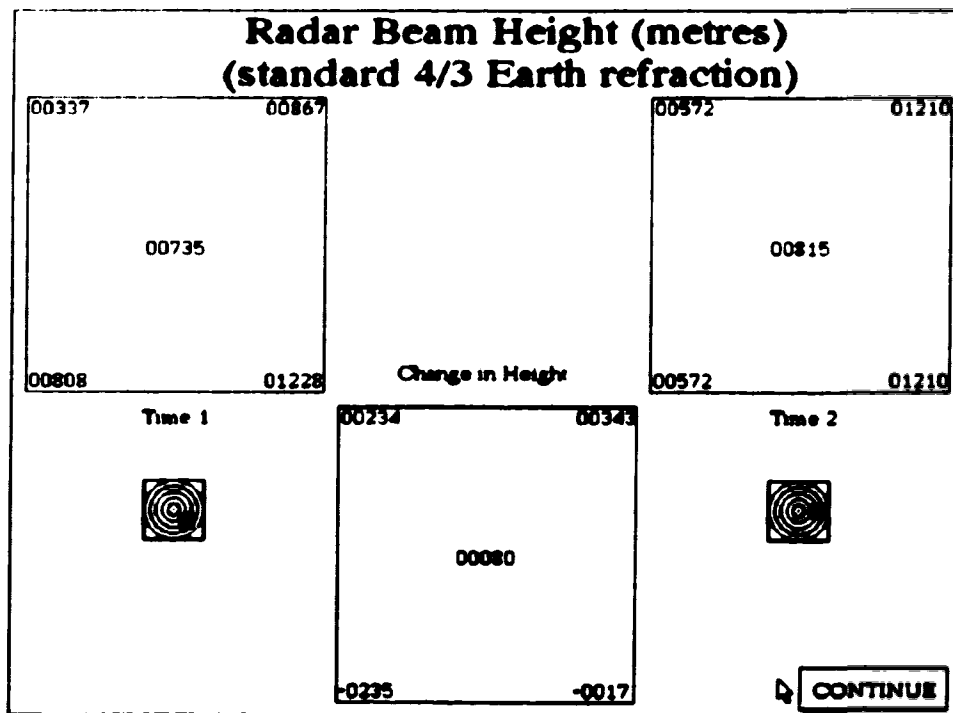
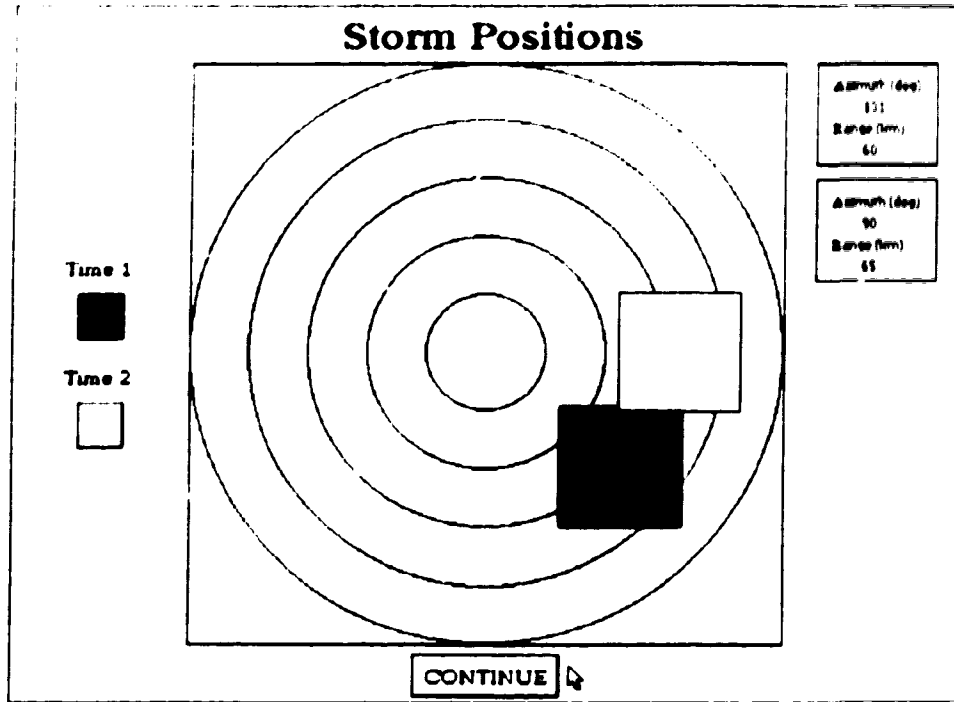


Figure 5.16A SDD storm positions and beam heights for the July 29-30 1993 severe storm case using the 0030Z and 0100Z 0.5° radar scans.

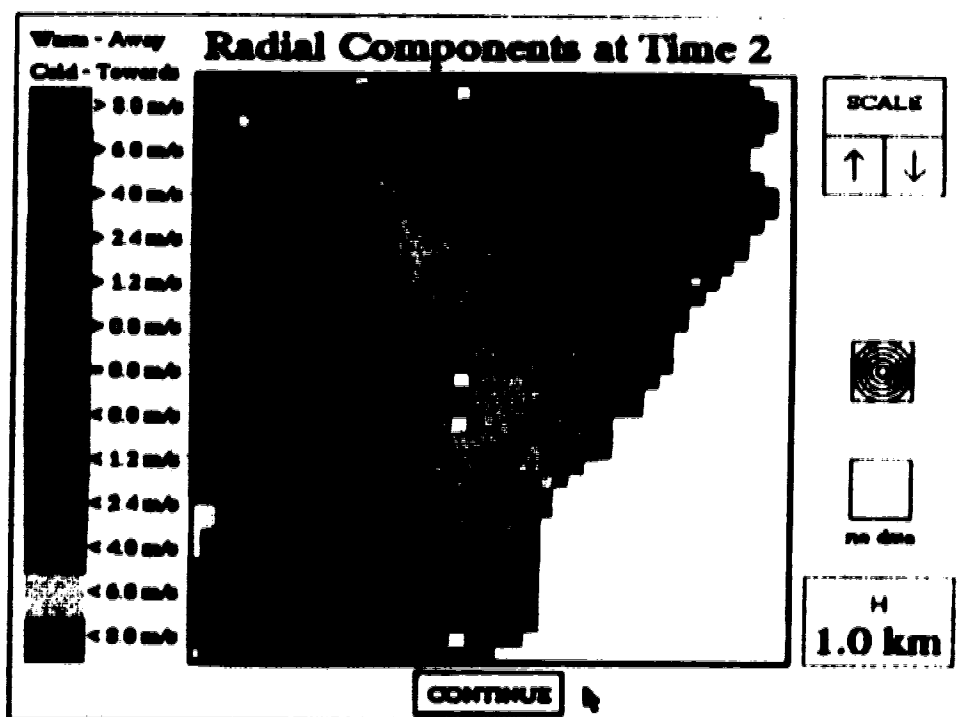
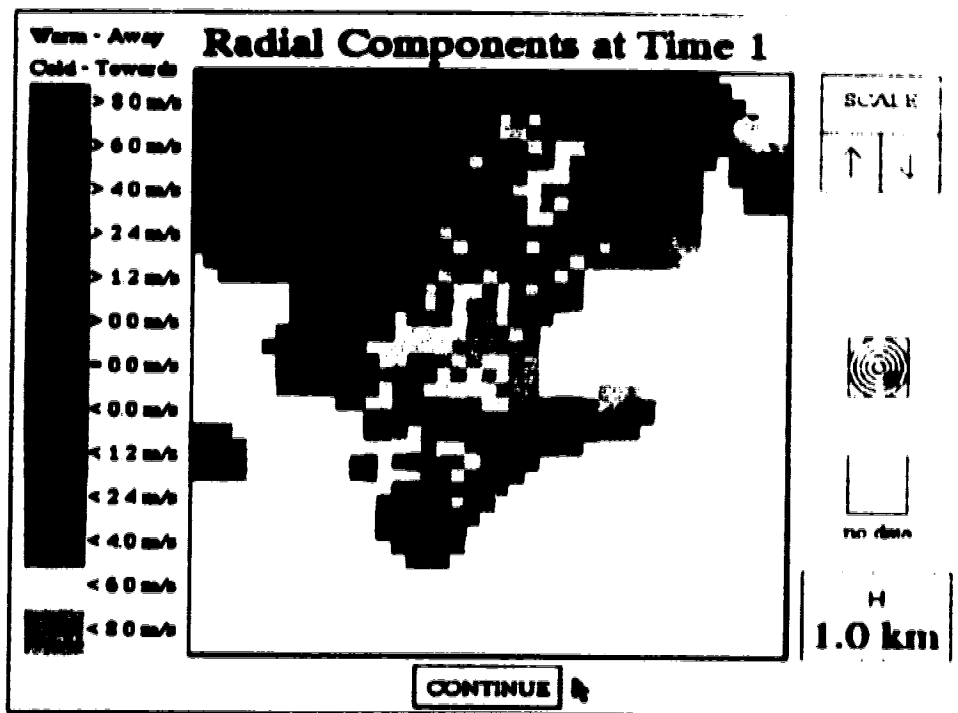


Figure 5.16B 0.5° radial velocity fields for the July 29-30 1993 severe storm (0030Z on the top panel and 0100Z on the bottom panel).

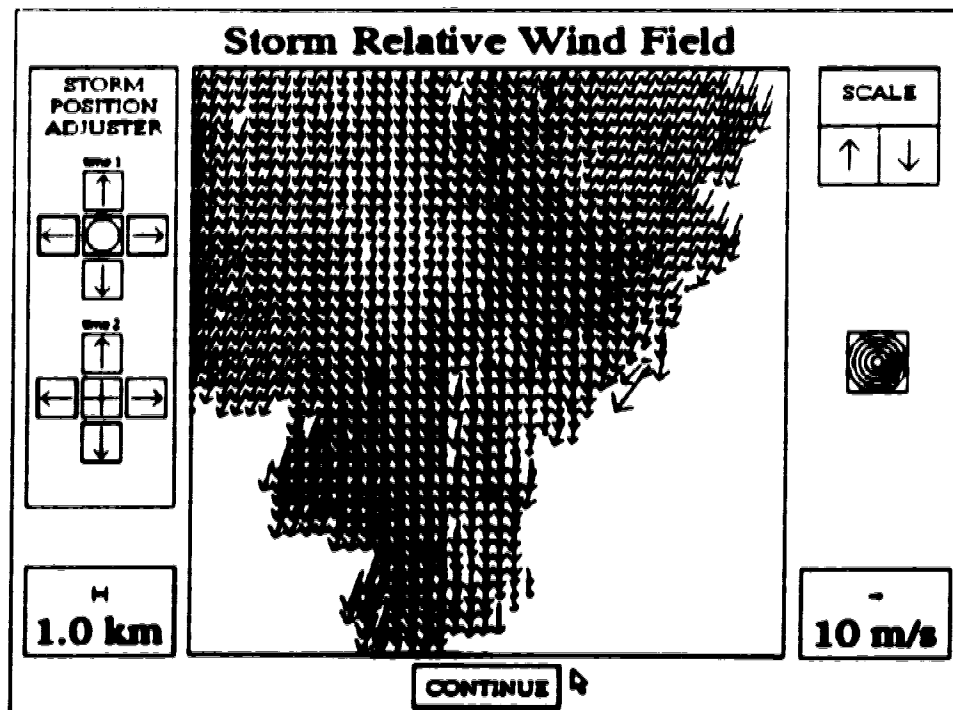
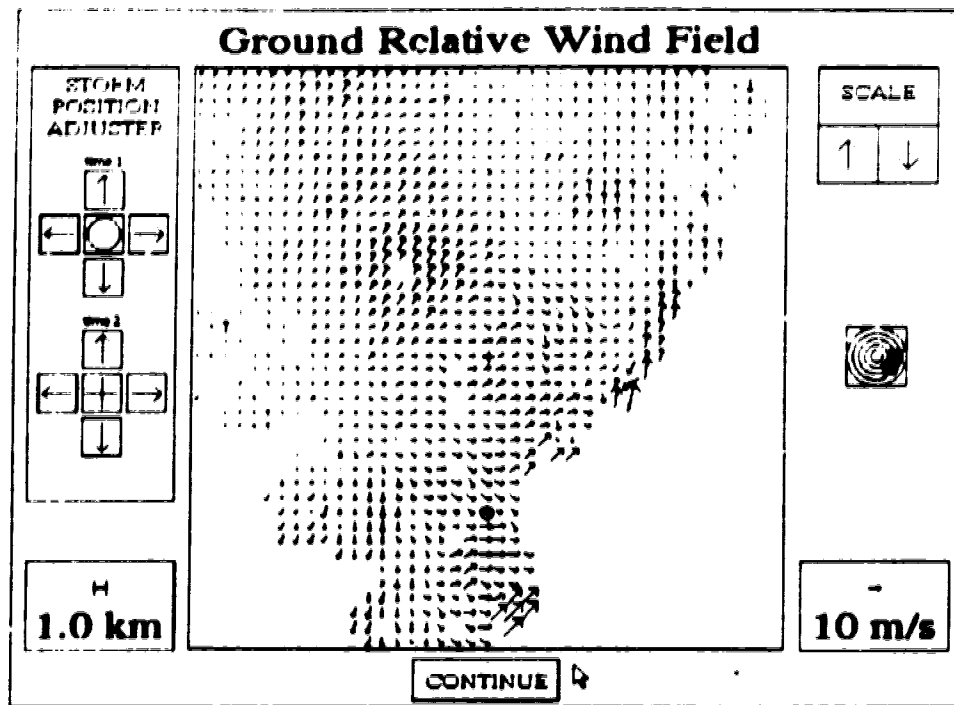


Figure 5.16C SDD wind field reconstructions for the July 29-30 1993 severe storm case based on the 0.5° scans at 0030Z and 0100Z.

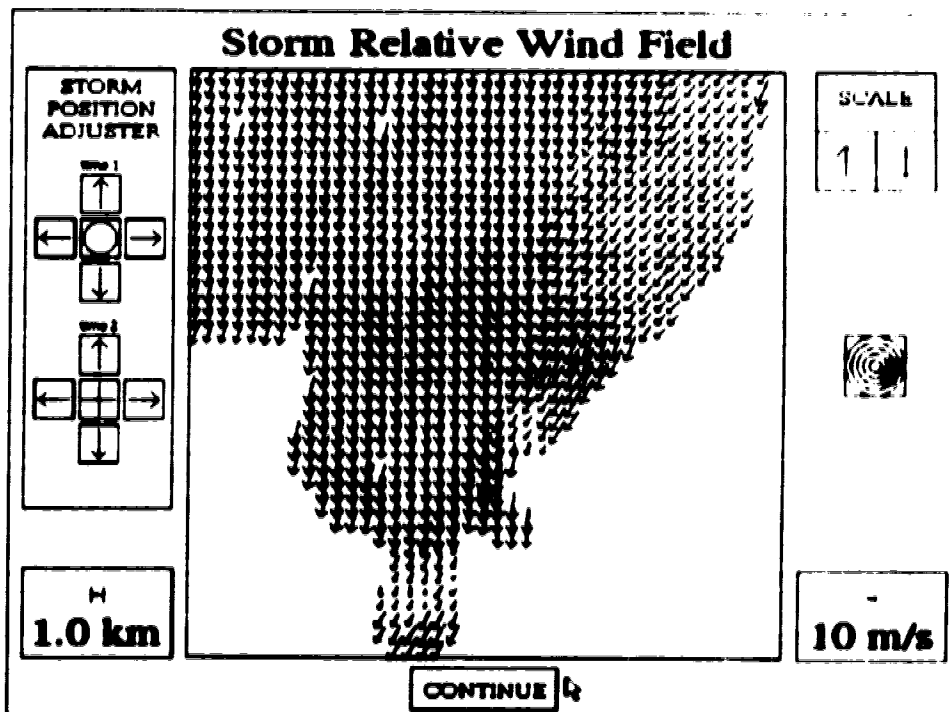
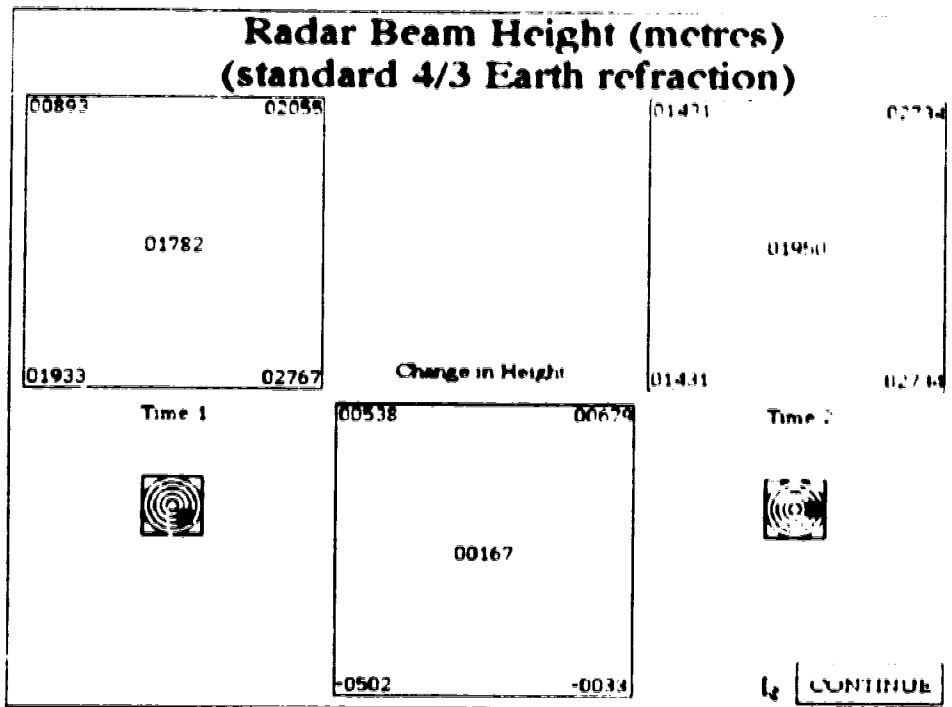


Figure 5.17 SDD analysis results of the July 29-30 1993 severe storm case using the 0030Z and 0100Z 1.5° Doppler scans.

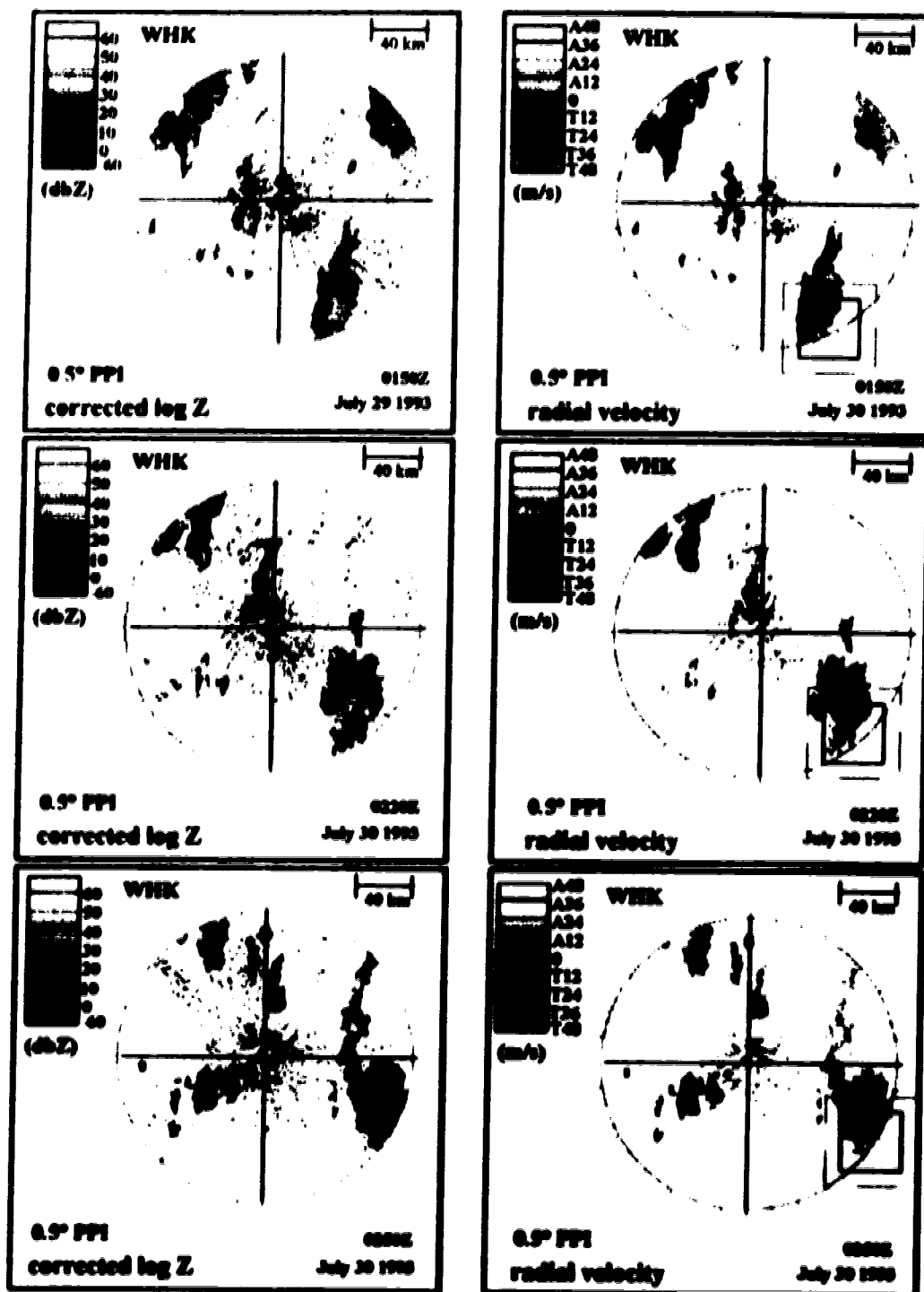


Figure 5.18 The July 30 1993 mesocyclone case with reflectivity and velocity fields at 0150Z, 0220Z and 0250Z. The solid window on the velocity field indicates the areas used for the SDD analysis. The larger window is the area within which the smaller window can be slid to adjust the analysis.

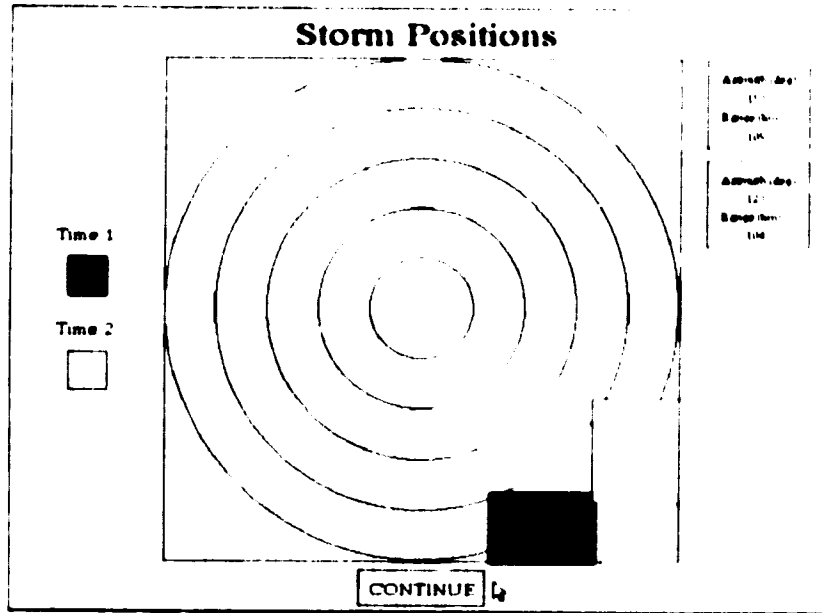


Figure 5.19 Storm positions at 0150Z and 0250Z for the July 30 1993 mesocyclone case. Spacing between rings is 20 km.

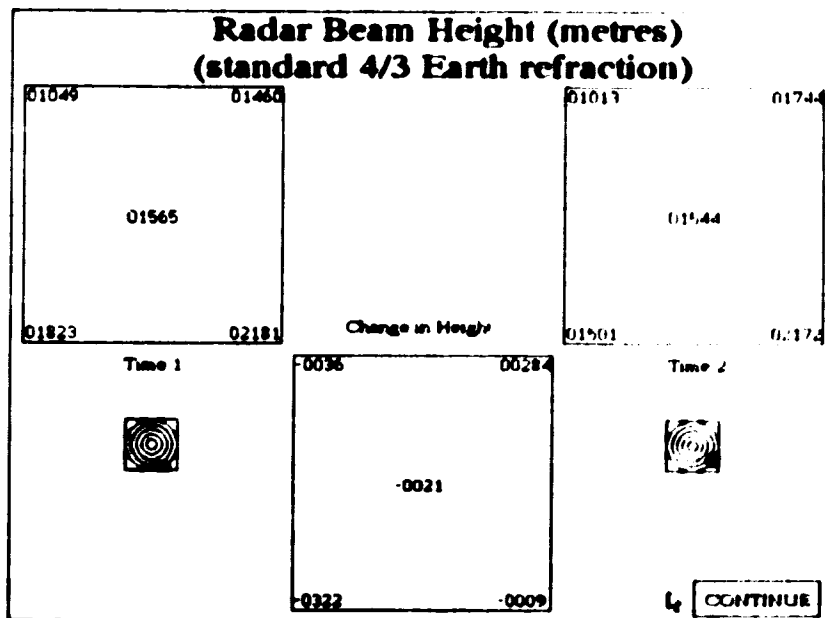


Figure 5.20 Radar beam heights at 0150Z and 0250Z for the July 30 1993 mesocyclone case. Heights for both observations are shown along with the computed change between them.

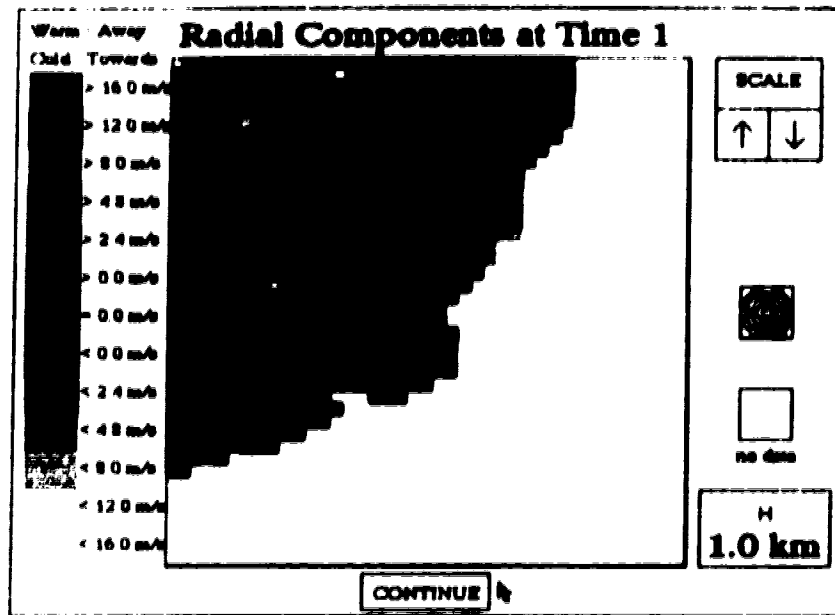


Figure 5.21 0150Z radial wind field for the July 30 1993 mesocyclone case.

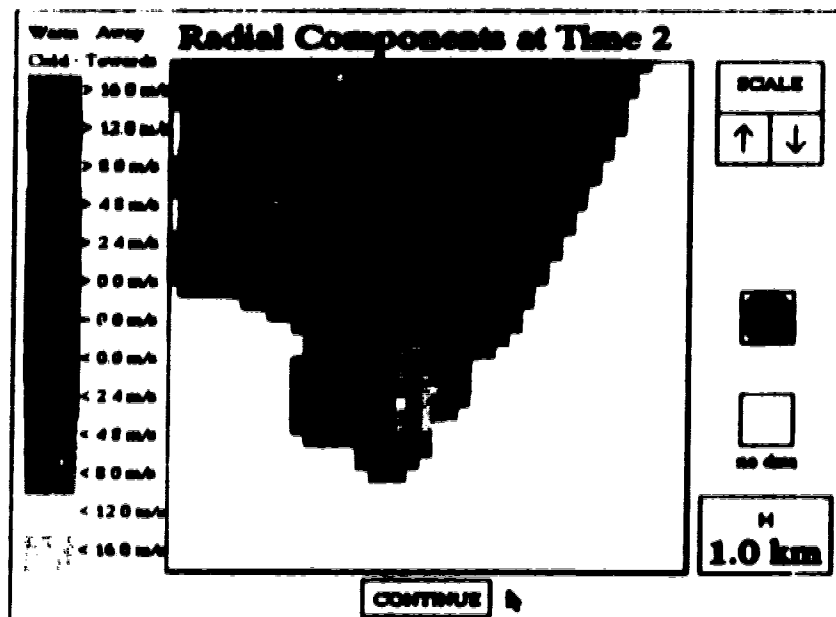


Figure 5.22 0250Z radial wind field for the July 30 1993 mesocyclone case.

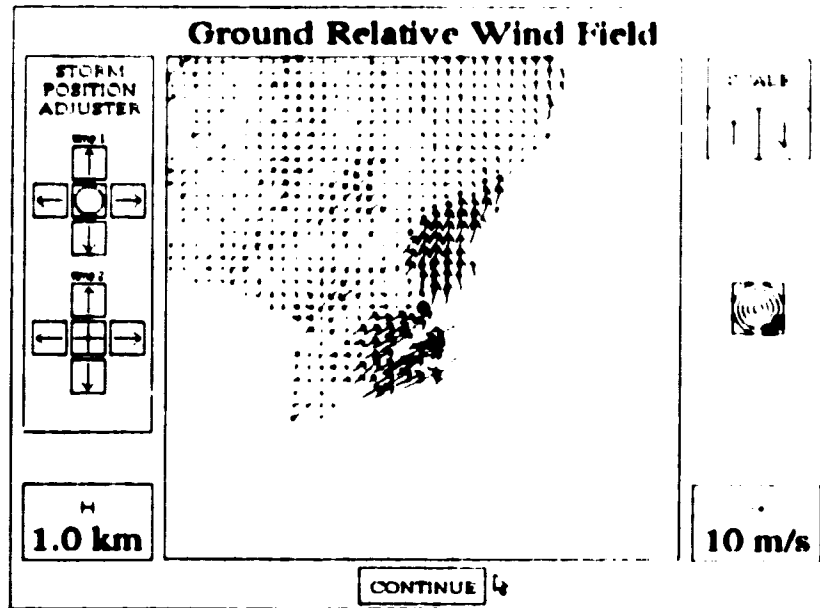


Figure 5.23 Ground relative wind field generated from the 0150Z and 0250Z observations of the July 30 1993 mesocyclone case.

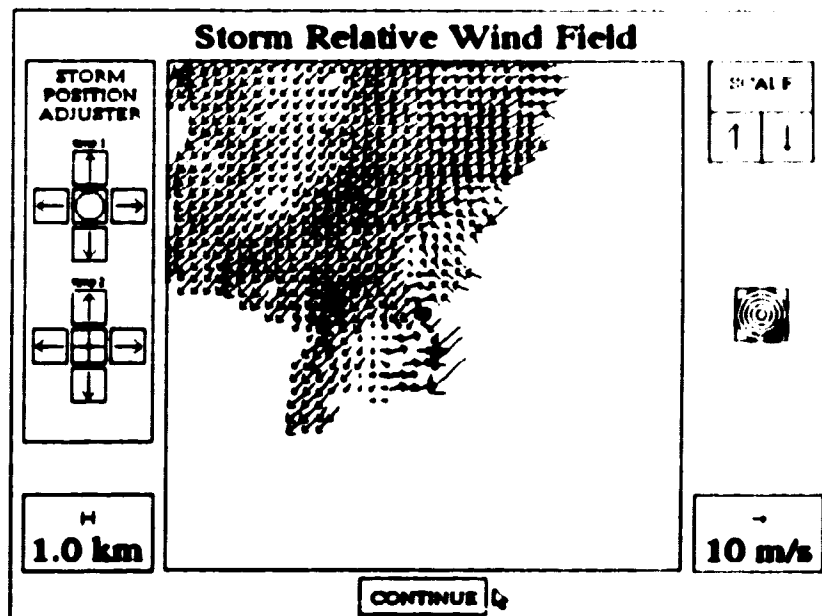


Figure 5.24 Storm relative wind field generated from the 0150Z and 0250Z observations of the July 30 1993 mesocyclone case.

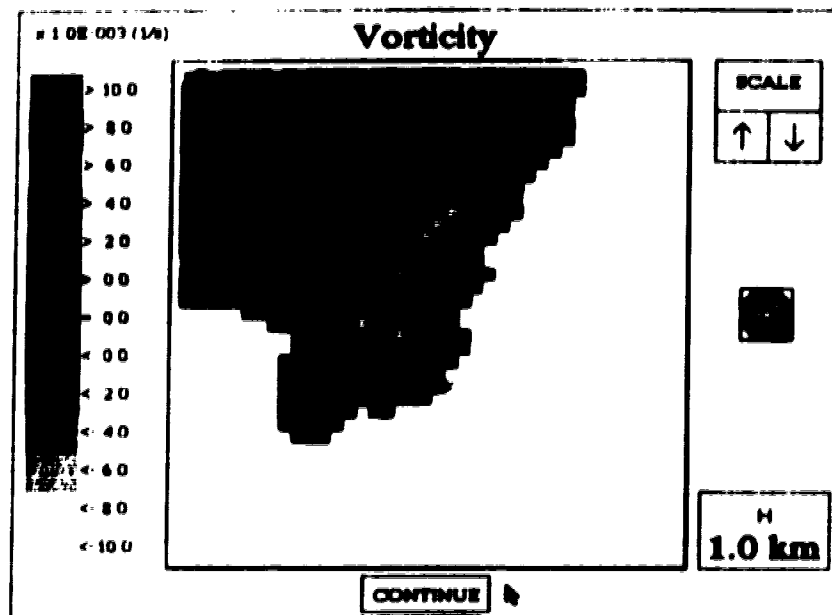


Figure 5.25 Vorticity of the wind field generated from the 0130Z and 0230Z observations on the July 30 1993 mesocyclone. Warm colors indicate cyclonic vorticity.

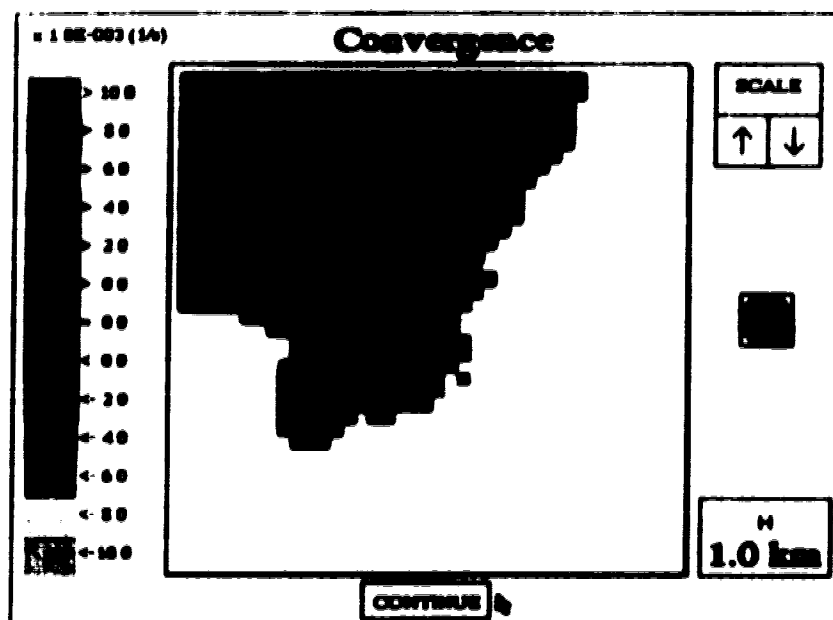


Figure 5.26 Divergence of the wind field generated from the 0130Z and 0230Z observations on the July 30 1993 mesocyclone. Warm colors indicate convergence.

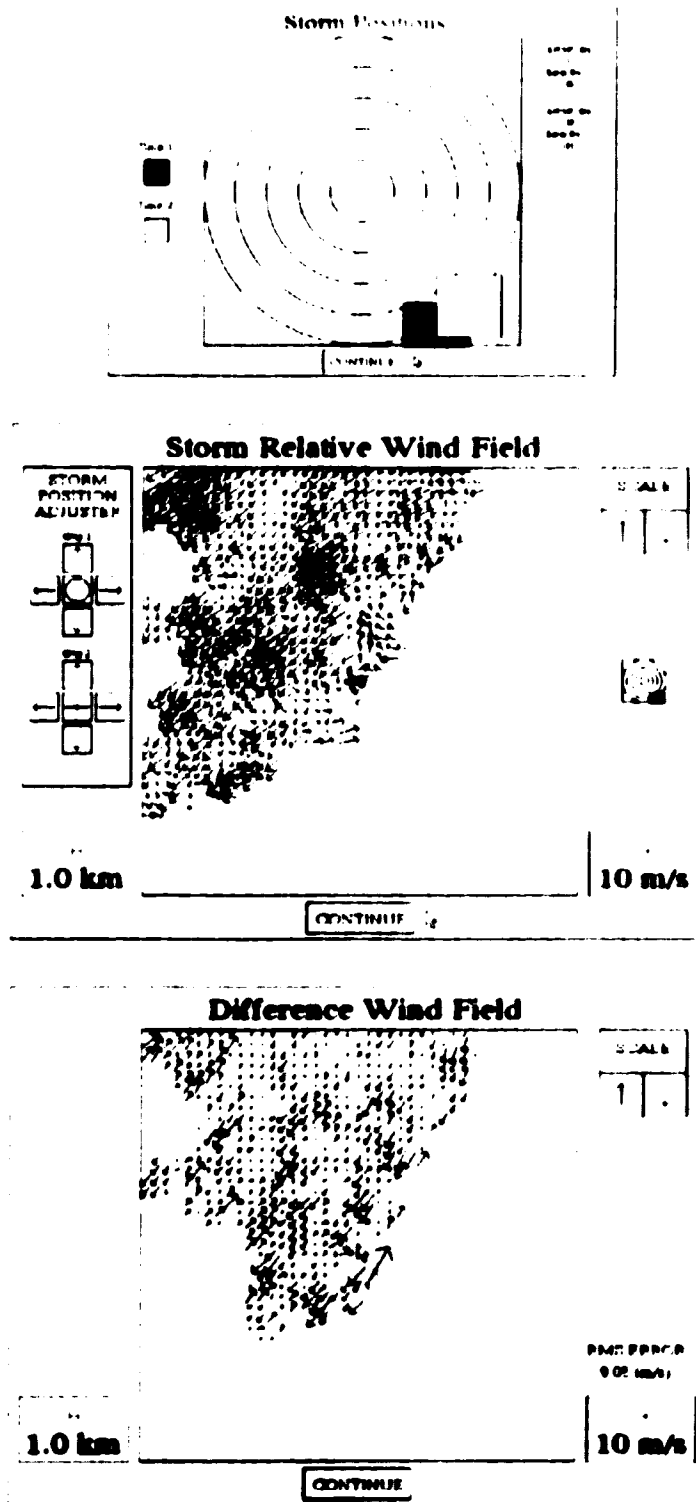


Figure 5.27A SDD analysis of the July 30 1993 mesocyclone case using the 0.5° scans at 0150Z and 0220Z. The bottom panel shows the difference between the wind field and that of the 0150Z-0250Z analysis.

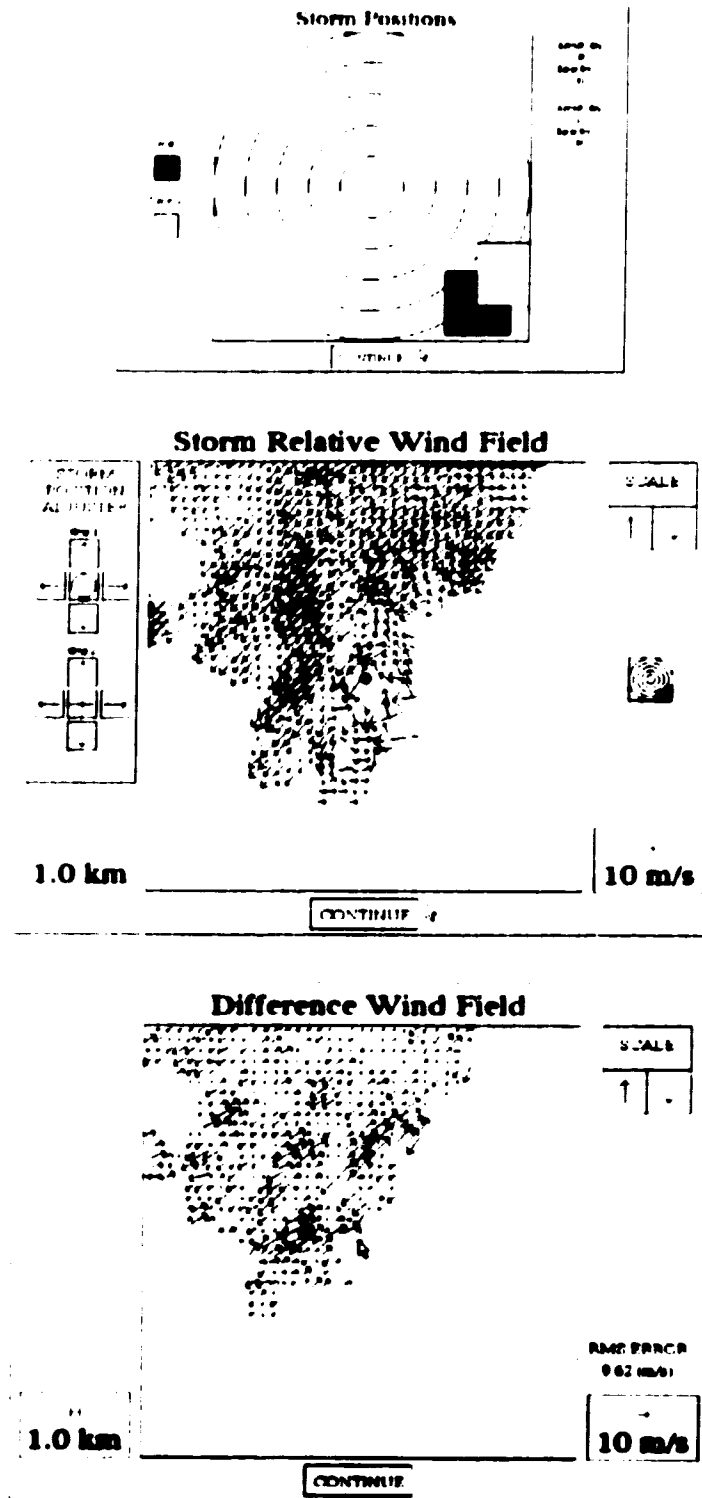


Figure 5.27B SDD analysis of the July 30 1993 mesocyclone case using the 0.5° scans at 0220Z and 0250Z. The bottom panel shows the difference between the wind field and that of the 0150Z-0250Z analysis.

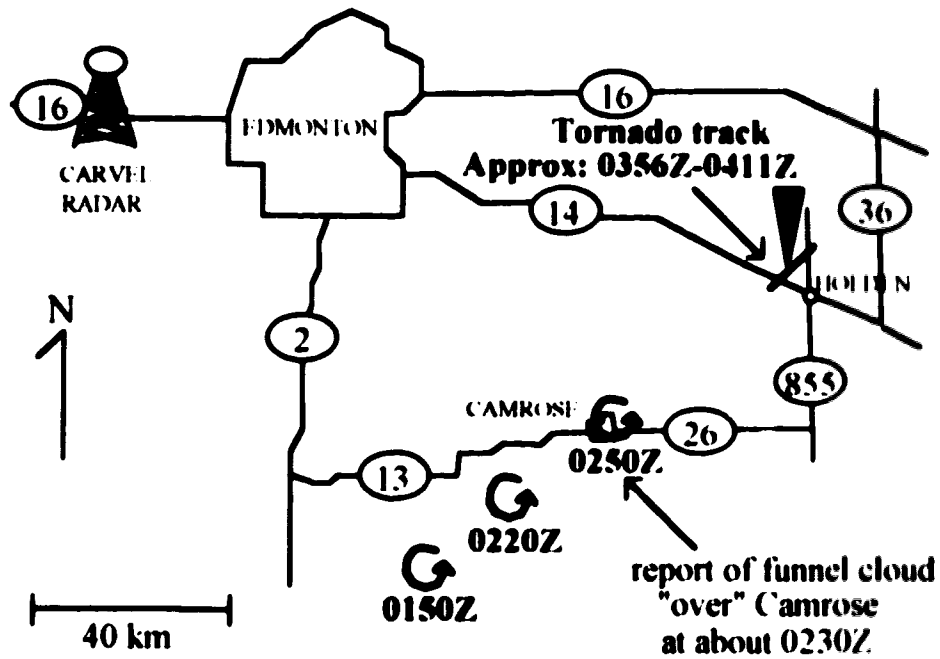


Figure 5.28 The Holden tornado ground truthing compared to the positions of the three wind field sets used for the SDD analyses.

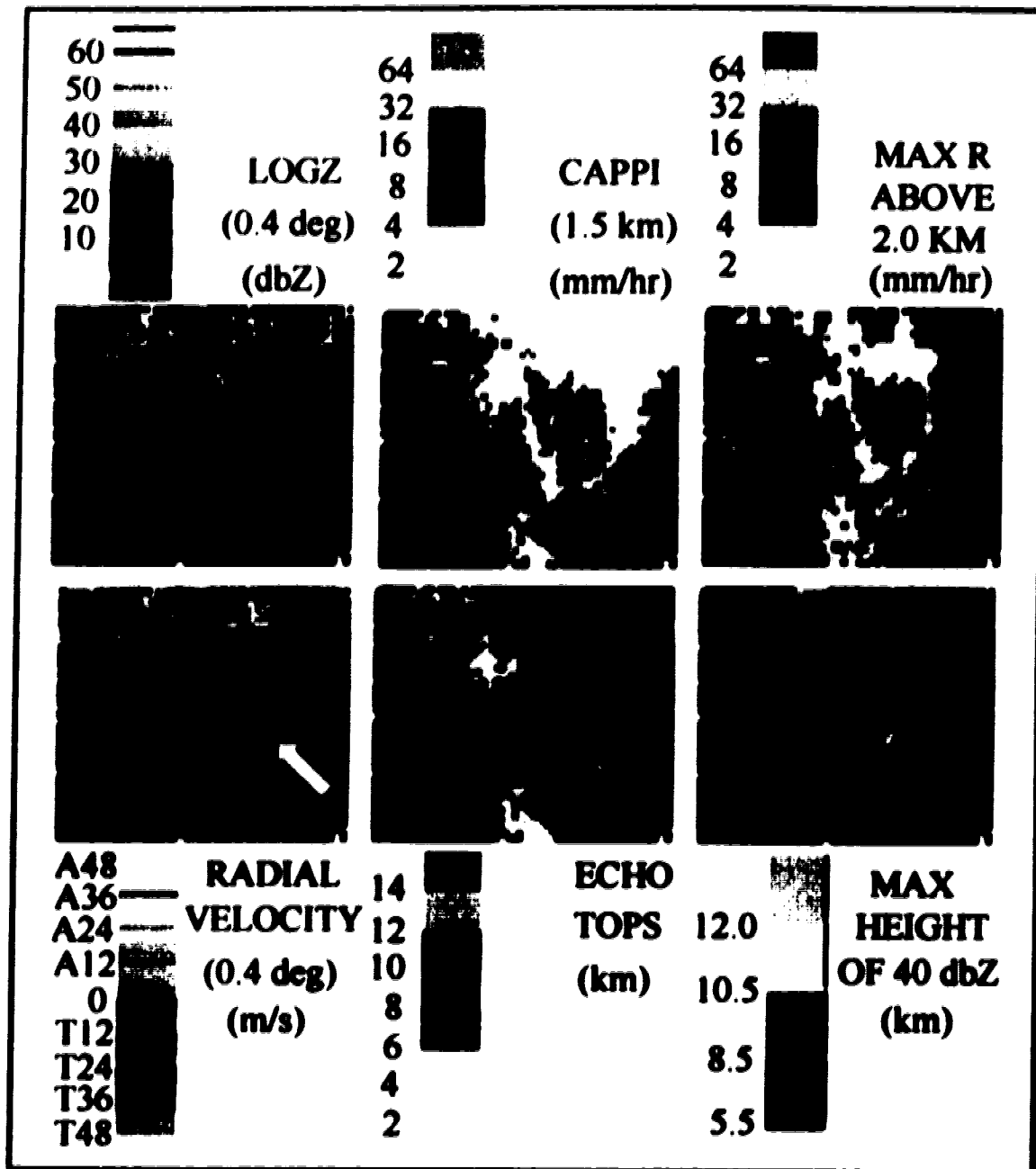


Figure 5.29 The bounded weak echo region (BWER) of the Holden storm is indicated with the arrow on the 0.4° logZ scan. The arrow on the 0.4° velocity scan shows part of the mesocyclone velocity couplet. Other conventional Doppler products show strong reflectivities at high elevations (>10.5 km) in the area of the BWER at low levels.

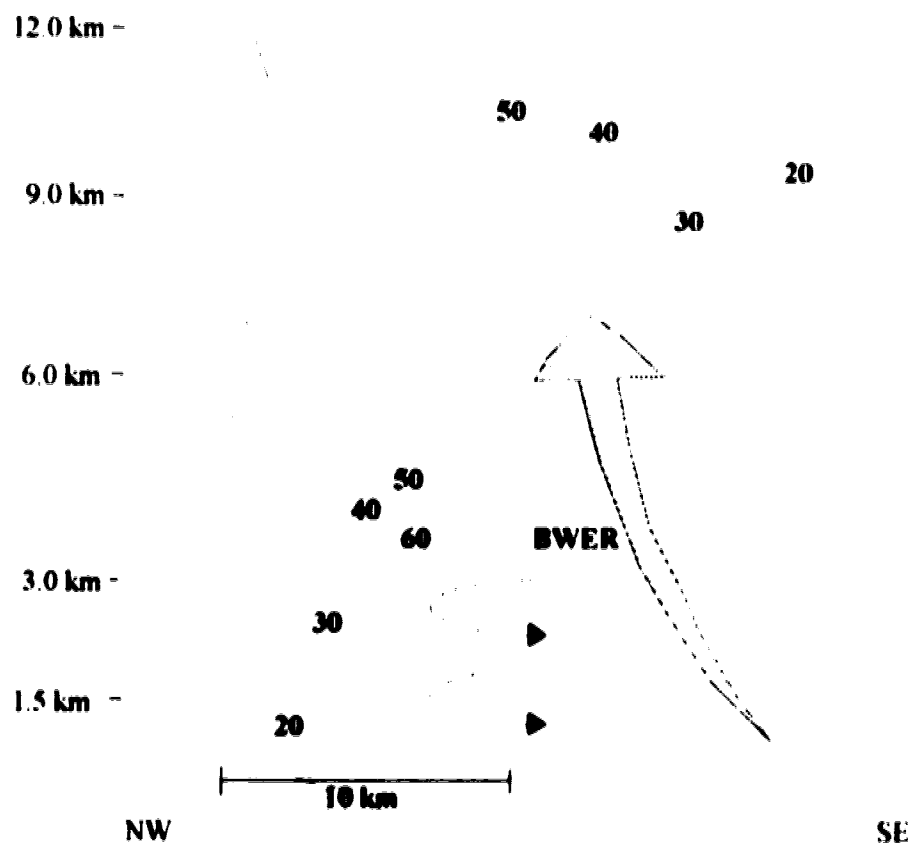


Figure 5.30 *Conceptual cross sectional of the Holden storm (July 30 1993) as seen from the back (SW). Placement of BWER, mesocyclone and reflectivities (in dBZ) based on conventional radar observations and SDD analyses. Conceptual model based on that of Lemon (1980).*

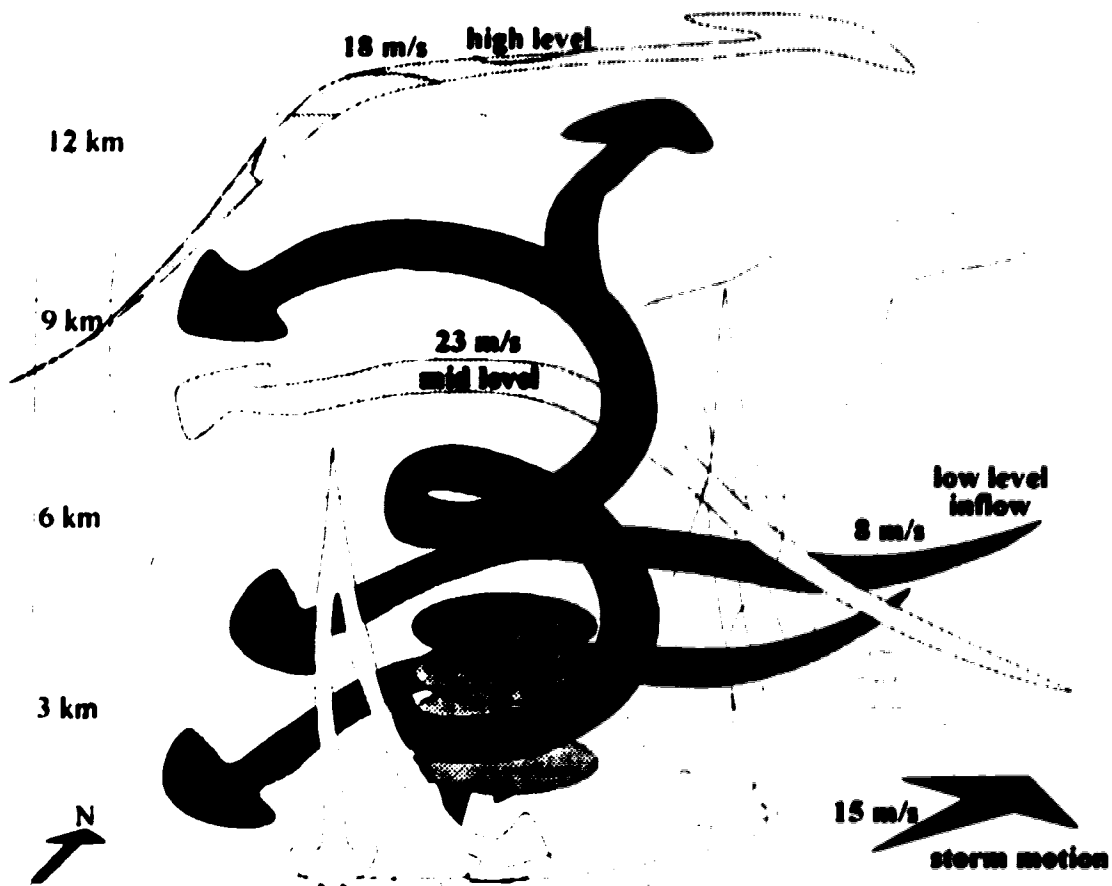


Figure 5.31 Model of the severe storms over central Alberta on July 29 and 30 1993. The storm relative environmental flow shown is based on the WSE upper air sounding of July 30 0000Z. The conceptual model is based on that of Lemon and Doswell (1979).

6. SDD analysis of the "Mississauga storm"

A severe storm developed in southern Ontario during the late afternoon of July 24 1987. Tracking eastward at 50 km/hr, this storm spawned an F1¹ tornado in Mississauga, causing the destruction of a house. The tornado was estimated to have touched down between 2200Z and 2220Z (Joe 1988). A mesocyclone embedded within the storm was detected by the King City Doppler radar (WKR) near Toronto. The storm was within Doppler range for over 2 hours.

An SDD analysis is done on the "Mississauga storm". The results are compared with calculations from an automatic mesocyclone detection algorithm which was developed for the King City radar.

6.1. Synthesized horizontal wind field at low levels

Figures 6.1A-B show the reflectivity and radial velocity scans (0.7°) from 2200Z to 2240Z. Radial component observations from 2200Z and 2220Z were used for the low level (0.7° elevation) analysis. The average beam height is about 600 m. Differences in beam heights between the observations are less than 200 m (Figure 6.2A).

The wind field derived from the SDD analysis is shown in Figure 6.2B. The storm relative depiction shows a mesocyclone with a radius of about 2 km within a larger partial vortex with a radius of about 8 km. The ground relative wind field shows a strong flow in the southern quadrants of the larger vortex due to the addition of the storm relative flow to the advection of the storm. The storm relative wind field shows some asymmetry which is probably a result of an evolving wind field, as described in section 4.4.

The vorticity associated with the mesocyclone, as calculated from the synthesized wind field, has a value of about $8 \times 10^{-3} \text{ s}^{-1}$, while the larger vortex has an overall vorticity value of 2 or $3 \times 10^{-3} \text{ s}^{-1}$ (Figure 6.3). The computed mesocyclone vorticity can be compared with results from an automatic mesocyclone detection algorithm developed at the King City radar research facility. The "effective" radius² of the mesocyclone decreased from 2.2 km (2200Z) to 1.3 km (2210Z). The vortex then expanded to reach an effective radius of 2.3 km at 2220Z (Joe 1988). The average velocity difference across the feature

¹On the Fujita scale, an F1 has wind speeds of 73-112 mph and causes moderate damage (Fujita 1973).

²This is an average of a momentum weighted average and a RMS average.

was 11.6 m/s (2200Z), 7.0 m/s (2210Z) and 9.3 m/s (2220Z). Assuming a non-divergent solid body rotation within the mesocyclone, these numbers give vorticity values of $5.3 \times 10^{-3} \text{ s}^{-1}$ (2200Z), $5.4 \times 10^{-3} \text{ s}^{-1}$ (2210Z) and $4.0 \times 10^{-3} \text{ s}^{-1}$ (2220Z). The higher vorticity value obtained from the SDD technique ($8 \times 10^{-3} \text{ s}^{-1}$) may be a result of the positive speed bias discussed in section 4.8.

Based on the SDD analysis, the convergence in the area of the mesocyclone is about $8 \times 10^{-3} \text{ s}^{-1}$ (Figure 6.3). The convergence field over the remaining area is quite noisy. The Doppler velocity images (Figure 6.1) confirm that the mesocyclone was converging during the 2200-2220Z period since the axis of the velocity couplet was rotated clockwise with respect to the viewing angle of the radar³. This is particularly true at 2200Z and 2220Z, but less so at 2210Z.

Since convergence into the mesocyclone causes a "spin-up" due to conservation of angular momentum, it is likely that significant changes occurred in the wind field between 2200-2220Z. Using a convergence value of $8 \times 10^{-3} \text{ s}^{-1}$, simple calculations show that the mesocyclone will reduce its radius by half about every 3 minutes (Appendix E). One could argue that this strong convergence led to the tornado between 2200-2220Z and that the mesocyclone observed after 2220Z was in fact a new mesocyclone resulting from the convergence of the larger vortex. However, both the SDD and mesocyclone detection algorithm results are quite limited for this type of calculation. Consequently, these interpretations are only speculative.

6.2. Test of the quasi-steady assumption

The steadiness of the wind field was tested by comparing the 2200Z-2220Z analysis (run A) results with an SDD analysis based on the 2210Z-2230Z (run B) observations (Figure 6.4A). The mesocyclone visible in the B analysis is qualitatively similar to that from run A. The large vortex seen in the A analysis is also apparent on the B run, but appears to have quite a few distortions. The wind fields differ most in the northeast section, where the A run shows a strong easterly flow but the B analysis gives a moderate southwesterly flow. This difference also accounts for most of the mean flow speed difference between the two analyses (11.53 m/s for A, 8.30 m/s for B). Based on these comparisons, it can be concluded that the wind field was fairly steady from 2200Z to 2230Z except in the northeast section of the areas analyzed.

³A simulation of this effect is shown in Figure 4.4B.

Further tests on the quasi-steady assumption were made by doing SDD analyses using the 2210Z-2240Z (run C) and 2200Z-2240Z (run D) observations. The resulting wind fields (Figure 6.4B) are *qualitatively* comparable, but quite different from those of runs A and B. As outlined in Figure 6.4C, this suggests that using the 2240Z observation for the SDD analysis results in a perturbation of the synthesized wind field. This, in turn, may mean that the wind field underwent important evolution between 2230Z and 2240Z.

6.3. Horizontal wind fields at higher levels

The Doppler scans at 1.5° and 3.5° were used to examine the storm flow at higher levels. Beam heights for the 1.5° scan average about 1200 m while average heights on the 3.5° scan are near 2700 m (Figure 6.5A). Changes in beam height are less than 400 m in the lower scan, but up to 800 m in the highest scan. This implies that vertical wind shear may cause large errors in the synthesized wind field, particularly for the 3.5° scan.

Synthesized wind fields for the mean levels of 1200 m (1.5°) and 2700 m (3.5°) are shown in Figure 6.5B. Although a partial velocity couplet appears on the 1.5° and 3.5° Doppler imagery (not shown), neither the mesocyclone nor the larger vortex synthesized with the 0.7° scan are apparent in the upper analyses. Strong shear does, however, appear on both the 1.5° and 3.5° synthesized wind fields in the area of the lower level mesocyclone. It is most likely, then, that the mesocyclone existed at these levels but was evolving rapidly and therefore cannot be resolved using the SDD technique.

Although the flow at 2700 m is stronger than that at 1200 m, strong similarities exist between the wind fields. The strong southerly flow over the southeast sections is probably the warm moist inflow into the storm.

6.4. Concluding remarks

This case illustrates how the evolution of a wind field can hinder an SDD analysis even under otherwise ideal SDD conditions (i.e. a fast moving storm, mostly azimuthal motion, high resolution due to close range). As discussed in Chapters 2 and 4, the effect of an evolving wind field can be minimized by using relatively short times between the Doppler observations used in the analysis. This storm makes it clear that it is also very important that the two observations used do not come from different "stages" in its lifetime. For example, a 20 minutes analysis may violate the quasi-steady requirement more than a 40 minute analysis if it happens to cross a transition boundary.

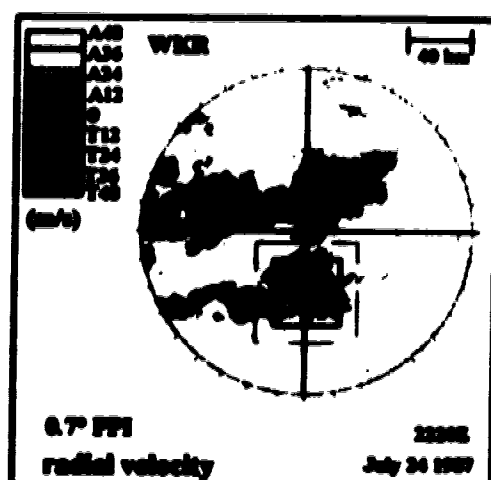
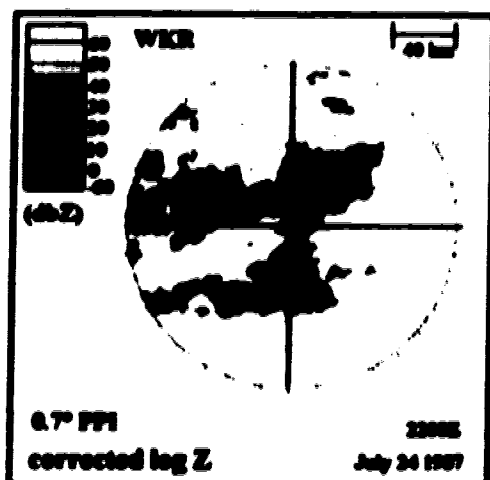
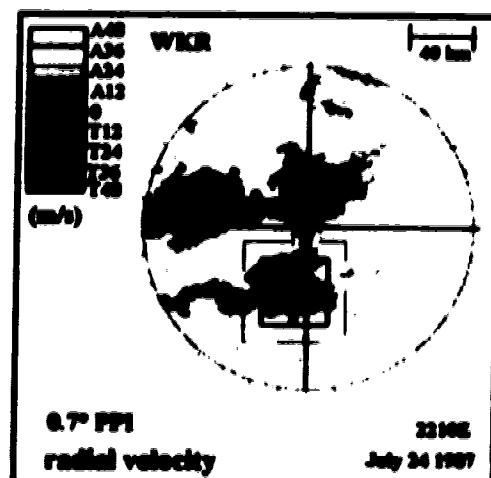
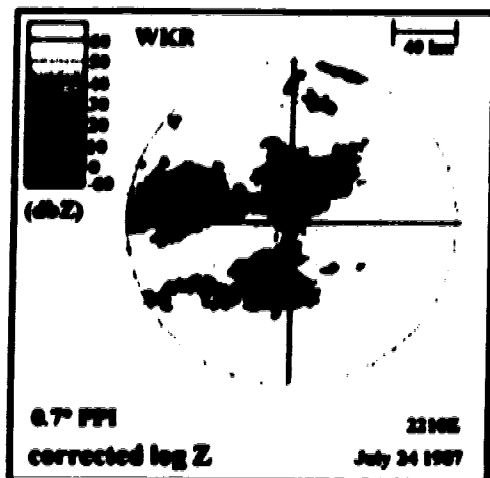
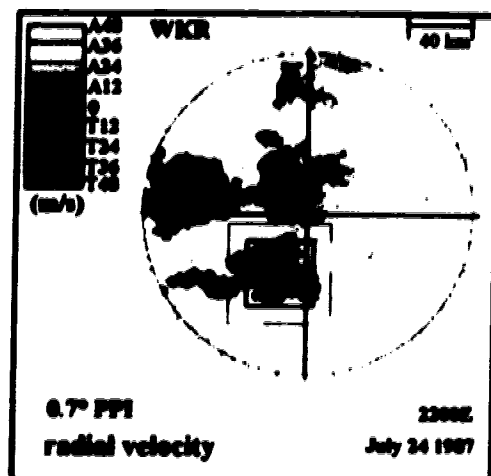
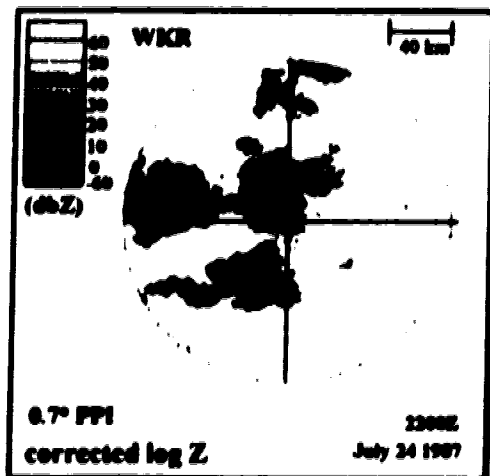


Figure 6.1A The July 24 1987 Minisinks tornadoic storm case. Reflectivity and velocity observations for 2200Z, 2210Z and 2220Z.

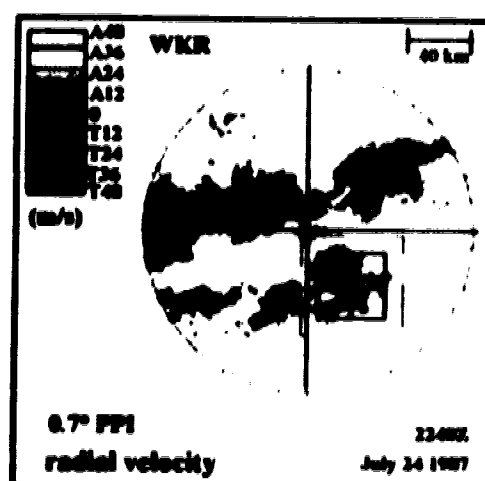
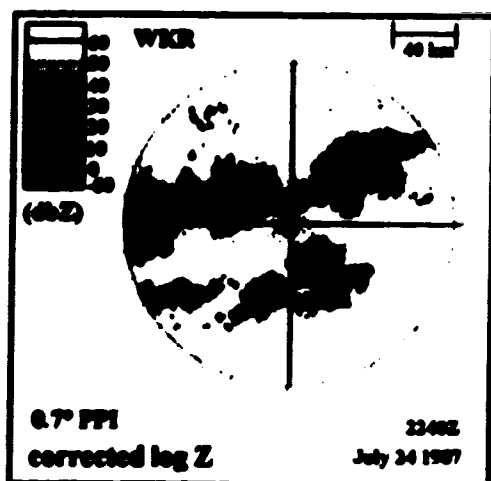
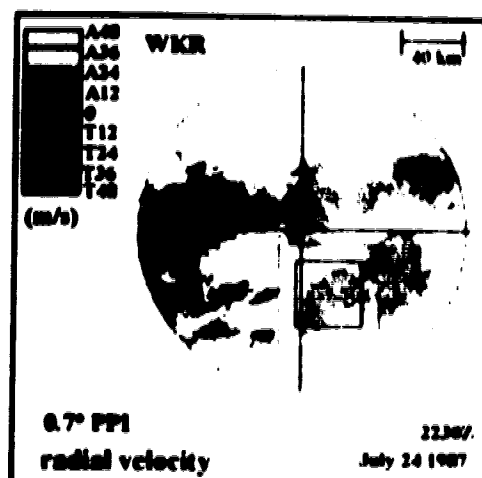
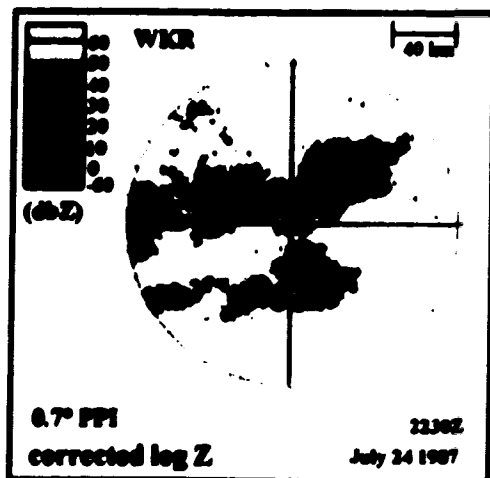


Figure 6.1B The July 24 1987 Mississauga tornadic storm case. Reflectivity and velocity observations for 2230Z and 2240Z.

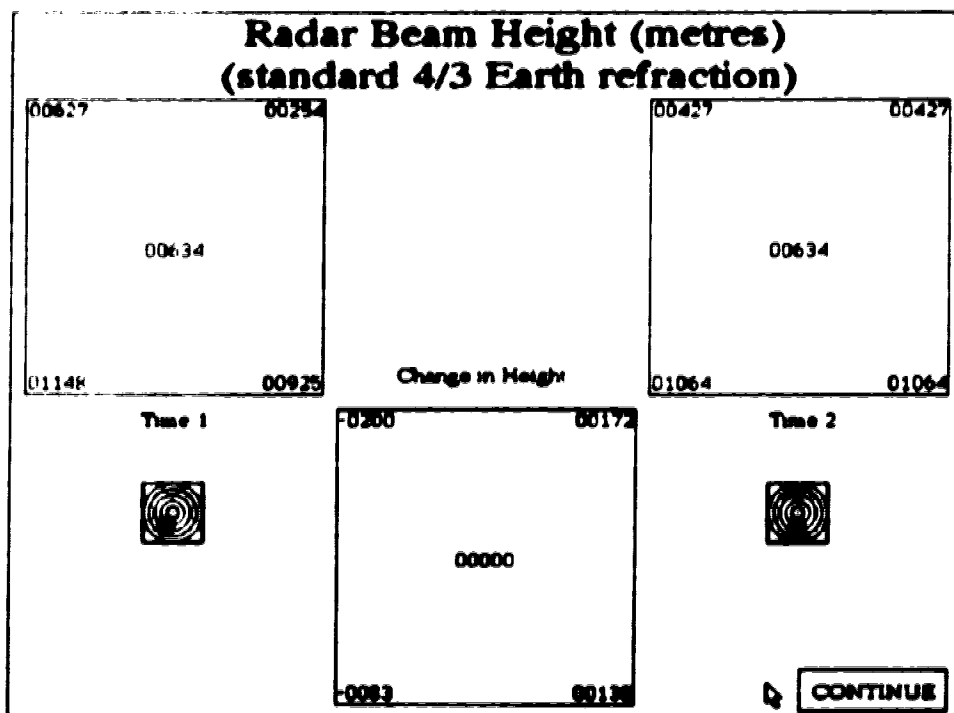
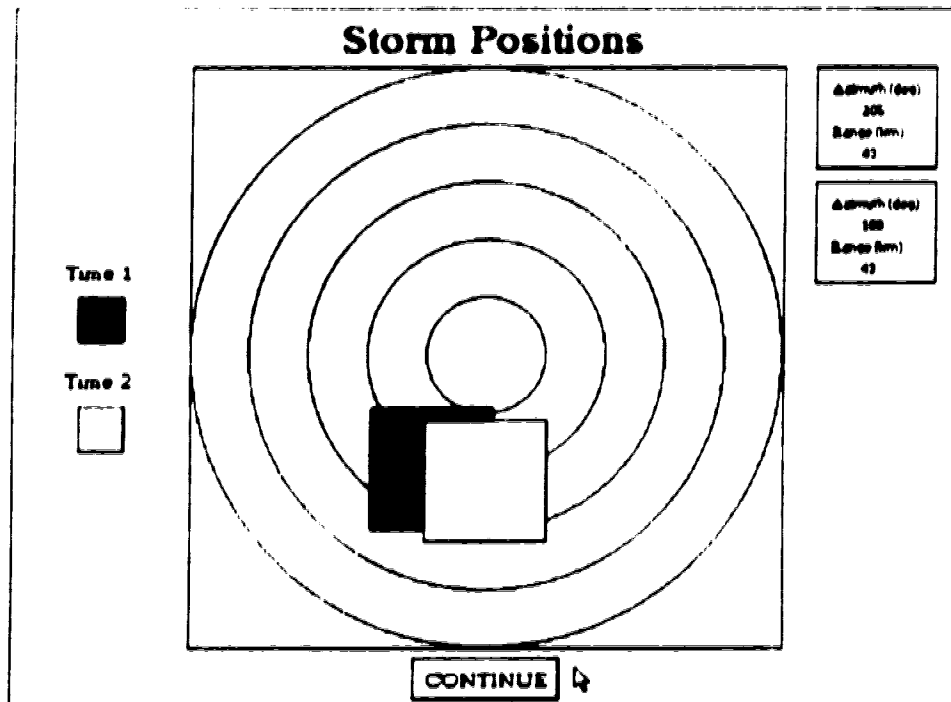


Figure 6.2A Storm positions and beam heights for the 2200Z-2220Z 0.7° analysis of the Mississauga storm.

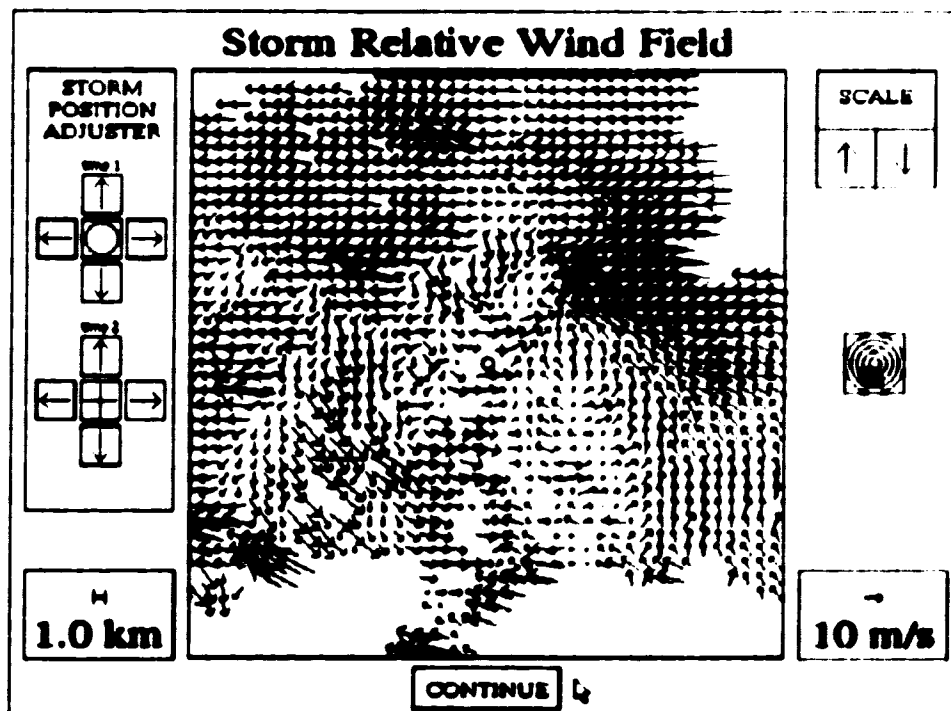
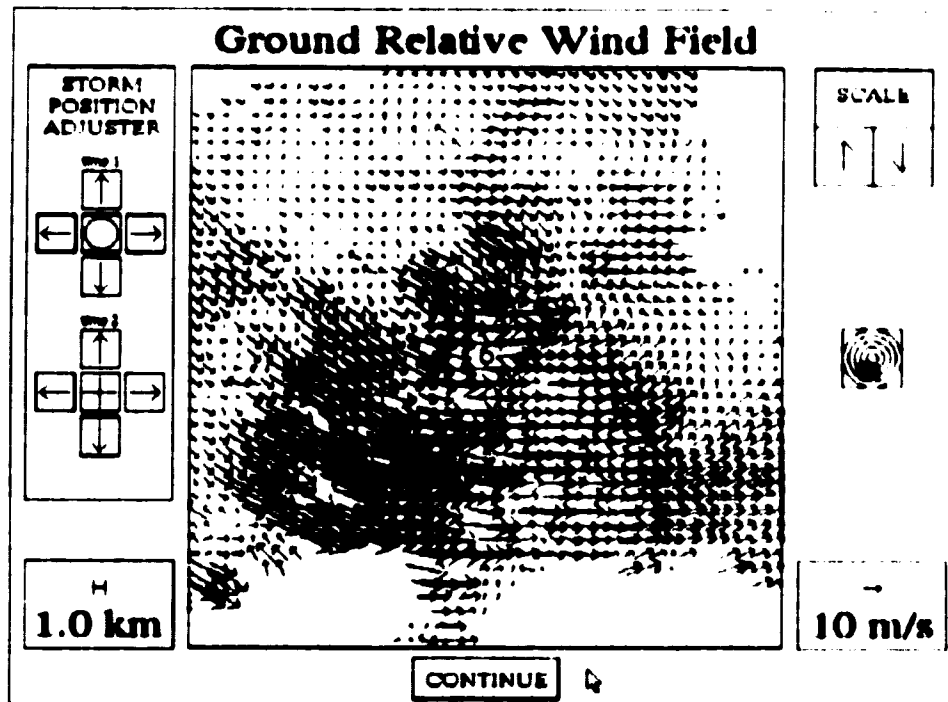


Figure 6.2B Storm and ground relative wind fields from the 2200Z-2220Z 0.7° analysis of the Mississauga storm.

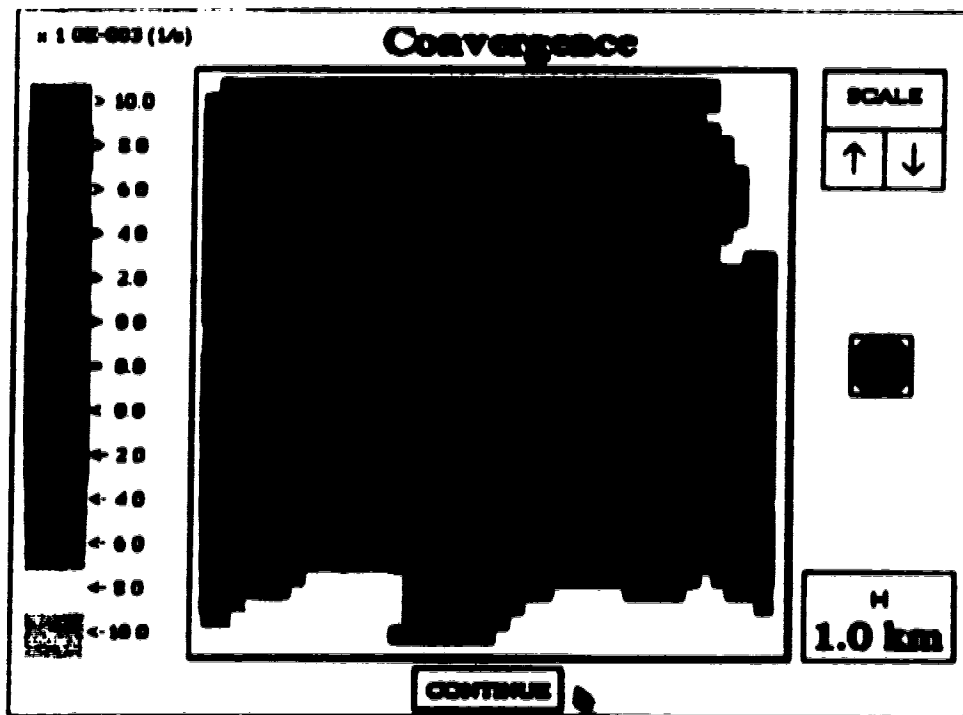
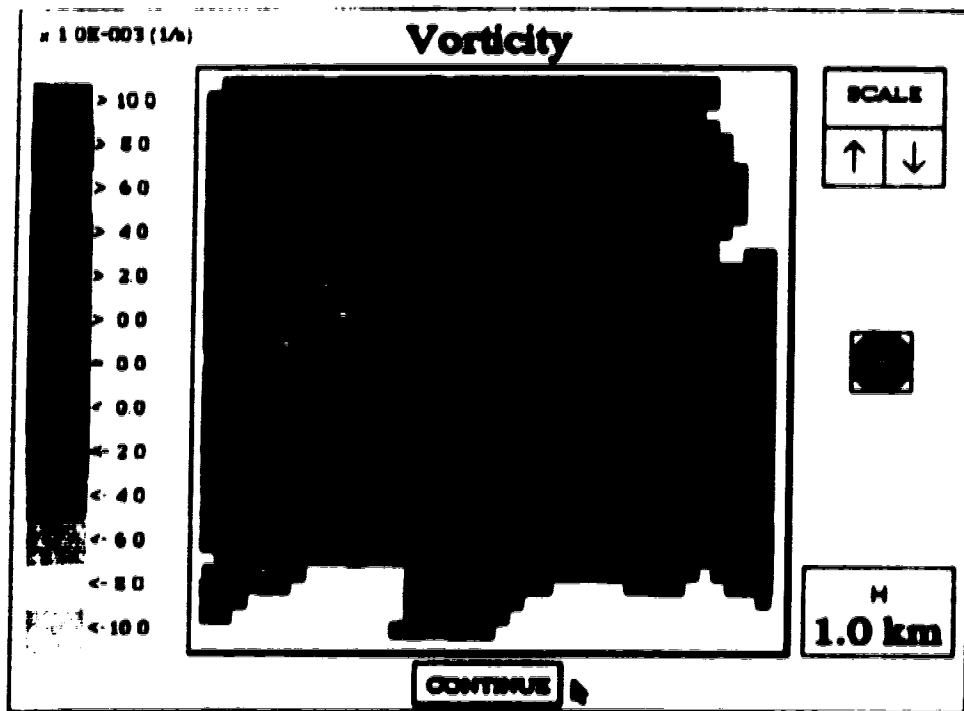


Figure 6.3 Vorticity and convergence fields from the the 0.7° analysis of the Mississauga storm (2200Z-2230Z).

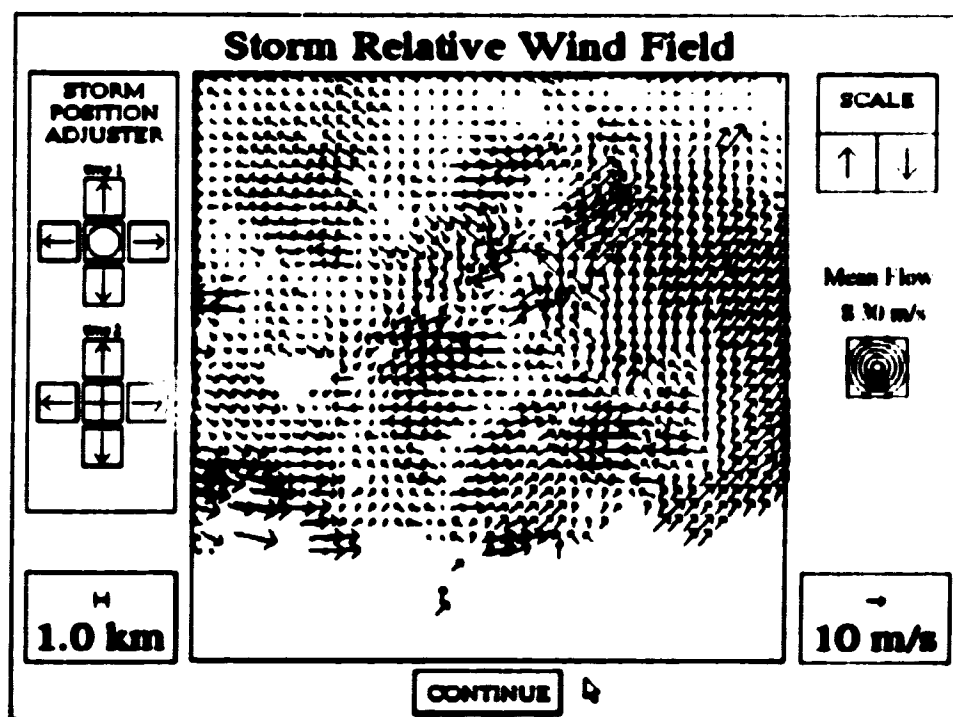
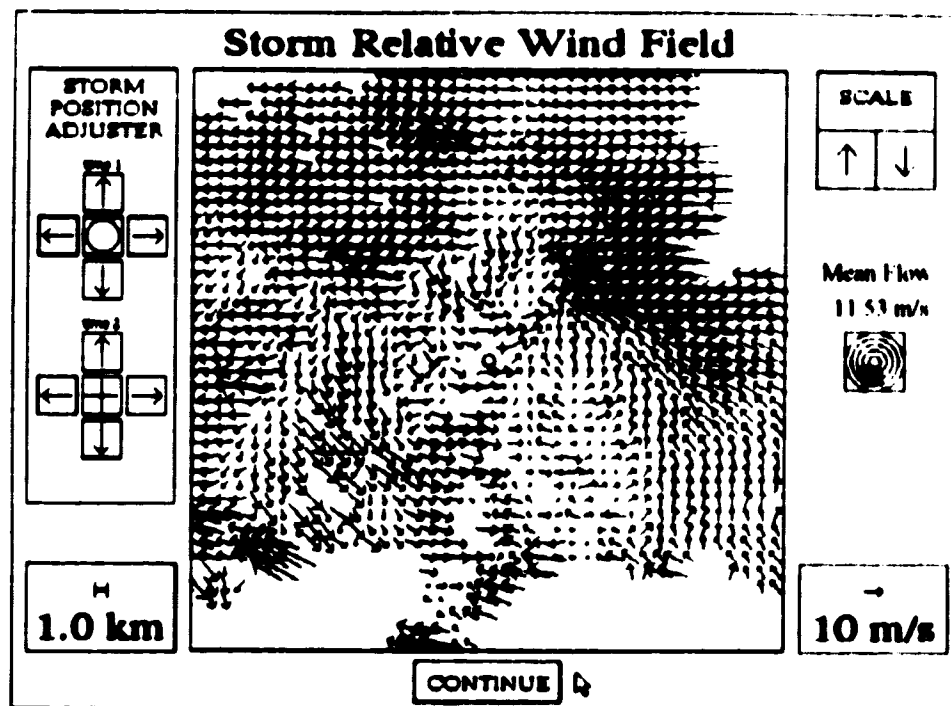


Figure 6.4A Storm relative wind fields for the 0.7° analysis of the Mississauga storm. Top panel shows the 2200Z-2220Z analysis (run A), bottom panel shows the 2210Z-2230Z analysis (run B). The RMS error between the two fields is 16.0 m/s.

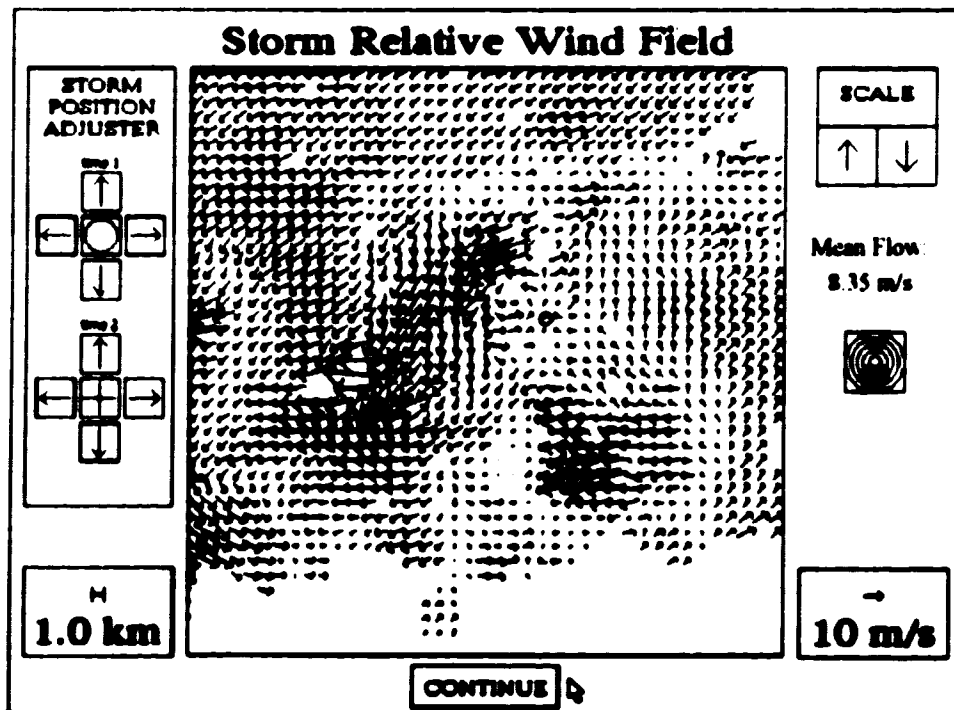
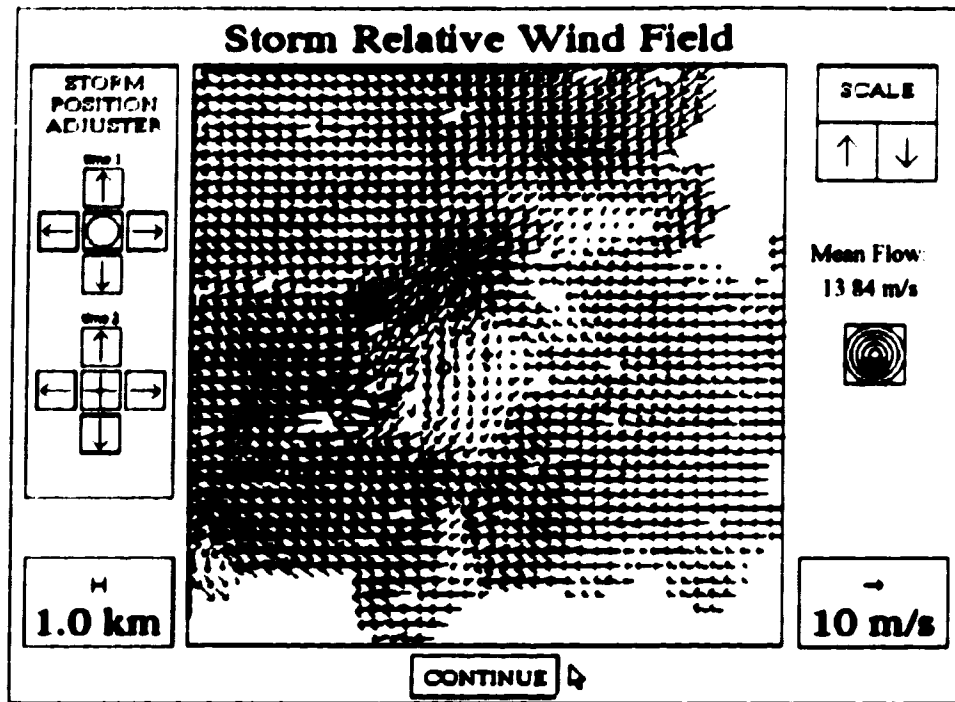


Figure 6.4B Same as Figure 6.4A but using the 2200Z-2240Z (run D) observations (top panel) and the 2210Z-2240Z (run C) observations (bottom panel). The RMS error between the two fields is 12.4 m s.

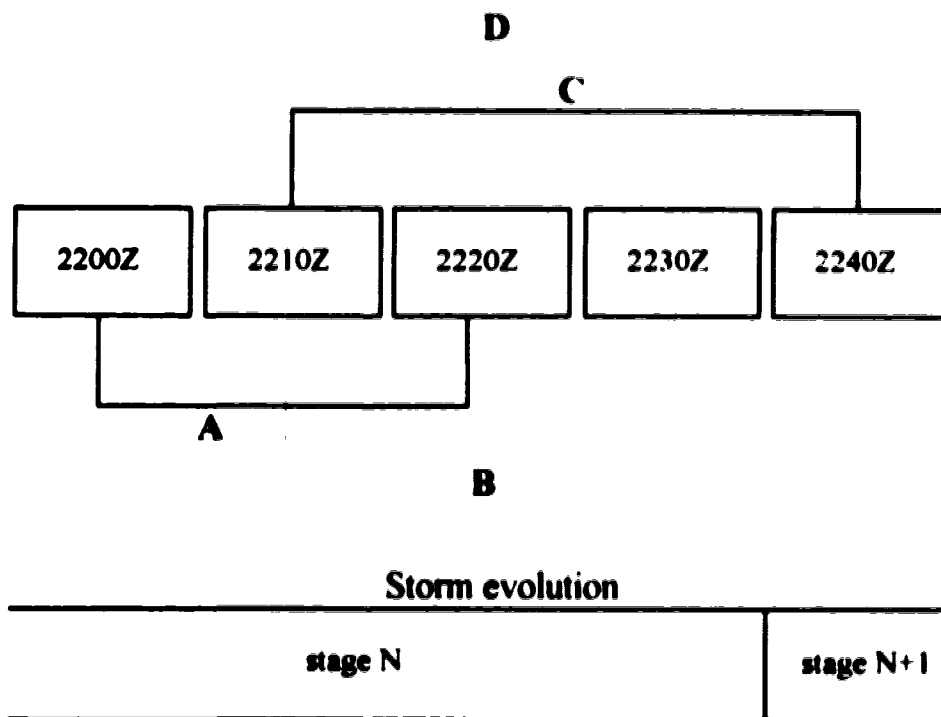


Figure 6.4C Schematic of Doppler observations used in SDD analyses of the Mississauga storm. Results from A and B are comparable suggesting that the wind field was steady between 2200Z and 2230Z. Results from C and D are also comparable but significantly different from those of A and B. It is likely that the wind field underwent important modifications by 2240Z since use of data at that time significantly perturbs the resulting SDD analysis.

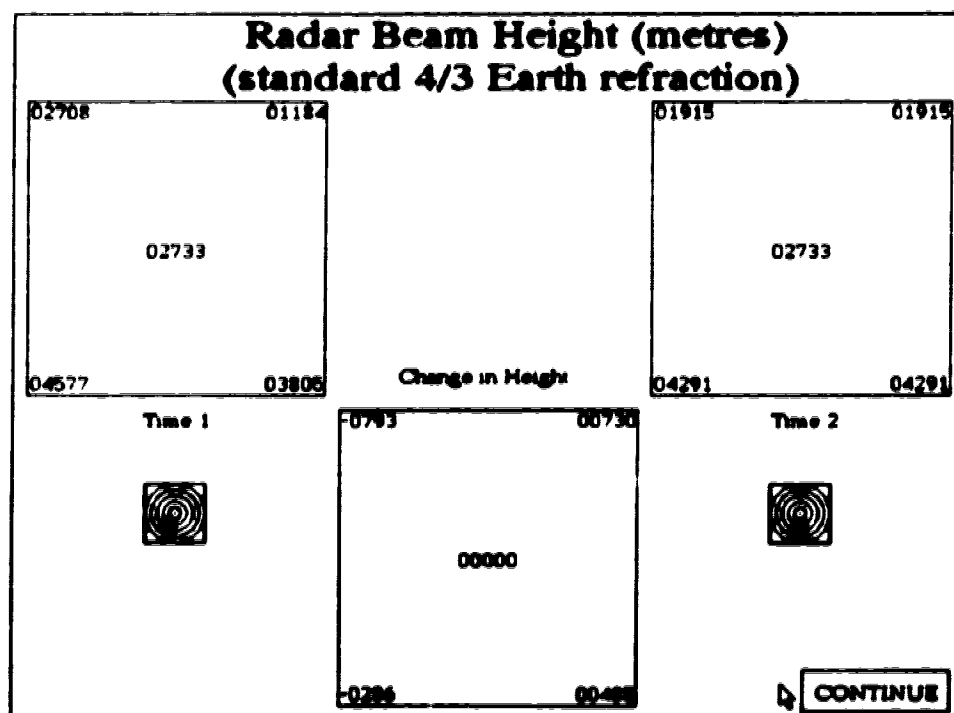
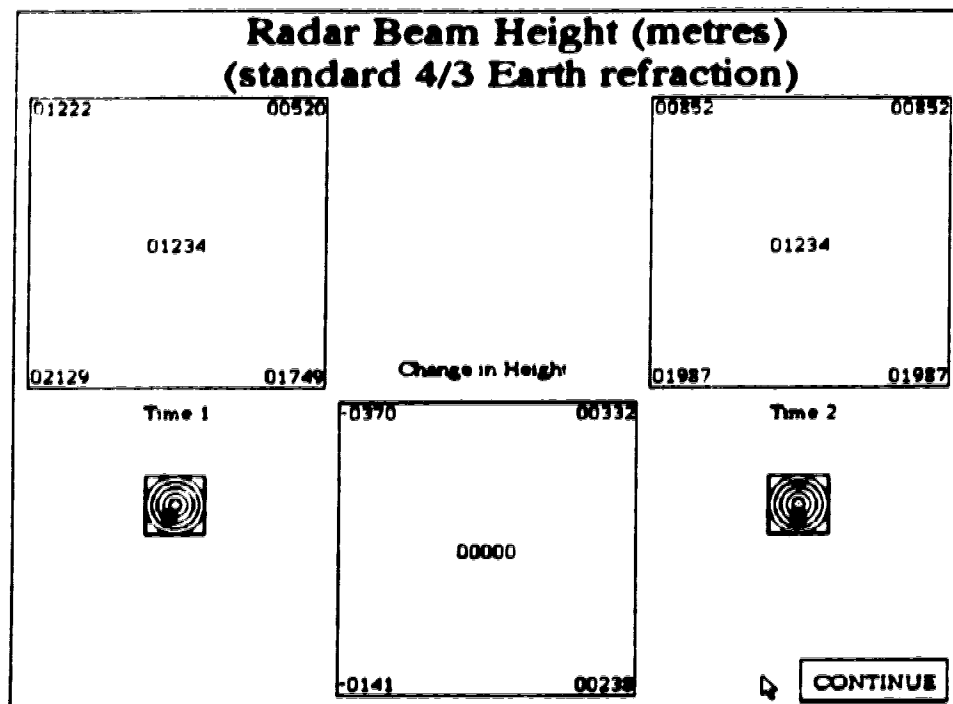


Figure 6.5A Beam heights for the 1.5° and 3.5° analysis of the Mississauga storm (2200Z-2220Z). The storm positions are the same as in Figure 6.2A.

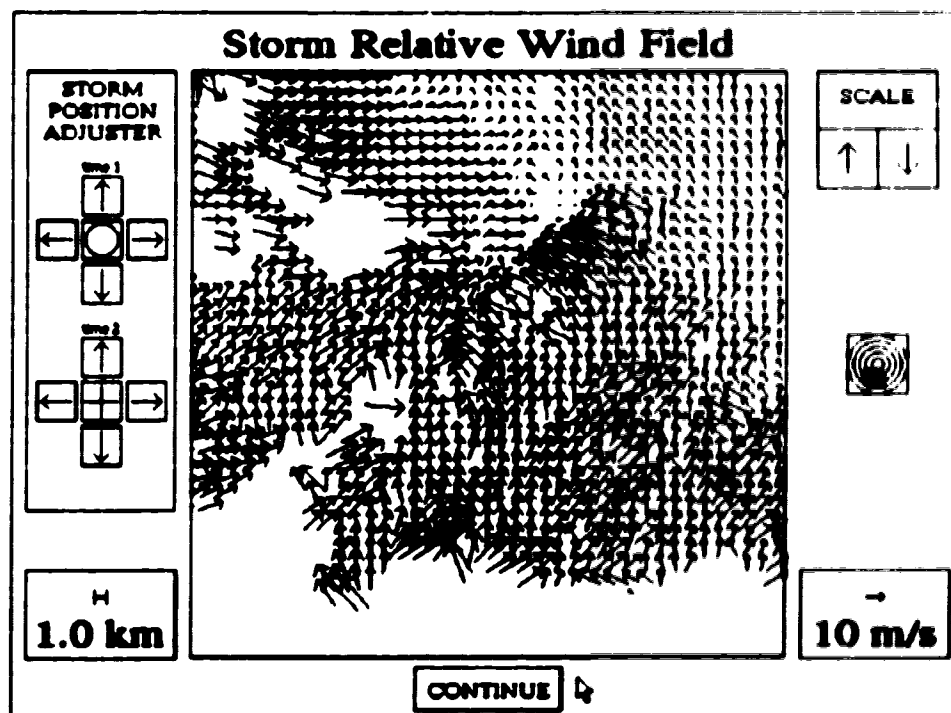
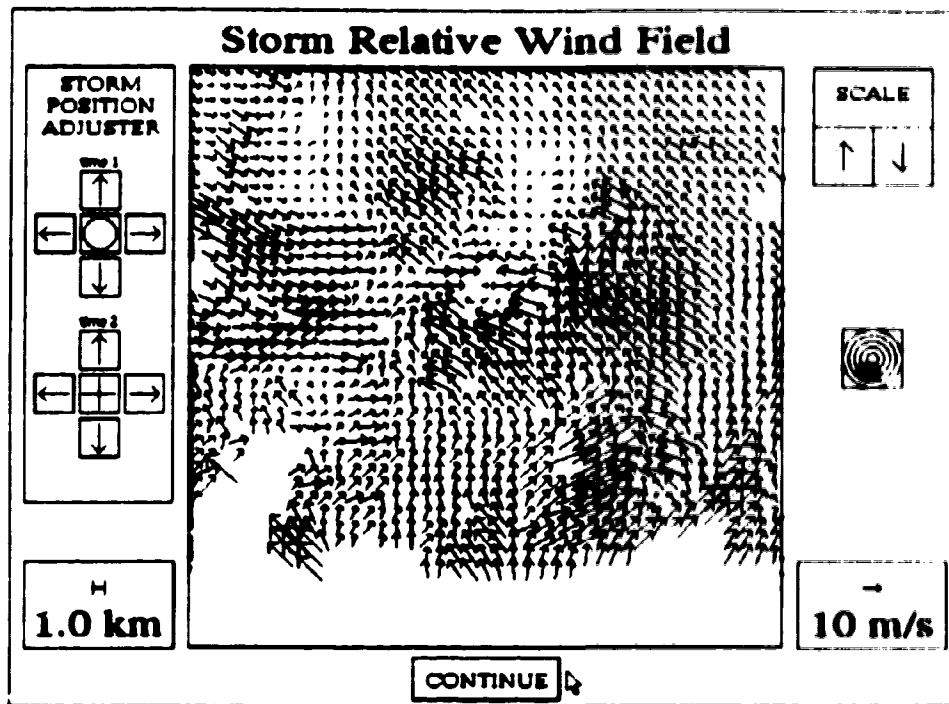


Figure 6.5B Storm relative wind fields for the 1.5° and 3.5° analysis of the Mississauga storm (2200Z-2220Z). Top panel shows 1.5° analysis, bottom panel shows the 3.5° analysis.

7. Conclusion and suggestions for future work

The SDD technique is a method whereby the horizontal wind field of a moving precipitation complex or storm is synthesized from two sequential Doppler radar observations. The technique is very similar to doing an actual dual-Doppler analysis except that, instead of two radars viewing a storm, a storm is viewed twice by the same radar, from different angles. A basic assumption of the technique is that the internal wind structure of the precipitating complex remains quasi-steady between the two radar measurements. The accuracy of the wind retrieval improves as the difference in the radar viewing angles of the storm increases (up to 90°).

This study was related to using the SDD technique with *operational* Doppler radars, such as the AES's King City and Carvel radars. These radars perform a Doppler velocity scan at only a few low elevation angles. In such cases, the radar data available for an SDD analysis often consist of a single conical surface, resulting from one low angle radar scan. Therefore, the radar measurement height (above ground) varies with the distance to the radar. In contrast, most research based Doppler radars provide a "full" volume scan (i.e. many elevation angles). The limited scan of operational Doppler radars restricts use of the SDD technique to analyzing weather features which maintain a fairly constant range from the radar. Otherwise, Doppler velocity measurements from different levels in the storm are used in the SDD wind synthesis. The resulting wind reconstruction is inaccurate if there is significant vertical wind shear in the feature being analyzed. The operational radar's limited scan also determines the height at which an SDD analysis may be made, and this height varies with the distance to the radar.

The objectives of this research were to (A) - *develop an SDD analysis package for an operational Doppler weather radar*, which could be used to (B) - *investigate the effect of various error sources on SDD derived wind fields* and to (C) - *determine whether or not the SDD technique is feasible and/or useful when based on limited Doppler scans, either for case studies or for real-time operational use by forecasters.*

7.1. Summary of the main results

A (Chapter 3)

The first part of the SDD analysis package is a program which can be used to simulate SDD analyses. This "SDD simulator" generates radial velocity components for a specified horizontal wind field and then uses these "Doppler measurements" in an SDD analysis. The generated radial wind fields can be modified before performing the wind synthesis. This provides a means of simulating realistic processes which cause errors and distortions in the reconstructed wind field (i.e. objective B).

The second main program in the analysis package is an SDD analyzer. This program was designed to read velocity data from the AES Doppler radars. It performs the SDD analysis and graphically display the synthesized wind field, as well as its vorticity and convergence. By doing various SDD analyses on actual cases, it was possible to determine the usefulness of the technique (i.e. objective C).

Since the SDD technique requires the matching of two radial wind field observations, the locations of the precipitating system must be accurately determined for both observations. When using real weather cases, these locations are not always well defined. For this reason, the programs are designed such that the storm positions can be *interactively* adjusted, with immediate feedback on the resulting analysis. Both programs run on an *inexpensive* computing platform (IBM), are *user-friendly* and can do complete SDD analyses in only a few minutes (i.e. *fast* enough for operational use).

B (Chapter 4)

The SDD simulator program was used to investigate the effects of the three major sources of error in an SDD analysis: spectrum broadening of the radial velocities, storm positioning errors and the effect of an evolving wind field.

Doppler measurements for a given radar echo vary significantly due to wind shear and turbulence. Radar units measure the radial velocity many times in order to obtain a "spectral width" and mean velocity value for a given point in the storm. The uncertainty in the mean radial velocity is related to the spectral width. As expected, simulations show that large uncertainties in radial velocity lead to a deterioration of the reconstructed wind field. Specifically, it was shown that *the RMS error in a reconstructed wind field is linearly proportional to the uncertainty in the radial components due to spectrum broadening.*

The effect of storm positioning was analyzed by doing simulations on various wind fields. It was shown that position inaccuracies can give significant errors in the resulting wind field. These errors tend to be asymmetric. Therefore, *even without knowing the precise storm positions in an SDD case (i.e. real cases), subjective storm position adjustment can be used to minimize errors caused by incorrect position matching* (by trying to remove the asymmetry). It was shown that horizontal position inaccuracies of x km will obliterate features in the wind field which have characteristic dimensions of less than x km (see also Klimowksi 1992). Since real cases for SDD often involve features of only a few km's, accuracy in horizontal positioning is crucial. As such, *operational SDD analysis packages can benefit significantly by incorporating run-time interactive storm position adjustment*. Errors in vertical position matching are also a problem with SDD on operational radars. Since a complete volume scan is not available, no adjustment is possible and use of the technique is restricted to cases where the motion of the storm or feature is mostly azimuthal.

The evolution of a wind field was modeled on the simulator to see its effects on the SDD wind synthesis. *For typical mesoscale dynamics, such as an intensifying mesocyclone, it was found that changes in the wind field over a 10 or 20 minute period can lead to large errors in a SDD synthesis*. It is therefore important to keep the time between the radar measurements as short as possible.

The angular separation between the radar measurements used in an SDD analysis must be as large as possible in order to obtain a useful wind reconstruction. This requirement is unfortunately limited by the desire to keep the time between radar observations as short as possible. Simulations and a statistical treatment show that *the RMS error in a reconstructed wind field is inversely proportional to sine of the difference in storm viewing angles*. In particular, cases with a viewing angle difference less than 20° cannot usually be accurately analyzed using the SDD technique.

The accuracy of wind synthesis using dual-Doppler techniques or the SDD method is dependent on the true wind orientation. The best wind magnitude estimates are obtained when the true wind is aligned along the bisector of the angle between the radars while the best wind directions are obtained when the true wind is aligned perpendicular to this bisector (Doviak 1976). Our simulations confirmed this result, but also suggest that, *for SDD analyses, the difference wind field due to spectral noise is mostly perpendicular to the average viewing angle from the radar*. This is however only true when the difference in storm viewing angles is relatively small (e.g. $< 40^\circ$).

Simulations indicated that reconstructed wind fields tended to have average wind magnitudes which were significantly larger than initial wind fields. This was investigated

further using simulations and a statistical treatment. The speed bias was found to be proportional to the relative uncertainty in the radial components and inversely proportional to the sine of the difference in viewing angles. In actual dual-Doppler analyses, where the uncertainty in radial components can be quite small and the difference in viewing angles is usually large, the speed bias is often negligible. This is not the case with SDD analyses: we find that *wind speeds in SDD analyses can often be overestimated by 10 to 80%*. The speed bias was formulated and a method to reduce wind magnitudes based on the relative uncertainty in radial velocity and the difference in storm viewing angles was proposed, tested and shown to be of merit.

C (Chapters 5 and 6)

Several actual cases were analyzed using the SDD technique to determine whether it is useful when based on limited Doppler scans.

A gust front (August 06 1993) near Edmonton was analyzed and results were found to be qualitatively reasonable when compared to other gust fronts. Using the convergence field of the derived wind field in conjunction with the storm relative winds at two levels, it was inferred that *a roll circulation was embedded in the August 06 1993 gust front*. Its characteristics were similar to detailed lidar observations of a roll embedded in a gust front (Christian 1993).

An SDD analysis was performed on a severe storm that occurred in central Alberta on July 29 1993. Results suggest that warm moist air was fed into the storm from the northeast. This *moist inflow was detected between 1000-2500 m (all levels analyzed), and appeared to be strongest at about 1000 m*.

The storm of July 30 1993 which spawned an F2-F3 tornado near Holden, Alberta was analyzed using the SDD technique. The reconstructed wind fields show a similar inflow to that observed on the July 29 storm, but also indicate a mesocyclone structure on the southeast edge of the storm which was moving northeast at 50 km/hr. Ground observations for this tornado were compared with the SDD analysis. In this case, the added information provided by *the SDD analysis would have given a tornado forecast lead time of about 90 minutes* (usually, 30 minutes is considered excellent for a tornado forecast lead time).

The SDD technique was also tested with the "Mississauga storm" from southern Ontario. The analysis indicated a large vortex (radius 8 km) and a smaller mesocyclone (radius 2 km). The retrieved wind fields were quite noisy, probably because of an evolving wind field. The results also indicated that radial velocity measurements used in the SDD

analysis must not come from different stages in the storm's lifetime. Since the transition from one stage to another can be very brief, this suggests that *even small times between the Doppler measurements may be inappropriate if this time interval happens to cross a transition state.*

Results of these cases of SDD analyses show the potential for the technique on a limited scan radar. The Holden tornado case suggests that *it may be useful to implement an SDD analyzer for real-time operational use, but it is likely that the technique will find more frequent application as a tool for doing case studies.*

7.2. Suggestions for future work

Based on my thesis research, I recommend the following extensions and future work on the SDD technique. Some are general, some deal in particular with limited scan radars.

1. *Interpolation schemes: for reducing variance and smoothing*

The method used to interpolate data from polar coordinates (radar) to Cartesian coordinates is discussed in Chapter 3 and Appendix B. A more sophisticated interpolation scheme might result in smoothing of the radial wind fields. A commonly used technique is that of Cressman (1959), where a radius of interpolation is specified. Features smaller than that radius will generally be lost in the smoothing. Various interpolation schemes exist (Doviak 1976) and can sometimes lead to a significant reduction in the standard deviation (or variance) of the mean radial velocity.

Implementing such interpolation schemes could give flexibility in deciding what should be smoothed out, depending on the case. In addition the variance reduction gives a lower uncertainty in the radial component wind fields (due to spectrum broadening), which could lead to a more accurate wind synthesis.

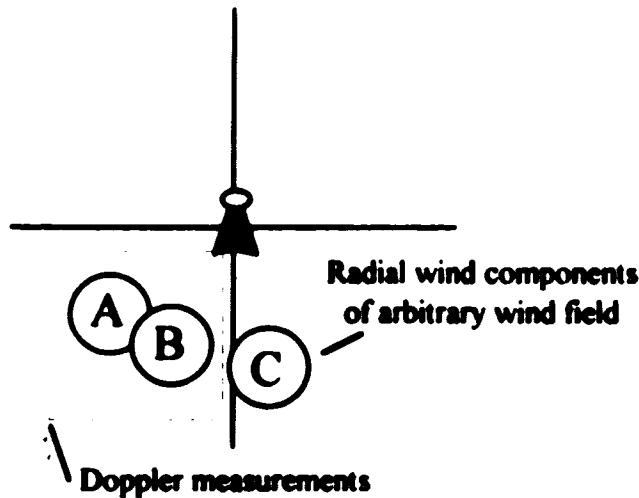
2. *Peace's original method of horizontal wind synthesis (see Chapter 1)*

The Doppler radar literature suggests that only Peace (1968) used a Taylor series approach to synthesizing a horizontal wind field from two radial component wind fields. This approach offers two possible advantages. First, the polynomial fitting of the radial wind fields provides "built in" interpolation and smoothing of data. Second, using the Doppler data as an ensemble may add to the accuracy of the wind retrieval. This approach

does however limit itself to the retrieval of linear wind fields, making it inappropriate for the study of complicated wind patterns.

3. *Determining the steadiness requirement using only 2 observations.*

In section 6.2 (the "Mississauga storm"), it was shown that use of the 2240Z radial wind field in the SDD analysis significantly perturbed the resulting wind field from what was obtained using the 2200Z-2220Z or 2210Z-2230Z radial wind fields. These results suggest that matching a radial wind field observation with an inappropriate radial wind field (i.e. not consistent with the first two observations) for a SDD analysis has a strong perturbing effect on the resulting wind field synthesis. I suggest that if the perturbing effect is the same for two different radial wind field sets, then these are probably quasi-similar (i.e. they are two views of a quasi-steady storm). This concept can best be discussed in terms of the diagram below:



If an SDD analysis using Doppler fields A and C gives a similar reconstructed wind field to the wind field based on B and C, then it is likely that the storm was quasi-steady between A and B, so that the SDD analysis using A and B is appropriate. I also suggest that this only works when the viewing angles to A and B do not differ very much (as in most SDD cases). The wind field C is in some ways arbitrary but should probably not differ too much from that in A and B (both unknown!). This is not an exact method but I suspect it may have some merit in that it could qualify the quasi-steadiness using only two Doppler observations. In real SDD cases, there are sometimes only two available

4. Wind field analysis using only one single Doppler measurement

It is possible to use two radial component measurements from different angles to reconstruct a complete horizontal wind vector under conditions where the wind field is uniform in x and y (Pilié 1963). This is similar to the VAD technique but uses only two data points instead of data from all azimuths. The geometry of the method happens to be identical to that of the SDD technique, but it requires the radial velocity from one time only. The uniformity requirement can be reduced to 1 dimension if band symmetry is assumed. The method might then be useful in analyzing banded precipitation structures.

A trial run of this approach was performed using the SDD analyzer with slight modifications. The analysis of a gust front over Edmonton on July 30 1993 gave plausible results.

5. NEXRAD and McGill: opportunities with full volume scans

The ongoing installation of NEXRAD radar units in the United States will give ample opportunity to test and use single-Doppler analysis techniques such as VAD (Easterbrook, 1975), VVP (Waldteufel, 1979) and SDD. These "state-of-the-art" operational radars will provide full ¹ volume scans of Doppler and conventional data at 5 minute intervals. Using such a volume scan eliminates most of the SDD errors associated with the comparison of radial components from different levels as encountered with limited scan radars. In addition, the volume scans permit SDD analyses of horizontal winds to levels of 12.0 km or more for observations beyond 35 km from the radar. The McGill radar observatory ², near Montréal, will also provide enhanced opportunities for the SDD technique. The volume scan measurements consists of 24 elevation angles and are repeated every 5 minutes (Singh et al 1993).

¹Plans are to have the radar scan from 0.5° to 19.5° in 14 increments (Klazura and Imy 1993).

²Recently renamed the J. Stewart Marshall Radar Observatory.

Bibliography

- Atlas D. and C.W. Ulbrich, 1990: *Early foundations of the measurement of rainfall by radar*, Radar in Meteorology, edited by D. Atlas, American Meteorological Society, Boston, 86-95.
- Barrat, P. and I.C. Browne, 1953: *A new method of measuring vertical air currents*, Quarterly Journal of the Royal Meteorological Society, Vol. 79, 550.
- Brantley, J.Q., Jr. and D.A. Barczys, 1957: *Some weather observations with a continuous wave Doppler radar*, Preprints, 6th Radar Meteorology Conference, American Meteorological Society, 297-306.
- Bonesteel, R.G. and Y.J. Lin, 1977: *A study of updraft-downdraft interaction based on perturbation pressure and single-Doppler data*, Monthly Weather Review, Vol. 106, 62-68.
- Bluestein, H.B. and D.S. Hazen, 1989: *Doppler-radar analysis of a tropical cyclone over land: hurricane Alicia (1983) in Oklahoma*, Monthly Weather Review, Vol. 117, 2594-2611.
- Bluestein, H.B., S.D. Hrebenach and E.A. Brandes, 1991: *A test of the synthetic dual-Doppler analysis technique: two case studies*, Preprints, 25th International Conference on Radar Meteorology, American Meteorological Society, 634-637.
- Browning K.A. and R. Wexler, 1968: *The determination of kinematic properties of a wind field using Doppler radar*, Journal of Applied Meteorology, Vol. 7, 105-113.
- Burgess, D.W., 1976: *Single Doppler radar vortex recognition: part I - mesocyclone signatures*, 17th Conference on Radar Meteorology, American Meteorological Society, 97-103.
- Caton, P.G.F., 1963: *Wind measurement by Doppler radar*, Meteorology Magazine, Vol. 92, 213-222.
- Christian, T.C., 1993: *A Doppler lidar and radar study of a Colorado squall line*, Preprints, 26th International Conference on Radar Meteorology, American Meteorological Society, 218-220.
- Cressman, G.P., 1959: *An operational objective analysis system*, Monthly Weather Review, Vol. 87, No. 10, 367-374.
- Crozier C.L., 1986: *King weather radar operations manual and users guide*, Internal publication, Atmospheric Environment Service, Environment Canada.

- Davies-Jones, R. P., 1979: *Dual-Doppler radar coverage area as a function of measurement accuracy and spatial resolution*, Journal of Applied Meteorology, Vol. 18, 1229-1233.
- Donaldson, N. R., 1992: *Outline of a pseudo-multi-Doppler routine developed at King Radar*, Internal report, King Weather Radar Station, Atmospheric Environment Service, King City, Ontario, Canada.
- Doviak, R. J. and P. S. Ray, 1976: *Error estimation in wind fields derived from dual-Doppler radar measurement*, Journal of Applied Meteorology, Vol. 15, 868-878.
- Doviak, R. J., D. Sirmans, D. S. Zrnic and G. B. Walker, 1978: *Considerations for pulse-Doppler radar observations of severe thunderstorms*, Journal of Applied Meteorology, Vol. 17, 189-205.
- Doviak, R. J. and D. S. Zrnic, 1984: *Doppler Radar and Weather Observations*, Academic Press.
- Dowell, D. C., H. B. Bluestein, D. O. Blanchard and D. P. Jorgensen, 1993: *Airborne Doppler radar analysis of an Oklahoma supercell*, Preprints, 26th International Conference on Radar Meteorology, American Meteorological Society, 212-214.
- Easterbrook, C. C., 1975: *Estimating horizontal wind fields by two-dimensional curve fitting of single Doppler radar measurements*, Preprints, 16th Radar Meteorology Conference, American Meteorological Society, 214-219.
- Fletcher, J. O., 1990: *Early developments of Weather Radar during World War II*, Radar in Meteorology, edited by D. Atlas, American Meteorological Society, Boston, 3-6.
- Fujita, T. T., 1973: *Tornadoes around the world*, Weatherwise, Vol. 26, 56-83.
- Gal-Chen, T., 1982: *Errors in fixed and moving frame of references: applications for conventional and Doppler radar analysis*, Journal of the Atmospheric Sciences, Vol. 39, 2279-2300.
- Joe, P. I., 1988: *The King City mesocyclone detection algorithm*, Internal publication, Atmospheric Environment Service, Environment Canada.
- Jorgensen, D. P., 1986: *Mesoscale and convective scale characteristics of mature hurricanes, Part I: General observations by research aircraft*, Journal of the Atmospheric Sciences, Vol. 41, 1268-1285.
- Klazura, G. E. and D. A. Imy, 1993: *A description of the initial set of analysis products available from the NEXRAD WSR-88D system*, Bulletin of the American Meteorological Society, Vol. 74, No. 7, 1293-1311.

- Klimowski, B. A. and J. D. Marwitz, 1990: *Single Doppler analyses of a severe squall line*, Preprints, 13th Conference on Severe Local Storms, American Meteorological Society, 252-255.
- Klimowski, B. A. and J. D. Marwitz, 1992: *The synthetic dual-Doppler analysis technique*, Journal of Atmospheric and Oceanic Technology, Vol. 9, 728-745.
- Krauss, M. J., 1974: *Doppler radar investigations of flow patterns within thunderstorms*, AFCRL Environmental Research Paper, No. 481, 86 p. [Available from Hanscom AFM, MA, (AFCRL-TR-74-0290).]
- Lemon, L. R. and C. A. Doswell III, 1979: *Severe thunderstorm evolution and mesocyclone structure as related to tornadogenesis*, Monthly Weather Review, Vol. 107, 1184-1197.
- Lemon, L. R., 1980: *Severe thunderstorm radar identification techniques and warning criteria*, NOAA Tech. Memo, NWS NSSFC-3, Kansas City, Mo (NTIS #PB81-234809), 67pp.
- Lhermitte, R. M., 1968: *New developments in Doppler radar methods*, Proceedings, 13th Radar Meteorology Conference, American Meteorological Society, 14-17.
- Lhermitte, R. M. and D. Atlas, 1961: *Precipitation motion by pulse Doppler*, Preprints, 9th Weather Radar Conference, American Meteorological Society, 218-223.
- Lhermitte, R. M. and L. J. Miller, 1970: *Doppler radar methodology for the observation of convective storms*, Proceedings, 14th Radar Meteorology Conference, American Meteorological Society, 133-138.
- Mohr, C. G., L. J. Miller, R. L. Vaughan and H. W. Frank, 1986: *The merger of mesoscale datasets into a common Cartesian format for efficient and systematic analysis*, Journal of Atmospheric and Oceanic Technology, Vol. 3, 143-161.
- Nelson, S. P. and N. C. Knight, 1987: *The hybrid multicellular-supercellular storm-an efficient hail producer. Part I: an archetypal example*, Journal of the Atmospheric Sciences, Vol. 44, No. 15, 2042-2059.
- Nichols, T. R., 1990: *A mesoscale convective system case study*, MSc thesis, York University, Toronto, Ontario.
- Peace, R. L. and R. A. Brown, 1968: *Comparison of single and double Doppler radar velocity measurements in convective storms*, Proceedings, 13th Radar Meteorology Conference, American Meteorological Society, 464-473.
- Peace, R. L., R. A. Brown and H. G. Cannitz, 1969: *Horizontal motion field observations with a single pulse Doppler radar*, Journal of the Atmospheric Sciences, Vol. 26, 1096-1103.

- Pilié, R. J., J. E. Justo and R. R. Rogers, 1963: *Wind velocity measurement with Doppler radar*, Proceedings, 10th Weather Radar Conference, American Meteorological Society, 329a-3291.
- Probert-Jones, J. R., 1960: *Meteorological use of pulsed Doppler radar*, Nature, Vol. 186, 271-273.
- Rankine, W. J. M., 1901: *A Manual of Applied Mechanics*, 16th ed., Charles Griffin and Company, 574-578.
- Rogers, R. R., 1990: *The early years of Doppler radar in Meteorology*, Radar in Meteorology, edited by D. Atlas, American Meteorological Society, Boston, 122-129.
- Singh, A., A. Kilambi, E. Ballantyne, A. Bellon, B. Katz and I. Zawadzki, 1993: *The McGill Doppler radar facility*, Preprints, 26th International Conference on Radar Meteorology, American Meteorological Society, 357-359.
- Smythe, G. R. and D. S. Zmic, 1983: *Correlation analysis of Doppler radar data and retrieval of the horizontal wind*, Journal of Climate and Applied Meteorology, Vol. 22, 297-311.
- Takahashi, N., H. Uyeda and K. Kikuchi, 1991: *A method to describe the fluctuation and discontinuity of horizontal wind fields by a single Doppler radar*, Preprints, 25th International Conference on Radar Meteorology, American Meteorological Society, 642-645.
- Wakimoto, R. M. and N. T. Atkins, 1993: *Airborne Doppler analyses of an intense extratropical cyclone during ERICA*, Preprints, 26th International Conference on Radar Meteorology, American Meteorological Society, 282-284.
- Waldteufel, P. and H. Corbin, 1979: *On the analysis of single-Doppler radar data*, Journal of Applied Meteorology, Vol. 18, 532-542.
- Watson, A. I., D. O. Blanchard, D. P. Jorgensen and D. W. Burgess, 1993: *The kinematic structure of a supercell thunderstorm seen by airborne Doppler radar*, Preprints, 26th International Conference on Radar Meteorology, American Meteorological Society, 209-211.
- Weisman, M. L. and J. B. Klemp, 1984: *The structure and classification of numerically simulated convective storms in directionally varying wind shears*, Monthly Weather Review, Vol. 112, 2479-2498.
- Weisman, M. L. and J. B. Klemp, 1986: *Characteristics of Isolated Convective Storms*, Mesoscale Meteorology and Forecasting, edited by P. S. Ray, American Meteorological Society, Boston, 331-358.

Appendix A Radar characteristics (WKR and WHK)

PARAMETER	CONVENTIONAL MODE	DOPPLER MODE
Disk diameter (feet)	20 (WKR) 12 (WHK)	
Peak power (kW)	260	
Microwave wavelength (cm)	5.34	
Microwave frequency (MHz)	5625	
Scanning rate (rpm)	6.0	0.75
Elevation angles (degrees) ¹	0.3 to 24.6 in 25 increments	0.5, 1.5 and 3.5 and 0.4 (folded)
Pulse duration (μs)	2.0	0.5
Pulse length (m)	600	150
Pulse repetition frequency (Hz)	250	1190 and 892
Range resolution (m)	300	75
Beamwidth (degrees)	0.65 (WKR) 1.1 (WHK)	
Effective azimuthal beamwidth (degrees) ²	1.8 (WKR) 2.2 (WHK)	0.85 (WKR) 1.4 (WHK)
Display resolution (km)	2	0.5
Max observed range (km)	256	113
Max displayed range (km)	220	110

WKR is the King City radar near Toronto. WHK is the Carvel radar near Edmonton. Most of the information in the table was obtained or inferred from Crozier (1986).

¹These values may vary slightly.

²This is the effective beamwidth when the motion of the antenna is taken into account.

Appendix B Data preprocessing

B1. Archive and decode of radar data (WHK and WKR)

The Doppler radar data are archived on optical disk and kept at the radar sites. Unfolding of the data is done prior to writing the archive. A program to read and decode the data files was written by Mr. Tom Nichols of AES. It provides an ASCII format output which can then be read by other programs.

Older data files, such as the ones for the July 24 1987 tornado case, had a different archive medium (tapes) and format. Unfolding of the data is not done prior to archiving and the data must then be unfolded before being used. A program was written to read, decode and unfold the data files.

Neither of these programs are included on the accompanying disk.

B2. Polar to Cartesian conversion of radar data

After being decoded, the Doppler velocities must be converted from polar coordinates (inherent to radar) to Cartesian coordinates.

First, a Cartesian grid (depending on a specified size and grid spacing) is established. The Doppler velocity data (polar coordinates) are matched to their nearest corresponding Cartesian location in the gridwork. If the nearest location is more than 3 grid spacings away, the grid cell is left empty. When a Doppler velocity is matched to a grid location which already contains a value, the one with the closest match is retained (i.e. the one with the polar coordinate location closest to the center of the Cartesian cell).

B3. Correction of folding errors and rejection of data

As described in Chapter 3, an attempt is made to correct unfolding errors in the Doppler velocities by adding (or subtracting) multiples of 2×12 or 2×16 m/s to a data point until the difference between it and its neighbors is minimized. If 3 or more (of a possible 8) neighbors to the data point still have Doppler velocities differing by 8 m/s or more, then the data point is cleared and left empty.

Once a wind synthesis is complete (by the SDD technique), data in which either the x or y component of the ground relative wind is greater than 35 m/s are removed. This

value was found useful in removing erroneous wind vectors caused by incorrectly dealiased data.

B4. Smoothing of the synthesized wind field

Before being displayed, the computed ground relative wind field is smoothed. This is done on wind vectors who have at least 4 immediate neighbors in the Cartesian grid. The following scheme was devised and used:

$$\bar{u}_{storm} = (0.7)u_{storm} + (0.3) \frac{\sum \text{neighboring } u's}{\# \text{ neighbors}}$$

This is a "light" smoothing since only 30% of the weight goes to the immediate neighbors. The smoothing is done independently on both the u and v wind components. The storm relative wind is obtained from the ground relative wind and therefore also contains this smoothing.

Appendix C Notes on the programs

The ASCII source code for the SDD simulator and the SDD analyzer are contained on the magnetic disk in the cover of this thesis. The disk is in Microsoft's DOS format. Various other programs associated with the SDD analyzer are not contained on the disk. These programs and the SDD analyzer were unified by a program (also not listed) which called each one as needed. This made for a semi-automatic analysis package where the only specified inputs were the filenames of the Doppler data, the grid spacing and resolution desired, the time between the Doppler observations and their locations.

A program was also developed to compare wind fields as output from the analyzer or simulator and calculate the average wind field speeds and the RMS difference between two wind fields. It is also included on the disk.

All programs were written in Microsoft's Quick C version 2.5, which runs on an IBM DOS platform. The data files used by the programs are described below.

C1. File formats

The radial component wind fields (Doppler velocities) are contained in files with the following format (example):

5	(dimension of matrix: e.g. NxN where N is 5)
3.0 2.0 1.0 0.0 -1.0	(spatial representation of radial velocities)
2.0 1.0 0.0 -1.0 -2.0	(in m/s, positive-away, negative-towards)
1.0 0.0 -1.0 -2.0 -3.0	
0.0 -1.0 -2.0 -3.0 -4.0	
-1.0 -2.0 -3.0 -4.0 -5.0	

These are called "*.add" files.

The files used to represent a wind field (either a given initial field, or a reconstructed field) are called "*.xyf" or "*.xys" files. The *.xyf files are the full representation of the wind field. The *.xys files are a spatial subset of the corresponding *.xyf file, the subset being determined by the offsets specified by "sliding windows" (Chapter 3). The format for these files (*.xyf and *.xys) is similar to the *.sdd files

5 (dimension of matrix e.g. NxN where N is 5)

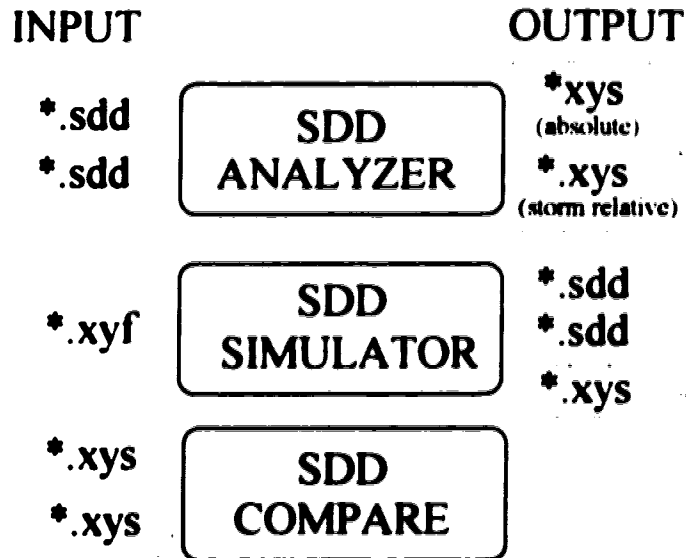
3.0	2.0	1.0	0.0	-1.0	(spatial representation of u component of wind, in m/s)
2.0	1.0	0.0	-1.0	-2.0	(+ve for eastward and -ve for westward)
1.0	0.0	-1.0	-2.0	-3.0	
0.0	-1.0	-2.0	-3.0	-4.0	
-1.0	-2.0	-3.0	-4.0	-5.0	

3.0	2.0	1.0	0.0	-1.0	(spatial representation of v component of wind, in m/s)
2.0	1.0	0.0	-1.0	-2.0	(+ve for northward and -ve for southward)
1.0	0.0	-1.0	-2.0	-3.0	
0.0	-1.0	-2.0	-3.0	-4.0	
-1.0	-2.0	-3.0	-4.0	-5.0	

All files (*.sdd, *.xyf, *.xys) are written in ASCII format. The *.sdd files are full representations of the radial wind field (i.e. not a subset from "sliding windows"). Several samples of the files are included on the disk.

C2. Input, output and interaction between the simulator and analyzer

The following diagram shows where the *.sdd, *.xyf and *.xys files are used in the SDD programs:



Two *.sdd files are used in the SDD analyzer, to produce *.xys files of the absolute and storm relative wind fields. A *.xyf file is specified for the SDD simulator, which generates the *.sdd files (with noise) and the computes the synthesized *.xys wind field. Note that the *.sdd files generated by the simulator can be used as an input to the analyzer (dotted lines). This is how the evolution of a mesocyclone (Chapter 4) was simulated. The SDD compare program is used to compare output (*.xys) files from either the analyzer, the simulator, or both (dashed lines).

Appendix D Derivations of (4.2),(4.5),(4.6).

The derivations contained in this appendix are based on the horizontal wind field synthesis equations (1.1):

$$u = \frac{r_1(\cos\beta_2) - r_2(\cos\beta_1)}{\sin(\beta_1 - \beta_2)}$$
$$v = \frac{r_2(\sin\beta_1) - r_1(\sin\beta_2)}{\sin(\beta_1 - \beta_2)}$$

and the associated error equations (2.2):

$$du = \frac{dr\sqrt{\cos^2\beta_2 + \cos^2\beta_1}}{\sin(\beta_1 - \beta_2)}$$
$$dv = \frac{dr\sqrt{\sin^2\beta_1 + \sin^2\beta_2}}{\sin(\beta_1 - \beta_2)}$$

D1. A general result

It is useful to derive an expression for the mean square deviations of the horizontal wind field:

$$\langle du^2 \rangle + \langle dv^2 \rangle$$

To do this, we first take the square of (2.2):

$$du^2 = \frac{(\cos^2\beta_2 + \cos^2\beta_1)dr^2}{\sin^2(\beta_1 - \beta_2)}$$
$$dv^2 = \frac{(\sin^2\beta_1 + \sin^2\beta_2)dr^2}{\sin^2(\beta_1 - \beta_2)}$$

Taking an average over a Gaussian distribution of noise in du and dv :

$$\begin{aligned} \langle du^2 + dv^2 \rangle &= \frac{\langle 2 dr^2 \rangle}{\sin^2(\beta_1 - \beta_2)} \quad \text{or} \\ \langle du^2 \rangle + \langle dv^2 \rangle &= \frac{2 \langle dr^2 \rangle}{\sin^2(\beta_1 - \beta_2)} \end{aligned}$$

By assuming that the error in the radial components is unbiased (i.e. $\langle dr \rangle = 0$), then:

$$\begin{aligned} \langle dr^2 \rangle &= \langle dr \rangle^2 + \sigma_r^2 \quad \text{becomes} \\ \langle dr^2 \rangle &= \sigma_r^2 \end{aligned}$$

so that:

$$\langle du^2 \rangle + \langle dv^2 \rangle = \frac{2\sigma_r^2}{\sin^2(\beta_1 - \beta_2)} \quad (\text{D.1})$$

D2. The root mean square error (4.2)

The definition of the RMS difference between a wind field and its reconstruction is defined as:

$$RMS_{error} \equiv \sqrt{\langle (u_0 - u)^2 \rangle + \langle (v_0 - v)^2 \rangle} = \sqrt{\langle du^2 \rangle + \langle dv^2 \rangle}$$

This definition, with result (D.1), simply gives:

$$RMS_{error} = \frac{\sigma_r \sqrt{2}}{\sin(\beta_1 - \beta_2)}$$

It is noted however, that when this relation is used on a wind field, the Gaussian distribution of noise is obtained from a spatial distribution. Therefore $\beta_1 - \beta_2$ and the standard deviation of the mean radial velocity may vary slightly. We can approximate the above expression as:

$$RMS_{error} \approx \frac{\overline{\sigma_r} \sqrt{2}}{\sin(\beta_1 - \beta_2)} \quad (4.2)$$

where the overbar represents a spatial mean on the wind field.

D3. The mean speed bias ratio (4.5 and 4.6)

We define the speed bias ratio as the ratio between the reconstructed and initial value of a given wind vector.

$$SBR^2 = \frac{[u^2 + v^2]}{[u_0^2 + v_0^2]} \quad (4.4)$$

Now we substitute:

$$u = u_0 + du$$

$$v = v_0 + dv$$

into (4.4), to get:

$$SBR^2 = \frac{[u_0^2 + 2u_0 du + du^2 + v_0^2 + 2v_0 dv + dv^2]}{[u_0^2 + v_0^2]}$$

If we then take an average over a Gaussian distribution of noise on du and dv

$$\langle SBR^2 \rangle = \frac{[u_0^2 + 2u_0 \langle du \rangle + \langle du^2 \rangle + v_0^2 + 2v_0 \langle dv \rangle + \langle dv^2 \rangle]}{[u_0^2 + v_0^2]}$$

If we assume that the errors in radial components are unbiased, then du and dv are also unbiased (see (2.2)), so $\langle du \rangle = \langle dv \rangle = 0$, giving:

$$\langle SBR^2 \rangle = \frac{[u_0^2 + \langle du^2 \rangle + v_0^2 + \langle dv^2 \rangle]}{[u_0^2 + v_0^2]}$$

Now, using (D.1), we can write:

$$\langle SBR^2 \rangle = 1 + 2 \left(\frac{\sigma_r}{\sqrt{u_0^2 + v_0^2}} \right)^2 \frac{1}{\sin^2(\beta_1 - \beta_2)} \quad (D.2)$$

Now:

$$\langle SBR^2 \rangle = \langle SBR \rangle^2 + \sigma_{SBR}^2$$

so that

$$<SBR> = \sqrt{1 + 2 \left(\frac{\sigma_r}{\sqrt{u_0^2 + v_0^2}} \right)^2 \frac{1}{\sin^2(\beta_1 - \beta_2)} - \sigma_{SBR}^2}$$

Numerical experiments reported in Chapter 4 indicate that $\sigma_{SBR}^2 \ll 1$, resulting in:

$$<SBR> \cong \sqrt{1 + 2 \left(\frac{\sigma_r}{\sqrt{u_0^2 + v_0^2}} \right)^2 \frac{1}{\sin^2(\beta_1 - \beta_2)}} \quad (D.3)$$

Now, since the Gaussian distribution of noise is obtained from a spatial distribution (wind field), then $\beta_1 - \beta_2$ and the standard deviation of the mean radial velocity may vary slightly. We can approximate the above expression as:

$$\overline{SBR} \cong \sqrt{1 + 2 \left(\frac{\overline{\sigma_r}}{\sqrt{u_0^2 + v_0^2}} \right)^2 \frac{1}{\sin^2(\beta_1 - \beta_2)}} \quad (4.5)$$

where the overbars represent the spatial average over the wind field.

If (4.5) is to be used to reduce reconstructed wind speeds in a real case, then it must be rewritten so as to remove the right hand dependence on the initial wind speeds. To do this, we first recall the definition of SBR to write:

$$<SBR^2> = \frac{<u^2 + v^2>}{u_0^2 + v_0^2}$$

Combining this with (D.2):

$$\frac{<u^2 + v^2>}{u_0^2 + v_0^2} = 1 + 2 \left(\frac{\sigma_r}{\sqrt{u_0^2 + v_0^2}} \right)^2 \frac{1}{\sin^2(\beta_1 - \beta_2)}$$

so that:

$$u_0^2 + v_0^2 = <u^2 + v^2> - \frac{2\sigma_r^2}{\sin^2(\beta_1 - \beta_2)}$$

Substituting this into (D.3) gives:

$$\langle SBR \rangle \cong \sqrt{1 + \frac{2\sigma_r^2}{\langle u^2 + v^2 \rangle \sin^2(\beta_1 - \beta_2) - 2\sigma_r^2}}$$

Since the average over a Gaussian distribution is obtained from the spatial distribution of the wind field, we approximate the above expression as

$$\overline{SBR} \cong \sqrt{1 + \frac{2\overline{\sigma_r^2}}{\left(\overline{\sqrt{u^2 + v^2}}\right)^2 \sin^2(\overline{\beta_1 - \beta_2}) - 2\overline{\sigma_r^2}}} \quad (46)$$

where the overbars signify that the averaging is performed over the wind field

Appendix E Calculations for an evolving mesocyclone

If we model a mesocyclone as a circular 2-D solid object of radius r with an outer rim velocity of v , then the divergence of that object can be defined as.

$$D = \frac{\Delta \text{area} / \Delta \text{time}}{\text{area}} = \frac{2 \, dr}{r \, dt} = \frac{2 \, d \ln r}{dt}$$

If the divergence, D , is constant with time, then the integration of the above equation gives.

$$r = r_0 e^{Dt/2}$$

where r_0 is the radius at an initial time and t is the time elapsed since that time. The radius halving time is therefore given by:

$$t = \frac{2 \ln 2}{D}$$

By using conservation of angular momentum and the definition of vorticity for solid body rotation of a 2-D object:

$$\frac{d(vr)}{dt} = 0 \quad \text{(conservation of momentum)}$$

$$\zeta = \frac{2v}{r} \quad \text{(vorticity for solid body rotation of circular object)}$$

$$\frac{d(r^2 \zeta)}{dt} = 0$$

$$\frac{d\zeta}{dt} = \frac{-2\zeta \, dr}{r \, dt} = -\zeta \left(2 \frac{d \ln r}{dt} \right) = -\zeta D$$

Integrating gives:

$$\zeta = \zeta_0 e^{-Dt}$$

and a vorticity doubling time given by:

$$t = \frac{\ln 2}{D}$$